BIOSENSING PERFORMANCE OF SURFACE PLASMON POLARITON BRAGG GRATINGS

by

Kholoud Khalid Gazzaz

A thesis submitted to the
Faculty of Graduate and Postdoctoral Studies in partial fulfillment of the requirements for the degree of Master in Physics

Ottawa-Carleton Institute of Physics
Faculty of Science
University of Ottawa

Abstract

Surface plasmon biosensors have raised much interest over the past few decades for their potential in biosensing applications. This thesis investigates the plasmon-polariton Bragg grating, which is a novel structure that supports surface plasmon modes. Plasmon-polariton Bragg gratings PPBGs consist of metal stripes embedded in Cytop. A number of designs were investigated to evaluate the biosensing capabilities of the device. The biosensing performance was studied for both bulk and surface sensitivities via wavelength interrogation. The biosensing study was conducted by observing changes in the effective refractive indices of the supported modes by changing the index of the sensing solution for bulk sensitivity, and by changing the thickness of the adlayer that represents the binding of the target analyte to the sensing surface for surface sensitivity. A theoretical assessment of the achievable sensitivity and detection limit for PPBGs is conducted via two approaches, wavelength and output power interrogation.

Acknowledgments

First and foremost, I thank Allah for helping me and giving me the strength, the health, and the patience to pursue my studies, which have been a dream for me for years.

It is also a pleasure to thank those who have made this thesis possible...

First, a special thanks to my beloved parents; my mother who always encourages me to pursue my studies and follow my dream, and who reminds me of this dream during the difficult moments, and my dear father who passed away at the beginning of my Masters journey, but whose support, encouragement, and endless kindness are always with me, and act as a candle that gives me hope and encourages me to persevere during hard times. I also thank my beloved husband, my little sweethearts (Ammar and Lamees), and my brothers and sisters whose patience, kindness, encouragement, and endless support allowed me to study. No words can express my gratitude to you for understanding, supporting, and believing in me.

I would like to convey my sincere and deepest gratitude to my supervisor, Prof. Pierre Berini, for his help, advice, patience, encouragement and guidance.

I would also like to deliver many thanks to my friends and colleagues for their assistance and for making my stay at the University of Ottawa a delightful experience.

Finally, I would like to thank Valerie Georganas for proof reading this thesis.

Acronyms

SPR	Surface Plasmon Resonance
SPPs	Surface Plasmon Polaritons
LRSPP	Long Range Surface Plasmon Polariton
ATR	Attenuated Total Reflection
FBG	Fiber Bragg Gratings
PPBGs	Plasmon Polariton Bragg Gratings
TE	Transverse Magnetic
TM	Transverse Electric
CMT	Coupled Mode Theory
TMM	Transfer Matrix Method
SAM	Self Assembled Monolayer
LOD	Limit of Detection
FoM	Figure of Merit
FWHM	Full Width Half Maximum

Table of Contents

List of Figures

List of Tables

Appendix

Chapter 1 Introduction and Literature Overview

1.1 Introduction

1.1.1 Thesis Motivation

Optical biosensors are devices used to detect and analyze biomolecular interactions. A significant number of biosensors, based on different methods, have previously been studied. Surface plasmon resonance (SPR) biosensors are very powerful tools for studying and characterizing biomolecular interactions. At this time, they are the most common optical biosensors on the market [1].

Since the first SPR sensor, SPR biosensors have produced great achievements in both instrumentation development and application. This technology dominates the field of biosensing and is an important tool used to characterize and quantify bimolecular interactions [2, 1, 3]. As of yet, there exists no comparable technology that can characterize molecular interactions in such a robust manner, in real time, and without labelling. SPR applications cover many fields, and their technology is well established in areas such as biomedical research, health care, drug discovery, the food industry, environmental monitoring, and homeland security. For example, SPR based biosensors are used commercially to quantify vitamins and to monitor drug remnants in food matrices, such as, confirming the presences of vitamin supplements in baby food or detecting harmful residues of hormones in meat. Whatever the aim is, the detection process needs to be fast and reliable.

SPR biosensors are also found to be immune to electromagnetic interference, allowing them to perform remote sensing and to provide a multiplexed detection within a single device [4].

The results of many sensing experiments conducted using long range surface plasmon polaritons have been reported, and these results were promising as they reveal the capability

of this mode in biosensing [5, 6, 7, 8]. These results encourage the use of different structures that support this mode in biosensing, in order to exploit the features of these structures, which might lead to an improved biosensing performance. Plasmon polaritons Bragg gratings (PPBGs) is a novel structure that revealed attractive characteristics, and by our knowledge has not yet been studied for biosensing applications.

In the field of biosensing there is always a need for a more accurate and reliable diagnostic platform. The history of success of surface plasmons in this field encourages further investigations in order to meet the demands of different areas.

1.1.2 Thesis Objectives

The objectives of this thesis are to model, design, and evaluate the performance of Bragg gratings based on long range surface plasmon polaritons for biosensing. This is considered to be a new technique in biosensing, which might have certain advantages over the available biosensors, as it is a phase sensor and the output signal shows a dip. The thesis includes designing plasmon polaritons Bragg gratings PPBGs for biosensing, optimizing the biosensing performance, and evaluating these designs. PPBGs have been studied by Jettè [9, 10], and the present thesis can be considered as an extension of that study. According to our knowledge, this structure has not yet been studied for biosensing. Several grating profiles have been reported by Jettè, and the step-in-width waveguides with a rectangular profile PPBGs has been selected for the biosensing study.

PPBGs were designed by properly selecting the dimensions of the waveguides that construct the gratings, then the gratings were designed to operate over three different wavelength ranges. The biosensing performance was evaluated by computing both surface and bulk sensitivities for PPBGs. The sensitivities were studied in two different ways, for the gratings and for the waveguides that construct the gratings. Figures of merit are used to compare the performance of different designs operating at different wavelengths.

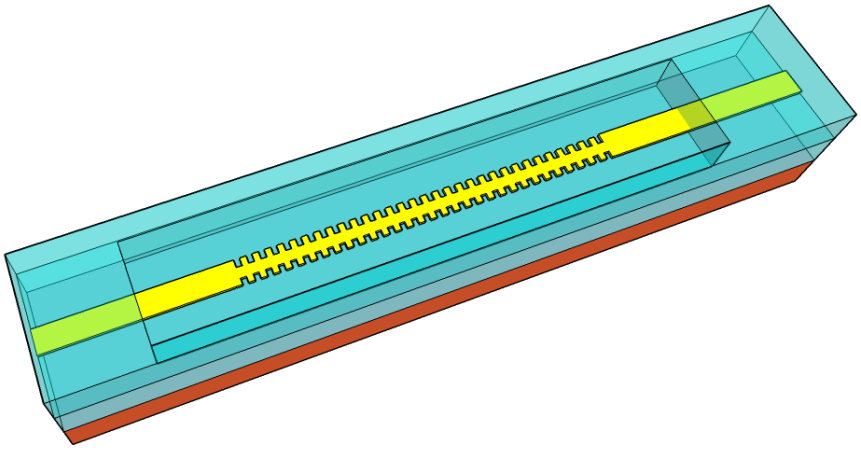

Figure 1: PPBGs used for biosensing.

1.1.3 Thesis Organization

This thesis is divided into five chapters. Chapter 1 is an introduction to SPR and long range surface plasmon biosensors, and a brief overview of the development of these biosensors. Chapter 2 is an overview of long range surface plasmon polaritons, which are the core of this study, and of the characteristics of the finite width waveguides that support this mode and are the foundational elements of PPBGs.

In chapter 3 PPBGs are presented, as well as the family of designs at three wavelengths, the modeling approach, the design rules and the theoretical performance.

Chapter 4 is a study of the biosensing performance of different grating designs including surface and bulk sensitivities. Surface sensitivity is studied in two ways; for grating designs and for the waveguides that comprise the gratings. The detection limits are also obtained for both sensitivities, with two different interrogations.

Chapter 5 contains a summary of this thesis and concluding remarks, as well as the future work.

1.1.4 Thesis Contributions

This thesis laid the foundation for the use of PPBGs in biosensing. Several designs were studied at three different wavelengths, and their optical performances were compared. The properties of PPBGs from wavelength response, bandwidth, and Bragg wavelength have

been characterized to enable the understanding of their biosensing performance. The biosensing performance was investigated theoretically for both surface and bulk sensitivities, which we believe to be for the first time. The surface sensitivity was investigated in two different ways, revealing a good agreement between both.

1.2 Literature Overview

1.2.1 Background

Surface plasmon resonance (SPR) biosensors are important tools used to characterize and quantify biomolecular interactions. In the last three decades, a vast number of research studies were conducted to develop and improve optical sensors able to detect and quantify biological and chemical molecules.

In 1982, the first sensing application of SPR was revealed. It was utilized for gas detection, measuring the concentration of CO_2 and O_2 by measuring the changes in the absorption spectrum [11]. Ever since, the use of SPR in biosensing is increasing rapidly and the field is attracting researchers who are interested in developing new sensing configurations and applications. A great diversity of optical methods have been used in biosensors and chemical sensors such as ellipsometry, spectroscopy (luminescence, phosphorescence, fluorescence, Raman), interferometry (white light interferometry, modal interferometry in optical waveguide structures), spectroscopy of guided modes in optical waveguide structures (grating coupler, resonant mirror), and SPR [12]. The SPR sensors are used to measure physical, chemical, and biological quantities. In SPR devices the analyte interaction can be determined by measuring certain parameters. Depending on the sensor, it could be the refractive index, the absorbance and fluorescence properties of analyte molecules, or a chemo-optical transducing medium [12].

The first observation of surface plasmons was conducted by Wood, who attributed the anomalous diffraction from metal gratings on the excitation of the surface waves. Wood pointed a polarized light at a mirror with diffraction gratings and observed a pattern of dark and light bands in the reflected light [13]. This phenomenon was not explained until the late

sixties, when the excitation of surface plasmons via the method of attenuated total reflection (ATR) was reported by Kretschmann and Otto [14]. Kretschmann used a prism with a layer of metal and observed the intensity of the reflected light by changing the angle of incidence. The excitation was seen as a strong decrease in the intensity of the reflected light. Since then, the surface plasmon has been the subject of a vast number of studies, and its properties have been studied intensively.

Surface plasmon resonance is the excitation of SPPs by light. Surface plasmon polaritons can be defined as a charge density oscillation that exists between two media with opposite signs of dielectric constants, such as metal and dielectric. The charge density is correlated with an electromagnetic field that peaks at the interface and decays exponentially as it extends into both media. The surface wave is TM polarized, which means that the magnetic vector is perpendicular to the direction of propagation and parallel to the interface. The propagation constant of the surface plasmon is given in chapter 2. Since metals are lossy materials, the surface plasmon polaritons SPPs suffer from high attenuation while propagating in the visible and near-infrared spectral regions. The majority of the electromagnetic field is distributed in the dielectric region and concentrated at the interface [15], as in Figure 2.

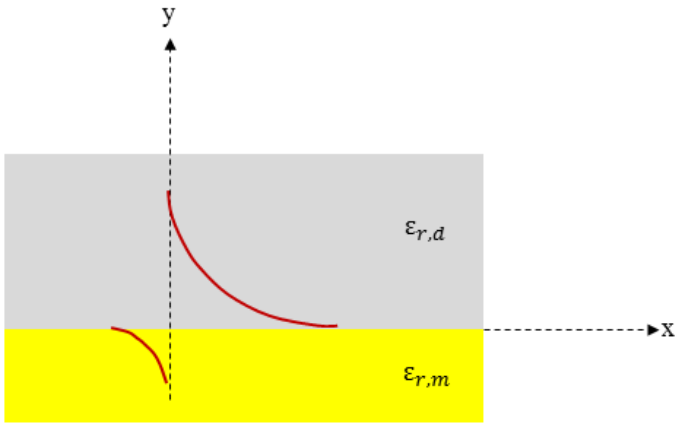

Figure 2: The field is concentrated at the interface while the majority of the field in the dielectric region.

1.2.2 The Potential of SPR in Biosensing

The potential of SPR in biosensing relies on the very high sensitivity of the SPPs at the interface to changes in the refractive index of the dielectric. Any change in the refractive index of the sensing medium results in a change in the propagation constant of the SPPs. Consequently, the resonance condition will also change [16].

As mentioned in the previous section, the field in SPPs reaches its maximum at the interface and decays exponentially as it extends into the bounding media; the potential of SPPs in biosensing relies on this fact. The field of the SPP is concentrated at the interface and the spectral position of a resonant structure is highly dependent on the dielectric properties near the resonance. Due to the high level of energy at the interface, even slight changes at the interface caused by a molecular monolayer can result in appreciable changes in the properties of the mode [12] (*e.g.* adsorption of the target analyte at the sensing surface results in changes of the supported mode), and this is the principle of SPR biosensing.

Furthermore, the mode characteristics and phase constant depend on the dielectric. Since the majority of the mode field is in the dielectric, any changes in the refractive index of the dielectric would affect the supported mode (*e.g.* presence of the target analyte) [2].

Surface plasmons showed a great potential in biosensing in several studies. Recent research has exposed interesting features of some structures that support SPPs; these structures can be used to develop biosensing.

1.2.3 SPR Biosensors

SPR based biosensors are considered very powerful tools for the study of biomolecular interactions. They are effective devices used to detect and analyze biological entities, and have important applications in biomedical research, health care, pharmaceuticals, environmental monitoring, and homeland security. SPR biosensors are also found to be immune to electromagnetic interference, where the presence of an electromagnetic field from another device does not affect their performance, revealing the capability of performing remote sensing, and allowing multiplexed detection within a single device.

SPR biosensors are sensing devices that consist of a biorecognition element attached to the sensing surface, able to recognize and bind with the target analyte that exists in the sensing solution. The binding results in a change of the refractive index at the sensing surface, which can be measured optically [3]. The binding with the analyte is thus translated into changes in the output signal.

In general, SPR sensors are composed of an optical system, a transducing medium that relates the optical and biochemical domains, and an electronic system that allows the data to be processed. The transducing medium translates the change resulted from the presence of the target analyte into a change in the refractive index. The optical system of the sensor consists of a source of optical radiation and an optical structure that supports SPPs [12]. The properties of the SPR subsystems play an important role in determining the property of the sensor. Both the transducing medium and the optical system determine the sensitivity, stability, and resolution of the sensor, while the selectivity and the response time are based on the transducing medium [12]. In other words, SPR sensors are devices made of thin metal film that support surface plasmon and can measure the changes in the refractive index occurring at the interface. SPPs are excited at the interface and their evanescent field extends at the media. Changes in the refractive index of the sensing media will lead to changes in the propagation constant of SP, which will modify the characteristics of the light wave coupled to the surface plasmon, such as coupling angle, intensity, coupling wavelength and phase. SPR sensors are categorized as angular, intensity, wavelength, and phase modulation based sensors depending on the characteristics that they measure [1].

The sensing surface of SPR sensors consists of a thin metal layer with a biorecognition element presented by functionalizing the metal surface, as in Figure 3. When the target analyte binds to the biorecognition element and the interaction takes place, the refractive index near the surface is changed; this change is detected by the SPR sensor and translated into useful information.

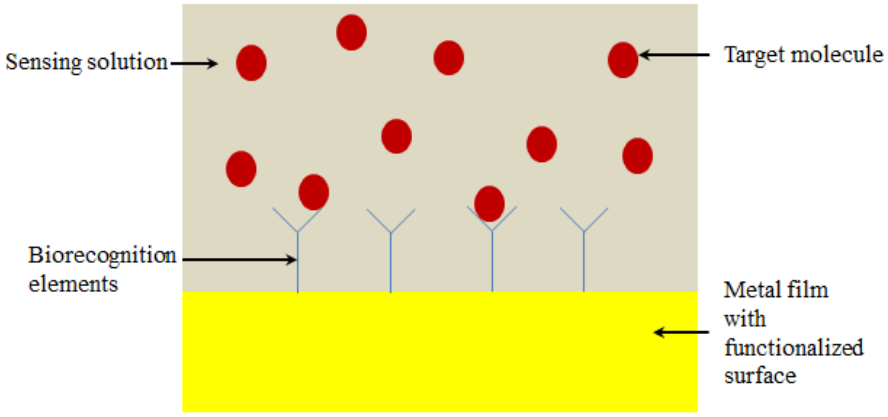

Figure 3: Illustration of basic optical biosensor.

The most common configuration of SPR biosensors is the Kretschmann geometry (Prism-based SPR) of ATR, since this configuration has proven practical and useful for sensing [16]. This configuration consists of a glass prism with a high index and a thin metal film of about 50 nm of gold, with a functionalized surface. In this configuration, a light wave is totally reflected at the interface between the prism coupler and the metal film, and excites the SPPs via evanescent tunneling through the metal layer with a TM polarized optical beam. The beam is launched beyond the critical angle, and the intensity or the phase of the reflected wave is monitored. The intensity of the reflected signal will reveal a minimum value when the incident beam couples efficiently with the surface wave at the interface. This SPR configuration has been studied intensively, covering all detection approaches: the measurement of the intensity of the reflected light wave, the measurement of the resonant angle of incidence of the light wave, or measurement of the resonant wavelength of the incident light wave. This configuration is adopted for the best commercialized SPR biosensor [16]. Even though this configuration is widely commercialized, it suffers from limitations. It is an approach that is bulky and difficult to miniaturise [17].

The development of SPR based on ATR was sought in order to obtain compact, mobile, and cost effective sensing devices neither of which has arguably been achieved. In order to improve the SPR sensing performance, many studies have been conducted to investigate different structures and sensing approaches. For example, SPR performance can be

enhanced by using Kretschmann geometry and replacing the gold film with an array of gold nanorods [18].

An effective SPR biosensor should be compact, with high resolution and sensitivity. The miniaturization of SPR sensors can be attained with fiber based approaches. Optical fiber based sensors are compact and appealing for in vivo applications; in this type of sensor, the cladding layer is removed and a thin gold film cover is used to allow the excitation of SPPs. Theoretical analysis of this structure revealed an improvement in the resolution when using Bragg gratings [19]. Another type of SPR sensor that offers an improvement in miniaturization is the waveguide-based sensor [16].

The sensitivity of SPR was the focus of many studies, and it was found that decreasing the operating wavelength enhances the sensitivity as the changes in the refractive index increase [5].

The detection methods of SPR are based on different approaches such as the measurement of the intensity of the optical wave near resonance, and the measurement of the resonant momentum of the optical wave (*e.g.* angular and wavelength interrogation of SPR) [3].

Due to the limited propagation length of SPP, the sensing is done directly at the area of excitation. Consequently, increasing the interaction length of SPP does not enhance the performance as is common in other types of sensors such as sensors based on dielectric waveguides [3].

One structure that revealed a promising performance in biosensing is a multilayer structure that supports Long ranges SPPs (LRSPPs). In this structure, a thin metal film is bounded by two dielectric media with the same dielectric constants. This mode can be excited using a Kretschmann-like geometry with alterations in order to form the symmetry required in the refractive indices. In this structure, a dielectric film with a similar refractive index to that of the sensing medium is placed between the metal film and the prism [16].

1.2.4 LRSPP Biosensors

Sensitivity enhancement is a goal in biosensing research. Most of SPPs sensors are based on the interrogation of the propagation of the mode of interest [12]. The mode characteristics

play an important role in the sensitivity. It is known that the sensitivity increases with field confinement and with a decrease in the attenuation. Using a multilayer structure supporting LRSPPs instead of a single interface enhances the sensitivity by lowering the attenuation [12]. It was found that three layer structures provide better surface sensing than single interface [5].

LRSPPs are surface waves that are able to propagate along metal slabs or stripes for considerable lengths, when the metal is bound by index matched dielectrics [20]. The propagation of this mode was investigated experimentally using different metals and different dielectrics for the claddings [21]. LRSPPs are less confined than SPPs, which makes it less sensitive, but its low attenuation allows it to propagate further, providing longer (interaction) sensing length [5, 6]. The propagation length for LRSPP is ~2000 μm *vs.* ~ 80 μm for the SPP supported by a two layer structure [22]. In addition, its penetration depth is higher (~1 μm *vs*. ~200 nm), which enables it to sense more analyte along this dimension [6]. Sensitivity enhancement in LRSPPs based biosensors enables the detection of small molecular interactions (few hundreds of Daltons) or of low molecular concentrations, which was not possible with conventional SPR biosensors [23]. In addition, LRSPPs can be supported by many integrated optical elements such as S-bends, Y-junctions, couplers and Mach–Zehnders [21] . These characteristics of the long range mode show great potential for biosensing applications.

In order to support the LRSPP mode, the refractive indices of the dielectrics around the metal stripe should be similar [20]. In biosensing applications, the symmetry of the structure can be obtained by supporting the metal stripe with a thin optically, not-too-invasive dielectric membrane, where the sensing fluid is surrounding the stripe [24], or by using a periodic dielectric stack supporting Bloch waves to support the metal stripe [25]. The most common way is by using dielectric material with an index close to that of the sensing solution; the dielectric is used as the lower cladding, while the metal is exposed to the sensing solution from the upper part to allow the bimolecular interaction to take place; this is the configuration adopted for this thesis.

A number of biosensing studies have been carried out using a LRSPP mode propagating along a thin Au stripe bounded by a symmetric dielectric environment. Biosensors using

LRSPP revealed higher sensing performance than conventional SPR biosensors. The sensor based on Kretschmann geometry was modified to support the long ranging mode [8]; this device features higher sensitivity to refractive index changes with deeper penetration depth. The LRSPP waveguides were used in different kinds of integrated components such as S-bends, Y-junctions, and couplers [6], as well as a metal slab in a prism-coupling geometry, and as metal stripes in an integrated Mach-Zehnder interferometer (MZI) on SiO_2 and covered with index matched oil [5]. They were used for detecting large biological objects (*e.g.* cells) in addition to small biochemical entities such as proteins [6]. Also, their ability to be used for biosensing was evaluated in [21], where the surface film was chemically functionalized to detect and identify cells based on cell identity markers [21]. The aforementioned study was performed by using Au waveguides surrounded by Cytop with microfluidic channels etched over the waveguides; the waveguides were integrated in Y-junction, S-bends, and couplers. The upper cladding was formed by a glycol/water solution with an index matching that of the lower cladding (Cytop) [26] in order to support the symmetric mode [21]. The experiment was carried out to study the response of the waveguides to the detected analyte by examining the binding of the cells to the surface of the waveguide [21].

The biosensing performance of 1D LRSPP waveguides was assessed theoretically in [5]. This study investigated the performance of different structures that support SPPs (*e.g.* single interface, metal/insulator/metal (MIM), and insulator/metal/insulator (IMI). The waveguides were integrated into a MZI with a single output, as in Figure 4. It was found that MIM and IMI show greater sensitivity than that offered by the single interface, even though they are on opposite sides of the confinement – attenuation trade off. The selected materials were Au for the metal, and H_2O as the background, since gold is a good plasmonic metal and H_2O is compatible with the sensing solutions, and an adlayer with an index representative of biological samples, in order to study the surface sensing. The study was conducted for a range of metal thicknesses ($5 \rightarrow 200$ nm), with a wavelength sweep from 600 to 1600 nm. It was found that the biosensing performance was enhanced when decreasing the wavelength and the best wavelength was 850 nm. The present thesis follows the same biosensing approach presented in this study.

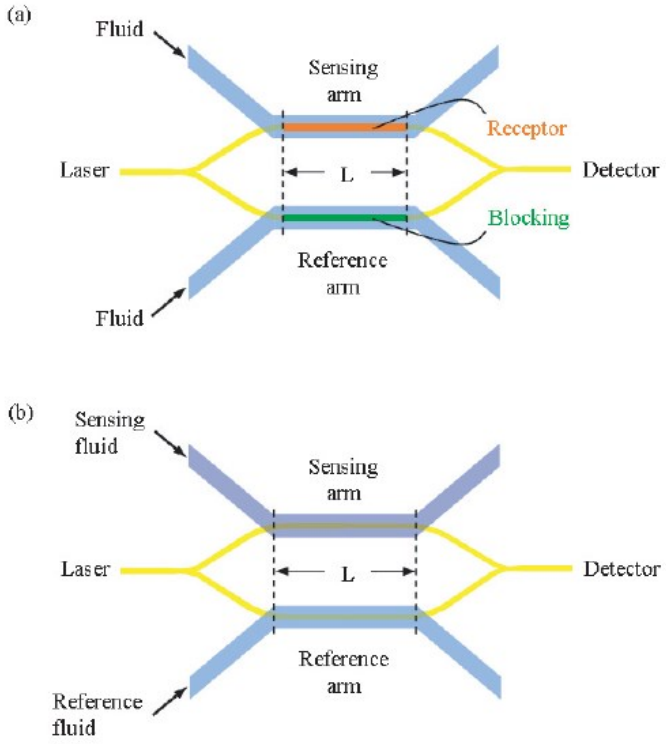

Figure 4: Sketches of MZIs used for surface and bulk sensing respectively. Adopted from [5].

Straight LRSPP waveguides have been used as biosensors to detect cells, proteins and changes in the bulk refractive index of solutions [6]. The waveguides used were comprised of Au metal film of 22 nm thickness and 5 µm width, embedded in Cytop. The stripes were exposed to the sensing solutions via microfluidic channels etched into the upper cladding [6], as in Figure 5. In this study, bulk sensing was investigated by injecting several solutions with different refractive indices to determine precisely the most suitable refractive index of the sensing solution. The Au waveguides were functionalized with antibodies to ensure the selectivity of cells. The study revealed the capability of LRSPP waveguides to detect bulk changes and the presence of different analyte with different sizes, ranging from large biological objects such as cells to small biological entities such as proteins. These biosensors are compact and inexpensive to fabricate.

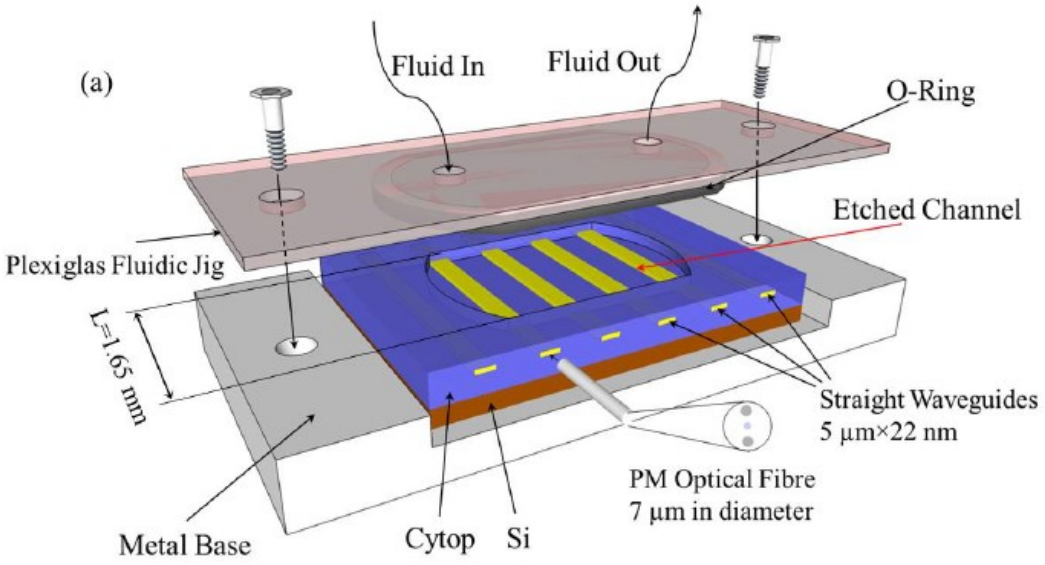

Figure 5: sensing device comprised of LRSPP waveguides exposed to the sensing fluid via microfluidic channels. Adopted from [6].

Another study was done by the same group, providing a deeper understanding of red blood cell detection using the same device but with different dimensions for the gold film [27]. The waveguides are comprised of Au films of 5 µm in width and 35 nm in thickness embedded in Cytop with an etched fluidic channel to allow the exposure of the sensing surface to the sensing solution. The device was fabricated by spinning Cytop on a Si wafer. The surface of the Au films was functionalized with antibodies against A antigen since A and AB red blood cells have the A antigen incorporated into the cell membrane, and the four blood groups were used as analyte and injected separately on the same functionalized waveguide. The selective capability was verified since only A and AB blood cells were detected, responding to the A antigen functionalized on the metal surface. Other types of red blood cells showed a negative response. In addition, a regeneration of the A antigen on the same sensing surface was applicable without changes in the binding response between the first and last binding. Regeneration is an important feature since it enables the reuse of the same device, reducing the cost of blood grouping. This biosensor also showed the ability to detect the cells even when very few cells were present.

The capability of biosensors based on LRSPP waveguides to detect small entities was investigated in [28] and the capability of biosensors operated with LRSPP waveguides of detecting cells was investigated in [29]. In the latter, the sensing surface was functionalized with antibodies against the bacteria being investigated, a wavelength sweep from 1265 nm to 1350 nm was performed, and the output power of the mode was observed. A comparison was done to assess the changes in the waveguides output as a result of binding bacteria to the sensing surface. The difference in the output power was high, and it was determined that good results are obtained around 1310 nm, as the mode exhibits little to no radiation while having a good sensitivity profile of the power variation.

LRSPP waveguides were integrated with Mach-Zehnder refractometric sensor [17] and the bulk sensing was investigated by injecting several sensing solutions with different refractive indices. The waveguides had a thickness of 34 nm and a width of 5 μm, the wavelength used was of 1310 nm. The study concluded that LRSPP waveguides with MZIs are promising for compact devices with a high performance. Surface sensing was also studied with the same structure, revealing results comparable to those of conventional SPR sensors [30].

The fundamental symmetric LRSPP mode (ss_b^0) revealed great potential for use in biosensing since it exhibits high surface sensitivity and low attenuation. The promising results for biosensing based on the long ranging mode encourages researchers to seek higher biosensing performance, thus exploiting the useful features and attributes offered by other metallic structures that support SPPs such as Bragg gratings. In addition, various studies suggest that a combination of different optical structures on the same sensing device would improve the performance and combine the advantages of each individual structure [4, 5].

The propagation of electromagnetic waves along line defects in periodic corrugated metal surface was studied by Bozhevolnyi [31]. The investigated structure consists of a thick film of evaporated gold on a glass substrate covered with periodic triangular lattices of gold scatterers. The line defects in this structure are of different widths and orientations, and perform as waveguides in a photonic band gap lattice supporting the electromagnetic waves. This study was followed by another study by Bozhevolnyi *et al*. [32] where the LRSPP were supported by a thin metal film with rectangular ridges placed periodically on the film in a

symmetric manner, as in Figure 6. These thickness variations form Bragg gratings. This structure transmits only one polarization.

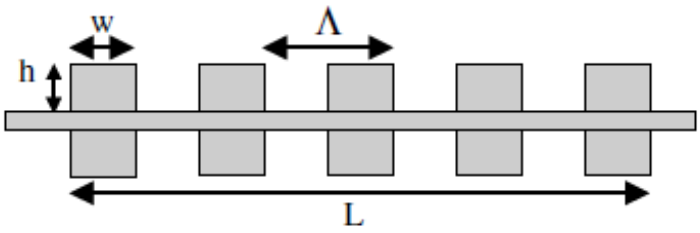

Figure 6: metal film with identical, periodic ridges placed above and under the film in a symmetric manner. "Reprinted from [32], copyright 2005, with permission from Elsevier."

The aforementioned structure was presented in a later study as a compact LRSPP Bragg grating [33]. The study was concerned with the propagation of the LRSPP along a structure comprised of patterning LRSPP waveguides with different thicknesses. The structure was embedded in homogenous dielectric at a wavelength near the telecom range. The behaviour for this grating is found to be similar to conventional reflecting Bragg gratings. The designs used in the study involved a range of thicknesses. Actually, the idea of LRSPP Bragg gratings was presented for the first time by Jettè [10, 34, 9, 35] . The grating structure here differs from designs performed by Bozhevolnyi as it is comprised of patterning waveguides with different widths and unchanging thicknesses over a length L. The variation of width is taken in the direction of propagation, as in Figure 7. Even though this grating is weaker than the former, it is easier to fabricate and to integrate. Jettè investigated several surface plasmon polariton Bragg grating PPBG structures such as non-periodic or chirped PPBGs. This thesis work can be considered as an extension of the Jettè thesis, since the periodic step in width design is adopted to conduct the study, following the same approach presented by Jettè.

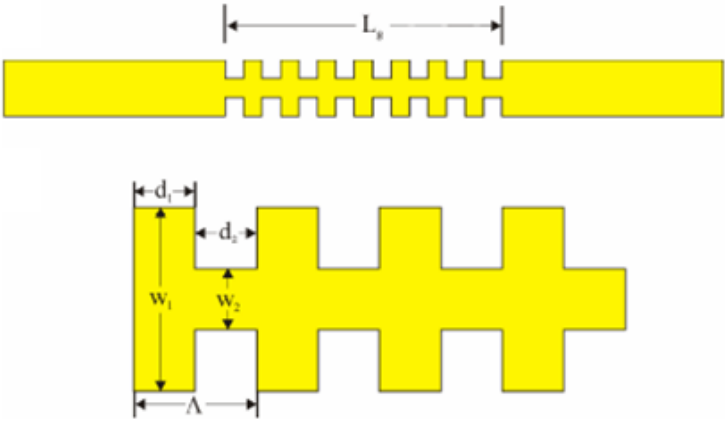

Figure 7: Top view of PPBGs with patterning the width.
Adopted from [35].

LRSPP based sensors with a Bragg gratings structure were proposed and investigated in [36, 37], but the structure was completely different than the structure adopted for this thesis. In reference [37], LRSPPs are supported by an asymmetric double electrode structure consisting of a metal slab with a Bragg grating layer topped with a finite width metal stripe, containing a microfluidic channel in between, and bounded by dielectric as claddings, as in Figure 8. The mode is confined by the metal stripe and slab.

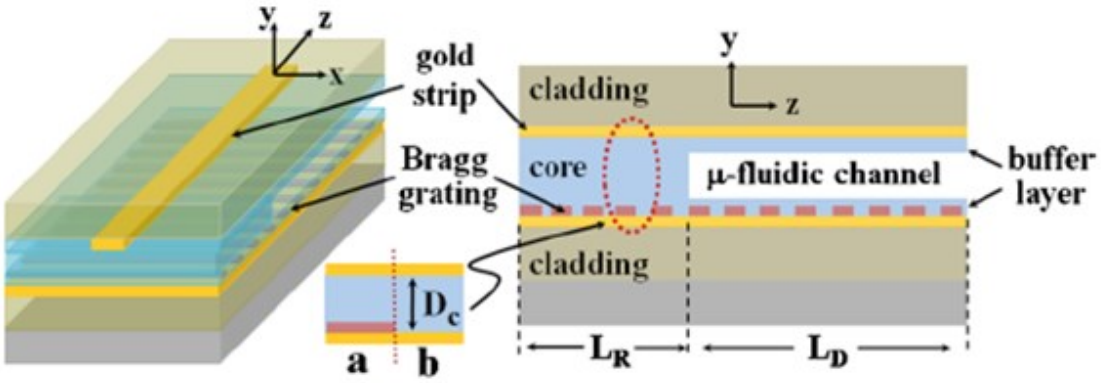

Figure 8: Schematic of asymmetric double electrode structure with Bragg gratings with cross sectional view. "Reprinted with permission from [37]. Copyright 2010, AIP Publishing LLC."

Chapter 2 LRSPPs Waveguides

This chapter contains an introduction to long range surface plasmon polaritons (LRSPPs), which are central to this study, and the structures that support this mode. The chapter will also describe the waveguides used in this study to produce LRSPPs.

At optical wavelengths, some metals are considered to be a free electron gas where conduction electrons are free to move in the metal. The electromagnetic properties of the electron gas can therefore be applied to metals [20].

The electron gas can enhance and retain a charge density oscillation called a plasma oscillation when one group of charges moves in relation to the other. Interaction between plasma oscillation and light in the visible and near infra-red regions leads to a surface plasmon, which can be defined as a transition of energy, carried by the photons of light, to a collective excitation of free electrons at the interface; this transfer happens under certain conditions and only at a specific resonance wavelength of light, when the momenta of the photon and the plasmon are matched [38]. The interface that supports this interaction is described in the following section.

2.1 Single Interface

Any interface between two semi-infinite materials with opposite signs of dielectric constants supports transverse magnetic TM (E_x= H_y=H_z=0) surface waves. If the two semi-infinite materials are a metal and a dielectric, the supported surface waves are called surface plasmon polaritons (SPPs); the interface that supports SPPs is called a single interface. The real part of the permittivity for the metal is negative and the real part of the permittivity for the dielectric is positive. At the interface between metal and dielectric, the free conduction electrons, which are abundant in the metal, will interact with the photons of light creating electromagnetic surface waves called surface plasmon polaritons (SPPs) [20]. These surface

waves propagate along the interface with a field that peaks at the interface and decays exponentially as it extends into each media away from the interface [12, 39, 40, 41].

To understand the properties of the SPPs, we should study the fields in the simplest structure that supports SPPs, which is the single interface. The field components for $\boldsymbol{E}$ and $\boldsymbol{H}$ of the propagating wave can be found using Maxwell's equations. Maxwell's equations provide a full understanding of the interaction between the electromagnetic fields and metals. In the rectangular coordinates, the equations that control the electromagnetic fields are written as follows

$$\nabla \times \boldsymbol{E} = -\frac{\partial \boldsymbol{B}}{\partial t} \tag{2.1}$$

$$\nabla \times \boldsymbol{H} = \boldsymbol{J} + \frac{\partial \boldsymbol{D}}{\partial t} \tag{2.2}$$

$$\nabla . \boldsymbol{D} = \rho \tag{2.3}$$

$$\nabla . \boldsymbol{B} = 0 \tag{2.4}$$

where $\boldsymbol{E}$ is the electric field, $\boldsymbol{H}$ is the magnetic field, $\boldsymbol{B}$ is the magnetic induction, $\boldsymbol{D}$ is dielectric displacement, and ρ and $\boldsymbol{J}$ are the charge and current density respectively, and are assumed to be zero, since there are no external sources. The constitutive relations are taken as follows

$$\boldsymbol{D} = \varepsilon \boldsymbol{E} \tag{2.5}$$

$$\boldsymbol{B} = \mu \boldsymbol{H} \tag{2.6}$$

From equations (2.1) and (2.2), a set of equations can be obtained, and for harmonic time dependence ($\frac{\partial}{\partial t} = i\omega$), the set of equations can be written as follows:

$$\frac{\partial}{\partial y} E_z - \frac{\partial}{\partial z} E_y = -i\omega\mu H_x \tag{2.7}$$

$$\frac{\partial}{\partial z} E_x - \frac{\partial}{\partial x} E_z = - i\omega\mu H_y \quad (2.8)$$

$$\frac{\partial}{\partial x} E_y - \frac{\partial}{\partial y} E_x = - i\omega\mu H_z \quad (2.9)$$

$$\frac{\partial}{\partial y} H_z - \frac{\partial}{\partial z} H_y = i\omega\varepsilon E_x \quad (2.10)$$

$$\frac{\partial}{\partial z} H_x - \frac{\partial}{\partial x} H_z = i\omega\varepsilon E_y \quad (2.11)$$

$$\frac{\partial}{\partial x} H_y - \frac{\partial}{\partial y} H_x = i\omega\varepsilon E_z \quad (2.12)$$

where μ is the permeability, and in homogenous media it is taken as $\mu = \mu_0$ (*e.g.* for air μ_r =1) , and μ_0 is the permeability of free space. ε is the permittivity $\varepsilon_i = \varepsilon_0 \varepsilon_{r,i}$, where ε_r is the complex relative permittivity, ε_0 is the permittivity at the free space, and *i* refers to the medium.

These equations support two solutions of propagating waves. These solutions represent the p-polarized (TM) and the s-polarized (TE) electromagnetic modes. The propagation is taken in the +z direction and evolves according to $e^{-\gamma z}$ with a harmonic time dependence $e^{+i\omega t}$, where γ is the propagation constant in (m^{-1}), and is defined as $\gamma = \alpha + i\beta$, and α and β are the attenuation and the phase constants respectively. The propagation constant can be written as

$$\gamma^2 = \gamma_x^2 + \gamma_y^2 + \gamma_z^2 \quad (2.13)$$

and defined by

$$\gamma = -\omega^2 \mu\, \varepsilon \quad (2.14)$$

Considering the propagation along the z axis, the field along the direction of the propagation can be written as follows by using the separation of variables

$$E_z = X(x)\, Y(y)\, Z(z) \quad (2.15)$$

where $X(x) = A_x\, e^{-\gamma_x x}$, $Y(y) = A_y\, e^{-\gamma_y y}$, and $Z(z) = A_z\, e^{-\gamma_z z}$

Considering no variation in x direction ($\frac{\partial}{\partial x} = \gamma_x = 0$), the field in the dielectric region along the direction of propagation can be written as follows

$$E_{z,d} = \mathrm{A} e^{-\gamma_{yd} y}\, e^{-\gamma_z z} \tag{2.16}$$

where $\gamma_d^2 = -\omega^2 \mu\, \varepsilon_d$ (2.17)

γ_{yd} is the propagation constant in y direction in the dielectric region. Using equation (2.13) yields the following equation

$$\gamma_{yd}^2 = -(\omega^2 \mu\, \varepsilon_d + \gamma_z^2) \tag{2.18}$$

Similarly, the field in the direction of the propagation in the metal region is written as follows

$$E_{zm} = \mathrm{A} e^{\gamma_{ym} y}\, e^{-\gamma_z z} \tag{2.19}$$

and

$$\gamma_{ym}^2 = -(\omega^2 \mu\, \varepsilon_m + \gamma_z^2) \tag{2.20}$$

In both regions, the surface waves propagate along the z direction with the same propagation constant γ_z, since the waves are confined at the interface. The field components can be found by using the previous equations as well as the equations derived from Maxwell's equations.

For TM modes, the six field components are

$$E_x = H_y = H_z = 0 \tag{2.21}$$

In the dielectric region, the rest of the components are

$$E_{z,d} = \mathrm{A}\, e^{-\gamma_{y,d} y}\, e^{-\gamma_z z} \tag{2.22}$$

$$E_{y,d} = -\mathrm{A}\, \frac{\gamma_z}{\gamma_{y,d}}\, e^{-\gamma_{y,d} y}\, e^{-\gamma_z z} \tag{2.23}$$

$$H_{x,d} = \mathrm{A}\,\frac{i\omega\varepsilon_d}{\gamma_{y,d}}\,e^{-\gamma_{y,d}y}\,e^{-\gamma_z z} \tag{2.24}$$

In the metal region, the rest of the field components are

$$E_{z,m} = \mathrm{B}\,e^{\gamma_{ym}y}\,e^{-\gamma_z z} \tag{2.25}$$

$$E_{y,m} = \mathrm{B}\,\frac{\gamma_z}{\gamma_{y,m}}\,e^{\gamma_{y,m}y}\,e^{-\gamma_z z} \tag{2.26}$$

$$H_{x,m} = -\mathrm{B}\,\frac{i\omega\varepsilon_m}{\beta_{y,m}}\,e^{\gamma_{y,m}y}\,e^{-\gamma_z z} \tag{2.27}$$

where A and B are constants. If the surface wave supported by the interface propagates along the interface, then a component of the electric field that is normal to the interface must exist. Hence, our interest is in p-polarized modes, where the magnetic field ***H*** is parallel to the interface. To satisfy the confinement at the interface, the boundary conditions should be enforced on all interfaces. The tangential fields should be continuous across the interface, at x = 0

$$\hat{y} \times [\boldsymbol{H}_d(0,z) - \boldsymbol{H}_m(0,z)] = 0 \tag{2.28}$$

$$\hat{y} \times [\boldsymbol{E}_d(0,z) - \boldsymbol{E}_m(0,z)] = 0 \tag{2.29}$$

Since ($E_x = H_y = H_z = 0$), then the boundary condition equations can be written as

$$E_{zd}(0,z) = E_{zm}(0,z) \tag{2.30}$$

$$H_{xd}(0,z) = H_{xm}(0,z) \tag{2.31}$$

Substituting equations (2.22) and (2.25) in (2.30), and equations (2.24) and (2.27) in (2.31), the following equation is obtained

$$\gamma_z = i\beta_0 \sqrt{\frac{\varepsilon_{r,d}\varepsilon_{r,m}}{\varepsilon_{r,d}+\varepsilon_{r,m}}} \tag{2.32}$$

where $\beta_0 = 2\pi/\lambda_0 = \omega/c_0$ and c_0 is the velocity of light in free space. For the lossless case, the previous equation can be written as follow

$$\beta = \beta_0 \sqrt{\frac{\varepsilon_{r,d}\varepsilon_{r,m}}{\varepsilon_{r,d}+\varepsilon_{r,m}}}$$

$$= \beta_0 \sqrt{\frac{\omega^2-\omega_p^2}{2\omega^2-\omega_p^2}} \qquad (2.33)$$

where $\varepsilon_{r,2} = 1 - \frac{\omega_p^2}{\omega^2}$, ω is the excitation frequency, and ω_p is the electron plasma frequency. The previous equation is the dispersion relation for SPPs; it expands into real and imaginary parts. The dispersion relation relates the components of the wave vector of the propagating electromagnetic wave to the frequency and the medium properties [42] , as in Figure 9.

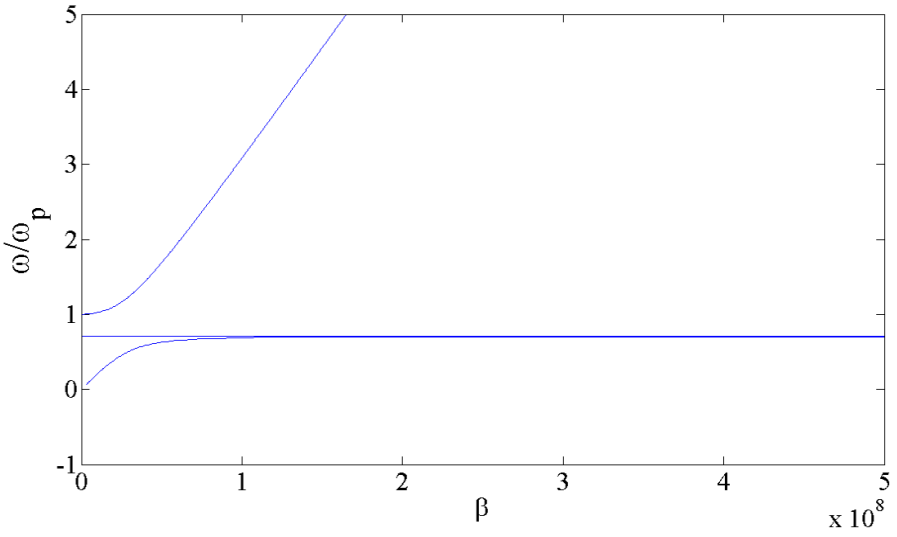

Figure 9: Dispersion relation of surface plasmon at the interface between metal and dielectric.

From the previous Figure, it is noted that at low values of β, SPP acts as a photon, but with an increasing β, the dispersion relation reaches the plasma frequency. Because of the bounding nature of SPP, special techniques are needed to allow the excitation of SPP.

In the case of TE modes, the ***E*** field is parallel to the interface, and this leads to a set of equations similar to equations (2.21) to (2.27), and when applying the boundary conditions (continuity of H_z and E_x the interface), we find that this mode is not supported by a single interface structure.

The main transverse electric field component is E_y, and since $\varepsilon_{r,m} >> \varepsilon_{r,d}$. The field decays faster in the metal than in the dielectric, as in Figure 10.

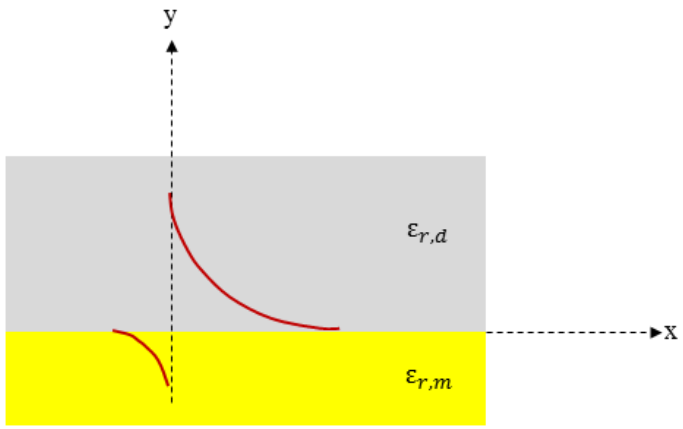

Figure 10 : An interface between two semi-infinite media that have real dielectric constants with opposite signs can support a purely bounded TM mode (E_x= H_y=H_z=0). The main transverse electric field distribution for the mode is sketched in red.

The SPPs at the single interface exhibit interesting properties and characteristics such as sub-wavelength confinement, high surface and bulk sensitivities, and high attenuation. The fact that this mode is bounded to the interface makes it very sensitive to surface irregularities.

2.1.1 Metal Permittivity

In general, metals can be characterized by a dielectric constant that includes a large and negative real part, and a small imaginary part. The imaginary part is the result of electronic damping and it determines the loss in the metal [43]. Any material that has a negative permittivity (ε) or permeability (μ) is considered to be opaque to electromagnetic radiation,

and light cannot penetrate metals very far, or at all, and is instead trapped at the surface as SPPs [44]. The imaginary component causes the SPP modes to have limited propagation length, thus metals with a small imaginary part offer longer propagation length values. There are only four metals that possess small imaginary dielectric constants, they are: Gold, Silver, Copper, and Aluminum [43].

At optical wavelengths, the metal film can be treated as a free electron gas. According to Drude's electron theory, the complex relative permittivity of the metal region can be given by the plasma frequency dispersion relation:

$$\varepsilon_{r,2} = \left[1 - \frac{\omega_p^2}{\omega^2+\nu^2}\right] - i\left[\frac{\omega_p^2\,\nu}{\omega(\omega^2+\nu^2)}\right] \tag{2.34}$$

Where ω is the excitation frequency, ω_p is the electron plasma frequency, and ν is the effective electron collision frequency and can be written as $\nu=1/\tau$, and where τ is the relaxation time of electrons in the metal. If the denominator is greater than the numerator in the first term of the equation then the condition to support the propagation of a surface wave will be satisfied, and this is the case at optical wavelengths [45].

2.2 Three Layer Structure

2.2.1 Metal film with infinite width

The previous concept of a single interface can be used in the optical slab waveguide by placing a metal film of a certain thickness t between two semi-infinite dielectrics. A metal film with thickness t and permittivity ε_3 bounded by dielectrics from above and below (ε_1 and ε_2), is considered as a wave-guiding structure (optical slab). If the metal film is thick enough (optically infinite), double interfaces will exist at both metal sides. When the thickness of the metal film decreases, the modes along both interfaces will start to couple due to tunnelling through the metal film. The modes supported by both interfaces will couple creating supermodes that exhibit dispersion with metal thickness [20, 46, 47]. This structure (the optical slab) supports only two purely bound TM ($E_x = H_y = H_z = 0$) modes

guided by the infinitely wide metal film, because only the TM state satisfies the boundary condition. These modes are defined by their field distribution.

The optical slab is considered symmetric when the claddings have matching or slightly different dielectric constants ($\varepsilon_1 = \varepsilon_2$), and is considered to be asymmetric when ($\varepsilon_1 \neq \varepsilon_2$). The two modes that are supported by the metal slab have transverse field components E_y, and H_x that exhibit symmetry or asymmetry along the *x* axis. E_y is the field component that dominates in this structure. In a plane perpendicular to the direction of propagation, the electric field of the mode consists of a single component E_y, normal to the interfaces and having either a symmetric or asymmetric spatial distribution across the optical slab. When the spatial distribution is symmetric, the mode that is supported by the structure is denoted as s_b mode; the mode is denoted as a_b mode when the field distribution is asymmetric. The confinement and attenuation of the s_b mode decrease with a decreasing thickness *t*, whereas the opposite is applied for a_b mode with a decreasing *t*. The s_b mode is often termed as a long range surface plasmon polariton (LRSPP) because it can propagate for a longer distance than a_b due to its low attenuation, and s_b exhibits less confinement than a_b mode as a result of the low attenuation. The a_b mode's field penetrates further into the metal film, which makes it more lossy (higher attenuation) by comparison with s_b mode [20, 47]. In general, there is a trade-off between confinement and attenuation, and they are always associated to each other.

Increasing the metal film thickness *t* leads the a_b and s_b modes to become degenerate; by further increasing the thickness they begin to split into a pair of uncoupled plasmon polariton modes on both top and bottom metal-dielectric interfaces. Thus, the propagation constants of the a_b and s_b modes are similar to the propagation constants of the modes supported by a single interface, and can be expressed by the following equations:

$$\beta/\beta_0 = \mathrm{Re}\left\{\sqrt{\frac{\varepsilon_{r,1}\varepsilon_{r,2}}{\varepsilon_{r,1}+\varepsilon_{r,2}}}\right\} \tag{2.35}$$

$$\alpha/\beta_0 = -\mathrm{Im}\left\{\sqrt{\frac{\varepsilon_{r,1}\varepsilon_{r,2}}{\varepsilon_{r,1}+\varepsilon_{r,2}}}\right\} \quad (2.36)$$

where $\varepsilon_{r,1}$ and $\varepsilon_{r,2}$ are the complex relative permittivities of metal and dielectric used [20, 47].

As mentioned previously, SPPs have interesting characteristics but high attenuation and confinement in one dimension only; this limits the applications for these modes. In order to exploit the interesting properties of the modes, the attenuation should be decreased; a practical way to do this is by using a metal film with a finite width embedded by dielectric [22].

2.2.2 Thin Metal Film with Finite Width

A thin metal film of finite width *w* and of thickness *t,* embedded by semi-infinite homogenous dielectrics from all sides, behaves as a waveguide where the metal film is the wave guide core. It is similar to the optical slab except that the width of the metal film is limited, as in Figure 11.

The thin metal film of finite width and its associated modes was studied theoretically by Berini [20, 41] and was experimentally tested by Charbonneau [46]. This waveguide does not support purely TM modes, because all six field components are present for all modes but they are TM-like in nature. By limiting the width, lateral confinement occurs, which enhances the mode spectrum, decreases the attenuation compared to the modes at the metal slab, and causes the waveguide to offer two dimensional confinement. The dominant field component is determined by the geometry of the wave guide. If the width of the metal film is greater than thickness $w>t$ then E_y dominates while E_x dominates when the thickness is larger than the width $t > w$. In this study E_y dominates since $w>> t$.

This structure supports four fundamental modes and a number of higher order modes. These modes can be divided into four groups depending on their field distribution [20]. All modes supported by this structure are supermodes created from the coupling of edge and corner surface waves, and their evolution with decreasing metal thickness is similar to the evolution

of the s_b and a_b modes in the metal slab [48]. To identify the modes, a pair of letters (*s*) and (*a*) are used to show the symmetry or asymmetry of the main transverse field along the y and *x* axes respectively. Then, a super script is used to identify the number of extrema observed in the spatial distribution along the longest dimension, and subscripts (*b*) or (*l*) are used to identify whether the mode is bound or leaky. According to this, the fundamental modes supported by this structure are: ss_b^0, aa_b^0, sa_b^0 and as_b^0. The mode of interest in this study is the fundamental mode that exhibits symmetry in both vertical and horizontal axes and is denoted as ss_b^0; this mode is called a long range surface plasmon polaritons or LRSPP.

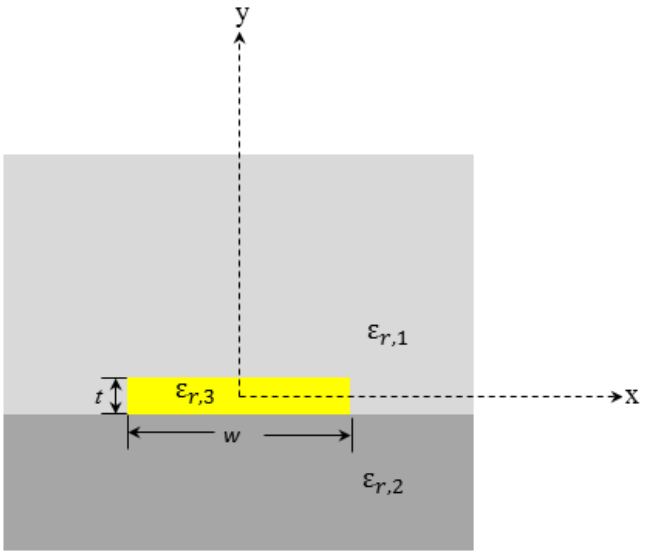

Figure 11 : A cross-section of a waveguide of thickness *t*, width *w* and permittivity $\boldsymbol{\varepsilon_{r,3}}$ surrounded by two semi-infinite media with permittivity $\boldsymbol{\varepsilon_{r,1}}$ and $\boldsymbol{\varepsilon_{r,2}}$.

The dominant field peaks at the interfaces of the metal film. The field takes the Gaussian like shape along the x axis, while it decays exponentially along the y axis, which is one of the surface modes' characteristics, as seen in Figure 12. In order to allow the mode its full expansion, the claddings should be optically infinitely thick.

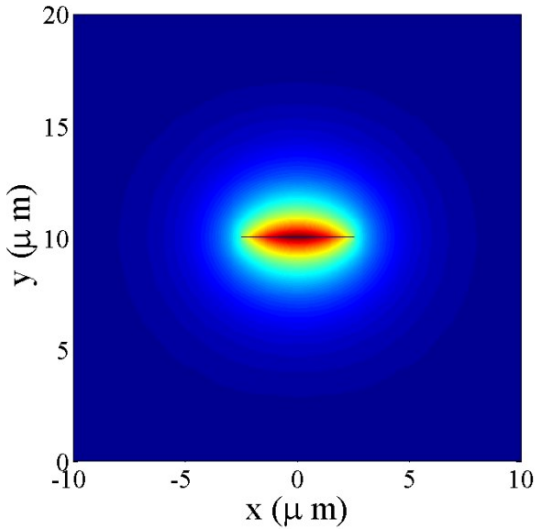

Figure 12: Field distribution for ss_b^0 mode supported by Au metal film of 35 nm thickness and 5 μm width surrounded by Cytop at 1310nm wavelength.

The performance of such waveguides is characterized by three attributes: confinement (or mode size), attenuation, and coupling efficiency to input and output means of interest. These attributes can be changed by modifying the thickness and the width of the metal film (geometry), the operating wavelength, and the materials used as the core and the claddings [46].

This study is concerned by LRSPP waveguides or, in other words, a waveguide that supports the ss_b^0 mode. LRSPP waveguides are characterized by low confinement and low propagation loss (loss is due to absorption in the metal) when comparing with other metal-dielectric waveguides [38].

The LRSPP waveguides are desirable in applications because they feature two dimensional confinement, the possibility of index modulation, sub-wavelength confinement and wave guiding, as well as large evanescent field volumes for optical sensing [38]. The applications vary between signal transmission and routing, and the construction of passive components such as couplers and power splitters.

2.2.2.1 ss_b Mode

In a symmetric structure ($\varepsilon_1 = \varepsilon_2$), when the metal film dimensions decrease (*t, w* → 0), the ss_b^0 mode evolves. Its field components E_y and $H_x$evolve from being confined and highly localized near the corners of a thick metal film to being distributed along the top and bottom boundaries in a Gaussian-like manner. With further thickness reduction, a coupling occurs between the fields at the top and bottom edges [20]. As all modes are supported by waveguides with finite width, the confinement is two dimensional. The effective field components for the ss_b^0 mode when the metal width is larger than the metal thickness are E_y and H_x, they exhibit a symmetric cross-sectional distribution. This field distribution facilitates the coupling between the mode's field and the single mode fiber field, which leads to efficient end-fire coupling. This ease in excitation makes this mode interesting for various applications [49]. The power for this mode is more in the claddings, where the field extends for a few micrometers.

In order for this mode to be supported, the structure must be symmetrical, or with a slight difference between the dielectric permittivity of the claddings [48]. For the ss_b^0 mode, as the thickness diminishes, the phase and the attenuation constants decrease, since the fields penetrate more deeply into the top and the bottom claddings and less into the metal [20]. The attenuation and the confinement are associated so that a decrease in attenuation is accompanied with a decrease in the mode field confinement to the wave guide core. The ss_b^0 mode does not have a cut-off thickness; it remains guided as $t \rightarrow 0$. Decreasing the width affects this mode by decreasing its attenuation, which is the opposite of decreasing the thickness. According to this, a proper selection of the metal film dimensions can make it the only long-range mode with acceptable attenuation [20].Thus, this attenuation renders the ss_b^0 mode long range, allowing it to be used in passive devices [50, 51]. In general, the metal stripe dimensions have a direct influence on the LRSPPs properties.

2.3 Waveguide Modeling

The modes in both the single interface and the optical slab can be obtained analytically, but in 2D waveguides a numerical method should be applied. The numerical method should be

accurate and reliable. The waveguides in this study are modeled numerically by using COMSOL multiphysics, which is a finite element analysis used to solve the mode in the frequency domain; COMSOL multiphysics involves discretization in the transverse domain, and it is formulated in rectangular coordinates with propagation occurring along the z axis.

COMSOL multiphysics can transform models described by underlying differential equations, which here are Maxwell's equations and the boundary conditions, as mentioned in section (2.1), into linear algebraic models via spatial discretisation. COMSOL multiphysics can provide the mode's field components across the wave guide cross-section (spatial distribution) and compute their propagation constant. In order to decrease the numerical effort and increase the accuracy of the results, the symmetry of the structure was exploited by placing a vertical magnetic wall along the y axis, which passes through the center of the metal film. A magnetic wall means that the tangential magnetic field is zero, however there can still be a normal magnetic field. The top and bottom boundaries should be placed far enough to resemble the infinity (openness of the structure) and the same situation should be applied to the lateral boundaries. Due to limits in the fabrication process, in this study the lower cladding was limited to thickness of 8 μm placed on a 2μm silicon substrate. Decreasing the cladding thickness leads to an increase in the propagation loss.

The result of solving the waveguide numerically gives the complex effective refractive index for the mode, which can be written as follows:

$$n_{eff} = \frac{\beta}{\beta_0} - i\,\frac{\alpha}{\beta_0} \tag{2.37}$$

where β/β_0 and α/β_0 are given in eqs. (2.35) and (2.36).

Throughout this research the propagation is taken to be along the $+z$ direction, which is directed out of the plane, and evolves according to $e^{-\gamma z}$.

2.3.1 Convergence

In order to determine the modes in two dimensional surface plasmon–polariton waveguides, a numerical method must be used. Due to the strong localization of mode fields and the large permittivity contrast between the metal and the dielectric, an accurate analysis is challenging

to obtain, and in order to claim accurate results, a convergence study is needed. Good results are achieved when they converge smoothly with decreasing mesh element size [52].

Generally, the mesh can be refined several times for a three layer structure (metal film with the dielectric claddings). The presence of thin layers in the structure makes it hard to apply the automatic mesh several times, because very fine mesh increases the effort and consumes time in the simulations. In this study, a thin layer is introduced above the metal film and its permittivity is defined depending on the calculations to eliminate any effects that could occur by changing the mesh in that area. Increasing the number of elements in the mesh makes the calculations expensive, as it consume a lot of memory and time.

The areas of the interest are the metal film, the thin layer, and the areas around them. A convergence study was done in order to identify a mesh able to provide reliable results. By default, the number of triangles in the vicinity of the film boundaries is the same as inside the metal film.

The convergence study is conducted by changing the mesh element size in the area of interest (the metal film).The element size is based on the height of the triangles along the vertical wall of the metal film. Within the metal region and its vicinity the mesh is uniform, as presented in Table 1.

Table 1: Normalized phase and attenuation constants for ss_b^0 mode supported by an Au waveguide of 35nm thickness and 3μm width at 1310nm.

Triangle height (nm)	$\boldsymbol{\beta/\beta_0}$	**MPA** (dB/mm)	$\boldsymbol{\alpha/\beta_0}$
0.79	1.336686	4.7317	1.136554×10^{-4}
1.59	1.336687	4.7319	1.136588×10^{-4}
2.33	1.336687	4.7321	1.136645×10^{-4}
3.2	1.336687	4.7324	1.136709×10^{-4}
3.9	1.336687	4.7326	1.1367676×10^{-4}
4.4	1.336687	4.7329	1.136829×10^{-4}
5.8	1.336687	4.7333	1.136934×10^{-4}

From the previous table, it is obvious that the values of the real part of the effective refractive indices converge rapidly, while the attenuation converges more slowly. The accuracy of the forthcoming grating computations requires 6 decimals in the real part and 4 decimals in the imaginary part of the effective index. We then introduced a thin adlayer on top of the metal film (discussed further in Chapter 4), and sought a suitable mesh. We started with 1nm for the maximum element size inside the metal film and the thin layer. This is believed to be the smallest element size that could be applied with the available computer. With this mesh the simulations were expensive, thus the maximum element size was increased gradually, comparing the result at each mesh. A maximum element size of 3 nm in the metal film and 2 nm within the thin layer gives an identical result to the maximum element size of 1nm for the real part of the effective refractive index.

2.3.2 Modeling Results

The materials chosen for the designs are: Gold (Au) as the metal film, Cytop as the claddings, and Si as a substrate (removed when 850 nm is the operating wavelength). The operating wavelengths are 850, 1310, and 1550 nm. The choice of materials is based on their properties and on the previous work of the group, as explained in chapter 4 of this thesis. The refractive index for Au is obtained from [53], where the refractive index of H_2O is obtained from [54].

In the study the metal film thicknesses are nanometric and the widths are micrometric. The thicknesses used are 20 nm, 35 nm, and 40 nm. In each waveguide, the fundamental ss_b^0 mode is defined by the complex effective refractive index, which is used for further calculations. We started each set of waveguide calculations with the smallest width that supports the desired mode, then increased the width gradually to a specific width (*e.g.* the largest width at λ = 850 nm is 2 μm and at λ = 1310 nm is 5 μm).

Table 2: Dispersion characteristics of finite width metal waveguide comprised of 35 nm thickness Au film embedded in Cytop at different wavelengths.

Wavelength (nm)	**Waveguide width** (μm)	**Effective refractive index**
850	0.5	$1.338442 - i\ 4.56435 \times 10^{-5}$
	0.75	$1.339974 - i\ 1.352144 \times 10^{-4}$
	1	$1.341917 - i\ 2.177551 \times 10^{-4}$
	1.25	$1.343753 - i\ 2.77174 \times 10^{-4}$
	1.5	$1.345315 - i\ 3.18146 \times 10^{-4}$
	1.75	$1.346599 - i\ 3.465548 \times 10^{-4}$
	2	$1.347646 - i\ 3.666236 \times 10^{-4}$
1310	1	$1.334523 - i\ 1.24628 \times 10^{-5}$
	2	$1.335491 - i\ 6.42274 \times 10^{-5}$
	3	$1.336686 - i\ 1.136554 \times 10^{-4}$
	4	$1.37655 - i\ 1.432185 \times 10^{-4}$
	5	$1.338361 - i\ 1.600725 \times 10^{-4}$
1550	1	$1.332887 - I\ 5.228238 \times 10^{-6}$
	2	$1.333298 - i\ 2.712563 \times 10^{-5}$
	3	$1.333915 - i\ 5.69801 \times 10^{-5}$
	4	$1.334536 - i\ 8.212771 \times 10^{-5}$
	5	$1.335067 - i\ 9.984718 \times 10^{-5}$
	6	$1.335496 - i\ 1.118675 \times 10^{-4}$
	7	$1.335835 - i\ 1.200709 \times 10^{-4}$
	8	$1.336105 - i\ 1.257707 \times 10^{-4}$

At each wavelength, among the set of widths we can see that the normalized phase constant (β/β_0) increases with increasing width as well as the normalized attenuation constant (α/β_0), as observed in Figure 13. At the smallest width, the mode is weakly confined to the metal film, but when we widen the film, the mode is more tightly bound to the film; this leads to higher confinement and a smaller spot size. By further increasing the width, the spot size became almost identical to the waveguide width, which is taken as the largest width for the metal film at a certain wavelength. The mode field profile changes from circular to more elliptical when increasing the width. When the mode is tightly confined to the metal film and less expanded in the dielectric, less computational domain is needed, thus the modeling

time is shorter. Table 2 shows that the effective refractive indices for the ss_b^0 mode are very close to the refractive index of the bounding material (the refractive index of Cytop is taken as 1.338, 1.3348, and 1.3335 at wavelengths of 850, 1310, and 1550 nm, respectively).

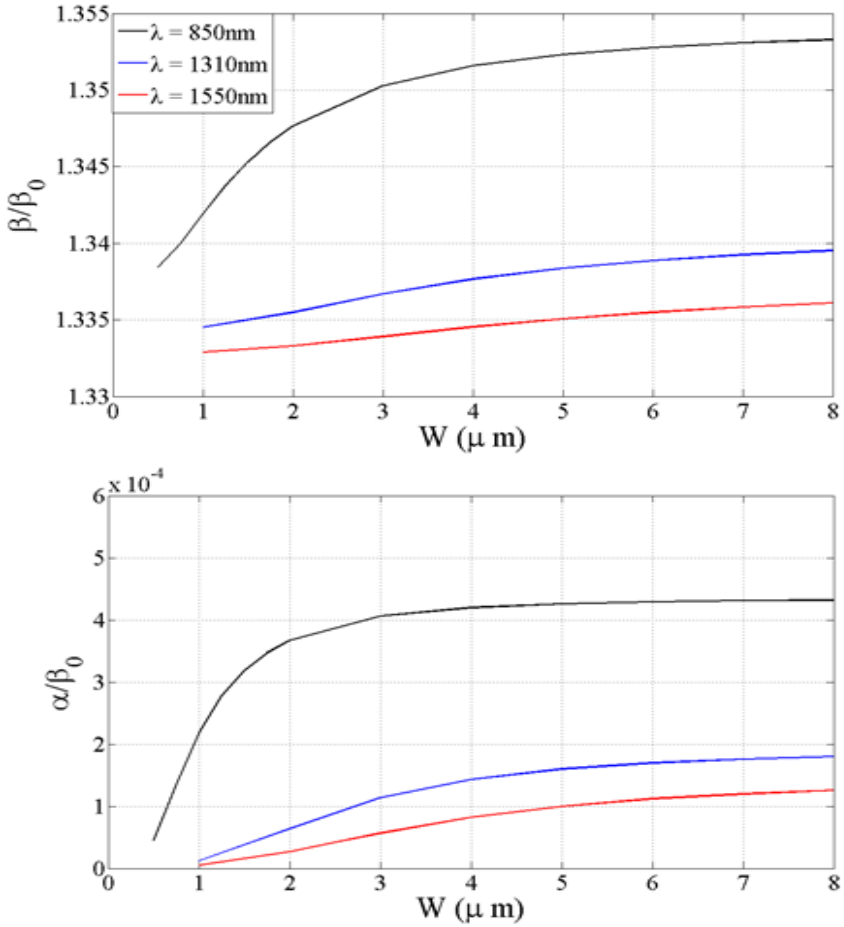

Figure 13: Dispersion characteristics for t = 35 nm Au film at different wavelengths.

The performance of the LRSPP waveguides differs with varying wavelengths. For a fixed width at different operating wavelengths, the effective refractive index for the ss_b^0 mode appears to decrease when the wavelength increase meaning that the modes become less confined to the metal and exhibit higher attenuation. Figure 14 offers a comparison of the ss_b^0 modes for different waveguides widths at various wavelengths.

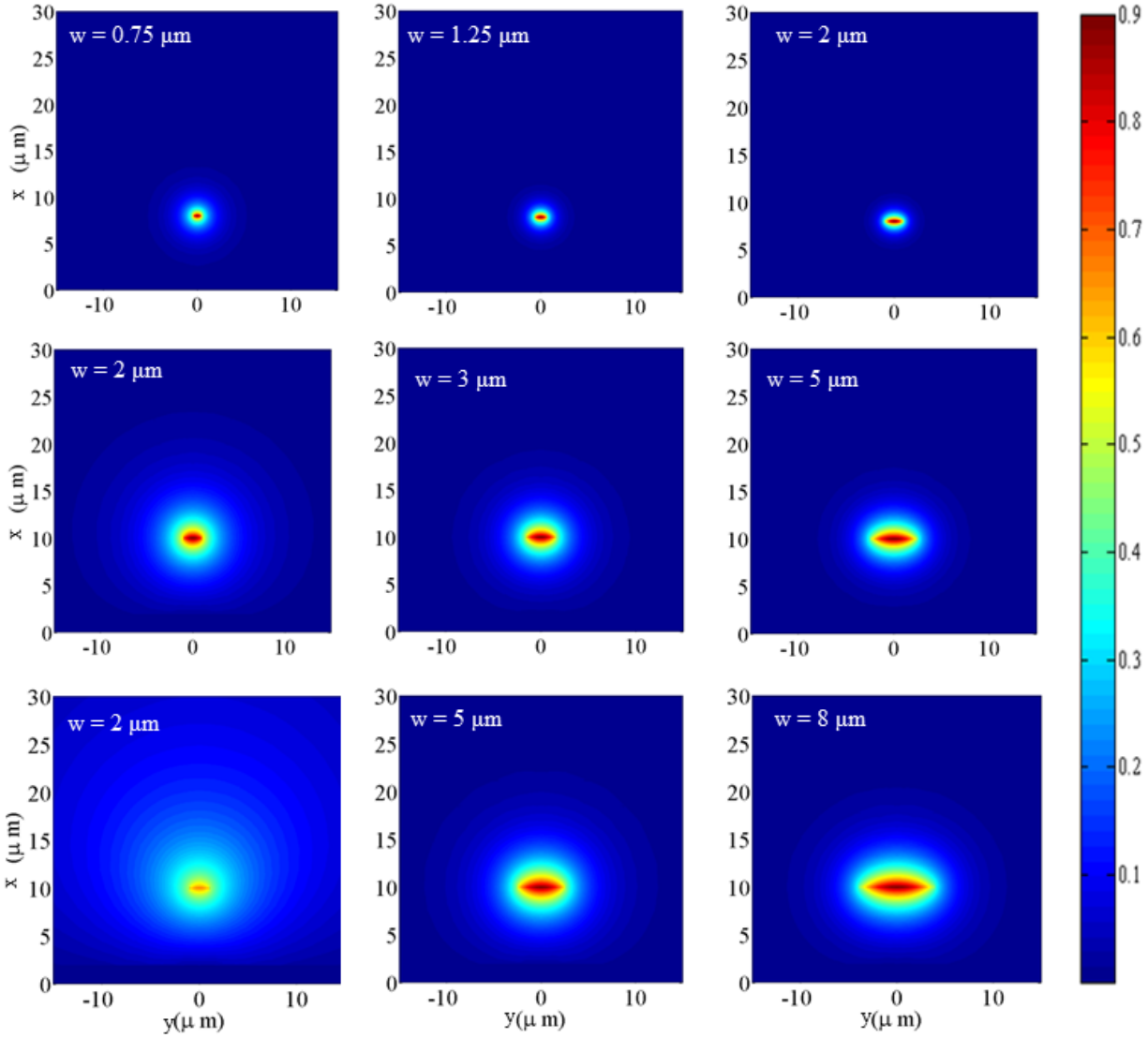

Figure 14: Mosaic of ss_b^0 mode for Au film of thickness 35 nm shows the variation in this mode with changing widths and wavelengths. E_y is plotted as a function of the metal stripe width over different wavelengths. First row is for λ = 850 nm, second row is for λ = 1310 nm, and third row is for λ = 1550 nm.

In Figure 15, the dominant field E_y is plotted as a function of the metal strip width. It is noticed that the field extends further into the bounding media in the case of small widths, meaning that the confinement increases when increasing the width. Decreasing the width is associated to a decrease in attenuation [20]. It is also noticed that the mode field profile changes from circular at small widths to elliptical with wider stripes, in order to follow the shape of the metal stripe. In addition, over a range of wavelengths, the mode field spreads further in the bounding media as the wavelength increases, meaning that the confinement increases with shorter wavelengths.

The calculations were repeated for the other metal film thicknesses (20nm and 40 nm); see Table 3.

Table 3: Effective refractive indices for Au stripes of different thicknesses and widths at λ = 1310 nm.

Thickness (nm)	**Width** (μm)	**Effective refractive index**
20	1	1.334336- i 1.212832× 10^{-6}
	2	1.33456- i 5.990562× 10^{-6}
	3	1.334907-i 1.2982065× 10^{-5}
	4	1.335273-i 1.92974× 10^{-5}
	5	1.335599-i 2.399244× 10^{-5}
35	1	1.334523- i 1.24628 × 10^{-5}
	2	1.335491- i 6.42274× 10^{-5}
	3	1.336686- i 1.136554× 10^{-4}
	4	1.337655- i 1.432185× 10^{-4}
	5	1.338361-i 1.600725× 10^{-4}
40	1	1.334619- i 2.16438 × 10^{-5}
	2	1.335935- i 1.058243× 10^{-4}
	3	1.337425- i1.752574× 10^{-4}
	4	1.338555-i 2.134434× 10^{-4}
	5	1.339352- i 2.34398× 10^{-4}

As seen from the results presented in Table 3, the effective refractive index increases with increasing thickness, causing the mode to be more confined to the metal film and exhibiting

higher attenuation. The results for thicknesses of 35 and 40 nm are very similar. At a thickness of 20 nm, the mode is less confined and extends more in the claddings, which results in lower sensitivity. Because of these results, metal films with a thickness of 35 nm are adopted for this study. The selection of 35 nm as the thickness is obtained from [51], where this thickness and a width of 5 μm were found to be good choices for stripe dimensions. A stripe with these dimensions supports only the fundamental mode with acceptable attenuation.

2.3.3 Mode Power Attenuation

To evaluate the performance of the waveguides, the calculations outlined below are necessary. The mode power attenuation (MPA), which is the power loss per unit length in (dB/mm) can be derived from the attenuation constant α (m^{-1}) using the following equation [41]:

$$MPA = \alpha \frac{20}{1000} \log_{10} e \tag{2.38}$$

The attenuation is related to the confinement, which is represented in the real part of the effective refractive index. Increasing confinement is accompanied by increasing attenuation. The mode power attenuation can be used to evaluate and compare the performance of waveguides operating at different wavelengths. Also, a comparison between waveguides with different architectures or comprised of different materials can be made using the ratio of the MPA [55].

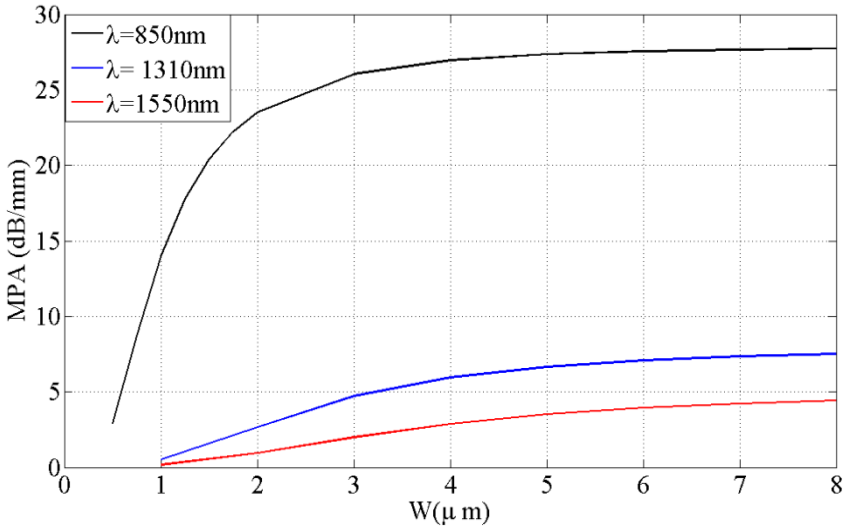

Figure 15: Mode power attenuation for step in width waveguides composed of 35 nm thickness Au film embedded in Cytop and H_2O, operated under various wavelengths.

Figure 15 shows that the attenuation increases with an increasing width; the confinement therefore also increases with this trend. Another way to represent the waveguide attenuation is by the attenuation constant (α) seen in Figure 16.

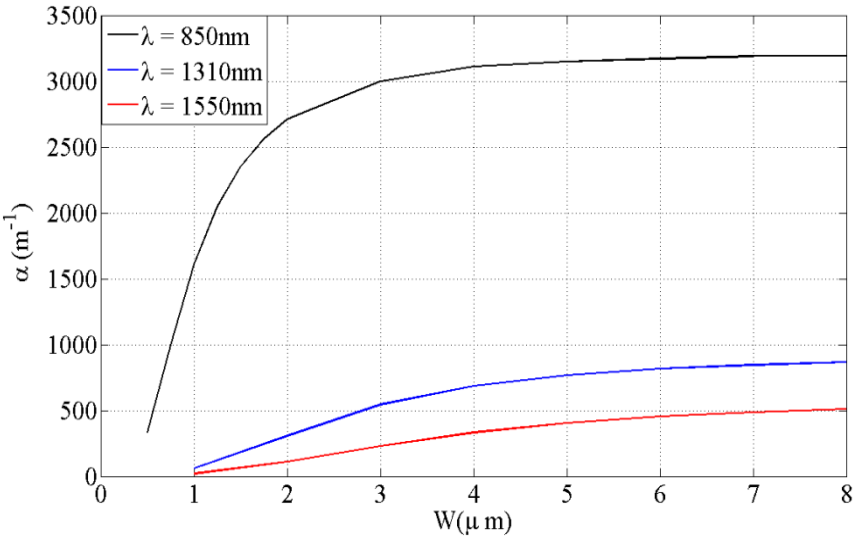

Figure 16: Attenuation constant for step in width waveguides composed of 35 nm thickness Au film embedded in Cytop and H_2O, operated under various wavelengths.

2.3.4 Coupling Efficiency

Another attribute that helps evaluate the performance of waveguides is the coupling efficiency. The method of excitation should be taken into account when assessing the coupling efficiency; in this case a centered, butt-coupled, and polarization maintaining single mode fiber is used. To excite the ss_b^0 mode, a maximum overlap should occur between the mode and the fiber fields. The selection of the stripe dimensions has a large impact on the coupling efficiency since these dimensions should provide a field distribution for the mode of interest that matches, as much as possible, the field of the single mode fiber used to ensure an efficient end fire excitation. The coupling efficiency here is computed with respect to single mode fibers that differ according to the free-space wavelength used. The fibers assumed are PM780-HP (core diameter 4.5μm, Nufern), PM-SMF (core diameter 7 μm, OZ optics), and SMF-28 (core diameter 8.2 μm, Corning) for free space wavelengths 850, 1310, and 1550 nm respectively. Figure 17 shows the field distribution for these fibers.

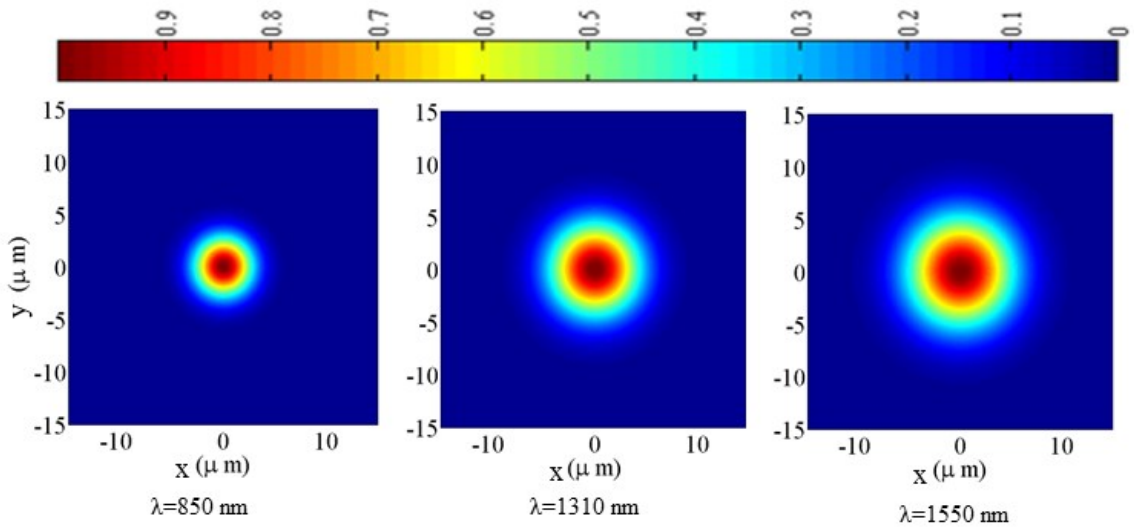

Figure 17: Field distribution for polarized optical fibers used to excite ss_b^0 mode at different wavelengths.

The first step in determining the coupling efficiency is computing the overlap factor *C* of the modes from the transverse spatial distribution of the main transverse electric field components of the two modes, E_{y1} and E_{y2}, using:

$$C = \frac{\iint E_{y1}.E_{y2}^{*}\,dA}{\sqrt{(\iint E_{y1}.E_{y1}^{*}\,dA)(\iint E_{y2}.E_{y2}^{*}\,dA)}} \tag{2.39}$$

where E_{y1} is the *y*-component of the electric field of the mode supported by the waveguide and computed numerically using COMSOL, and E_{y2} is the *y*-component of the electric field of the mode supported by the fiber and is modeled as a simple Gaussian distribution centered on the wave guide of interest.

The integrals in the previous equation cover the entire computational domain at the transverse plane where the coupling occurs. E_y is selected since it is the field component that dominates in the ss_b^0 mode for the waveguide considered here (w>>t).

The E_{y2} field is given by:

$$E_{y_2} = \exp\left[\frac{-x^2-(y-t/2)^2}{r_f^2}\right] \tag{2.40}$$

where r_f is the mode field radius and is given by:

$$r_f = a\left(0.65 + \frac{1.619}{V^{3/2}} + \frac{2.879}{V^6}\right) \tag{2.41}$$

The V parameter is given by:

$$\mathrm{V} = \frac{2\pi a}{\lambda_0}\,\mathrm{NA} \tag{2.42}$$

The parameters *a* and NA are the fiber core radius and the numerical aperture (NA=0.12), respectively. The coupling efficiency is given by $|C|^2$ assuming there is no discontinuity in the material at the coupling plane. The coupling efficiency is presented as a percentage. The mode power coupling loss C_{cpl} is given by [46, 48]:

$$C_{cpl} = -20\ log_{10}\ |C| \tag{2.43}$$

The selection of a proper stripe dimensions has a large impact on the coupling efficiency. The dimensions of the stripe should support the ss_b^0 mode in order to have a field distribution that matches as much as possible the field of the single mode fiber, to ensure an efficient end fire excitation; see Figures 18 and 19.

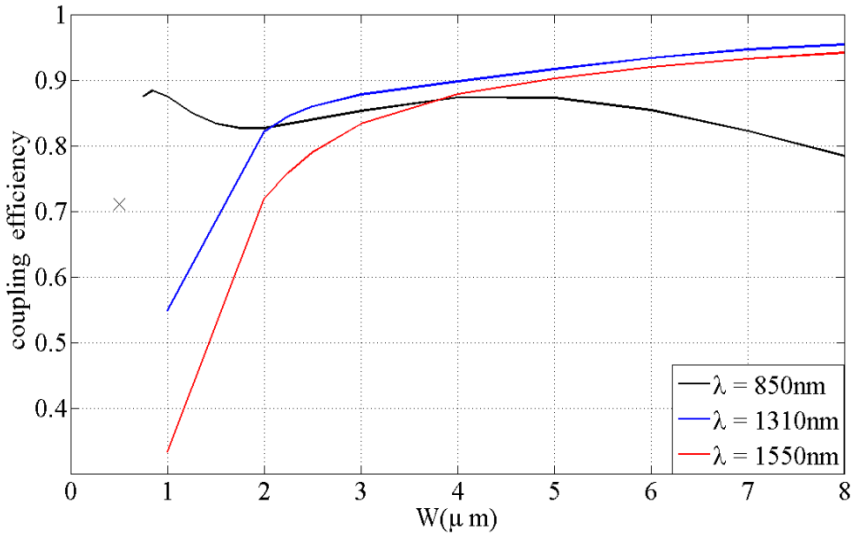

Figure 18: Coupling efficiency for an Au stripe of thickness 35 nm with various widths at several wavelengths. Point (x) represents the coupling efficiency at $w = 0.75$ μm and $\lambda = 850$ nm.

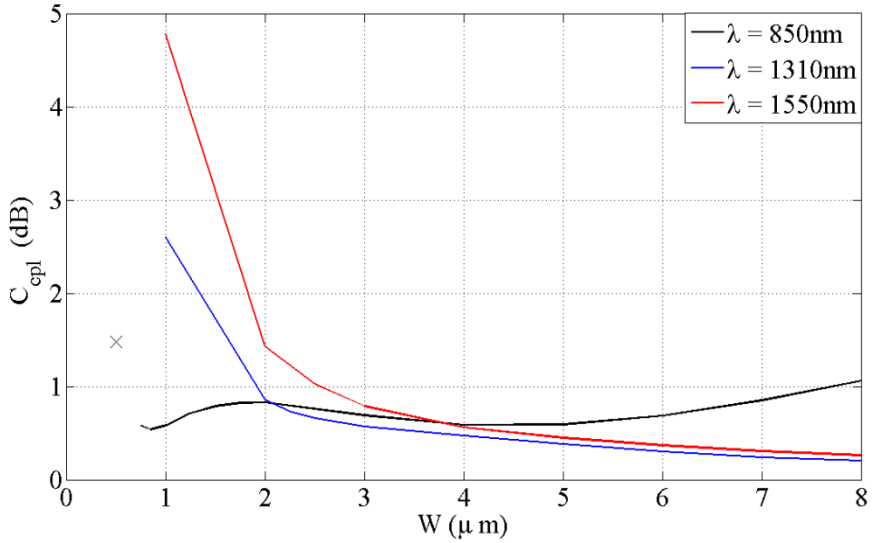

Figure 19: The mode power coupling loss for Au stripe of 35 nm thickness and increasing width under various operating wavelengths. Point (x) represents the power coupling loss at $w = 0.75$ μm $\lambda = 850$ nm.

The values of the overlap change according to the size of the mode field. At λ = 1310, 1550 nm, the coupling efficiency has low values with small widths, because the modes' fields are large and extend more into the bounding media than the that of wider widths. The coupling efficiency increases as the modes become more confined. However, at λ = 850 nm, the largest coupling is at w = 0.75 μm. Figure 19 shows the mode power coupling loss, which is the power loss that occurs during coupling. According to this, the power coupling loss is the opposite of the coupling efficiency, meaning that a high coupling leads to a low power coupling loss.

Chapter 3 Plasmon – Polariton Bragg Gratings

This Chapter contains an overview of long range surface plasmon polariton Bragg gratings (PPBGs), the method used to model the gratings, the designs used for this thesis work, the performance characteristics of PPBGs, and a comparison between different designs.

A grating is a structure with regularly spaced periodic elements. When the "elements" that construct a grating in fiber, is a periodic index modulations spaced less than half a micrometer apart, the grating is called a fiber Bragg grating (FBG) [56]. The finite width waveguides used in the previous chapter are used here to construct gratings. The use of this kind of waveguide to construct LRSPP Bragg gratings was proposed in [10, 34]. They will be referred to as PPBGs.

The grating concept in this study depends on patterning LRSPP waveguides with two alternating widths but a constant thickness, over a certain length and in a periodic manner.

3.1 General Theory of Bragg Gratings

Qualitatively, PPBGs operate in the same manner as FBG. In FBGs, light is launched into the structure; it will then suffer from perturbations along the structure at each transition, due to changes in the refractive index of the fiber. These perturbations will cause micro reflections of the incident wave, the micro-reflections will combine constructively to create a reflected wave, and the rest of the incident light will appear at the output as a transmitted wave. In a PPBG the perturbations are introduced by stepping the width of the waveguide, rather than by photo-inducing changes in the refractive index as in FBGs.

There are some quantities that can help provide a general idea of how a generic Bragg grating operates and enables a better understanding of the concept of a grating.

3.1.1 Reflectance and Transmittance

The reflectance and transmittance of a grating can be obtained from the reflection and transmission coefficients respectively. The reflection coefficient of a grating *r* is the ratio of the reflected electric field to the incident electric field, which can be written as the following equation:

$$r = \left[\frac{E_0^{ref}}{E_0^{inc}}\right]_{E_s^{ref}=0} \tag{3.1}$$

where E_0^{inc} and E_0^{ref} are the incident and reflected waves respectively, and E_s^{ref} is the electric field incident onto the output of the grating from the second semi-infinite dielectric medium. It is set to zero (no light is injected therein). The transmission coefficient *t* can be obtained from a similar expression:

$$t = \left[\frac{E_s^{trn}}{E_0^{inc}}\right]_{E_s^{ref}=0} \tag{3.2}$$

where E_s^{trn} is the incident electric field on the semi-infinite dielectric at the output of the grating. According to the equation, the transmission coefficient is defined as the ratio of the transmitted electric field to the incident electric field.

The reflectance and transmittance of the grating can be obtained from the reflection and transmission coefficients, as follows:

$$R = |r|^2 \tag{3. 3}$$

$$T = \frac{n_s \cos\theta_s}{n_0 \cos\theta_0} |t|^2 \tag{3. 4}$$

where n_0 and n_s are the refractive indices of the semi-infinite bounding materials at the input and the output respectively, and θ_0 and θ_s are the angles of incidence and transmission respectively and are taken to be normal to the direction of propagation, as seen in Figure 20. The reflectance equation can be applied to real or complex refractive indices, where the transmittance equation is true only if the indices of the bounding media are real and both incident and transmitted waves have real propagation vectors. If the bounding media have a

complex refractive index, the transmittance equation can be applied only if the two bounding media are identical (matched), meaning that $n_0 = n_s \; and \; \theta_0 = \theta_s$. If the condition is satisfied, the transmittance equation can be simplified as follows [10, 57] :

$$T = |t|^2 \tag{3. 5}$$

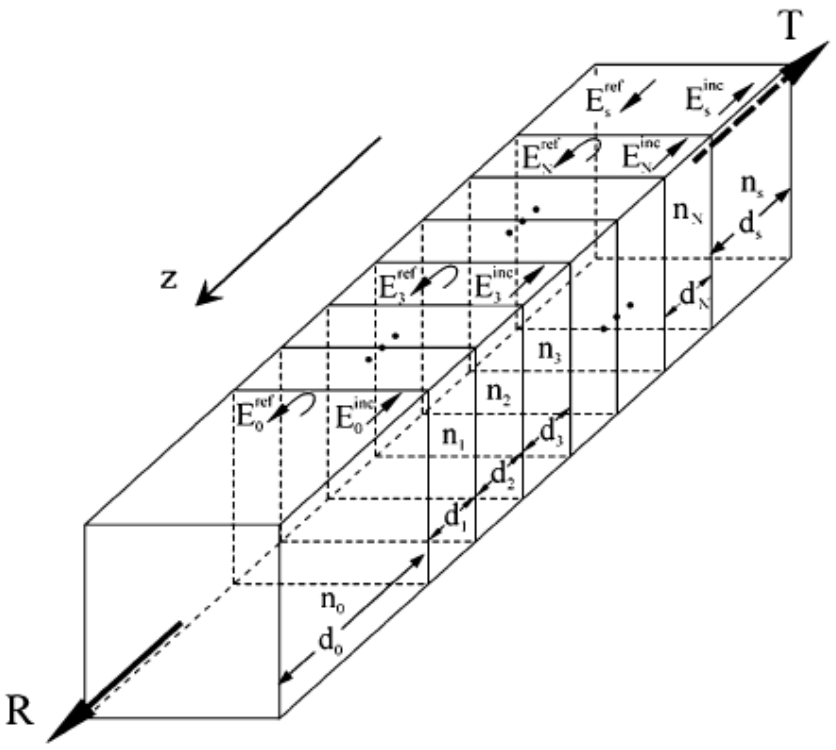

Figure 20: A model of a grating shows the directions of the reflected and transmitted waves and the bounding media n_o and n_s. Adopted from [34], (0018-9197© 2005 IEEE).

3.1.2 Bragg wavelength λ_B

The Bragg wavelength is defined as the central wavelength of the grating, representing the wavelength with the maximum reflectivity. It is proportional to the period of index modulation, and defined by the following equation:

$$\lambda_B = \frac{2\, n_{eff}\, \Lambda}{O} \tag{3. 6}$$

where O is an integer ($O \geq 1$) and represents the order of the grating, n_{eff} is the effective refractive index of the grating, and Λ is the pitch of the grating [56, 58].

3.1.3 The Pitch Λ

The pitch is the period of the gratings and it determines the Bragg wavelength. For uniform periodic PPBGs it is defined as:

$$\Lambda = d_1 + d_2 \tag{3.7}$$

where d_1 and d_2 are the lengths of the elements constructing the gratings.

3.1.4 Duty Cycle dc

This quantity represents the weight or division of the grating pitch, Λ, between the two elements that create the perturbation (two materials or two sections with different refractive index values). The duty cycle is usually represented as a percentage and given by the following equation [59]:

$$dc = \frac{d_1}{\Lambda} \times 100(\%) \tag{3.8}$$

where d_1 is the length of the wave guide section of refractive index $n_1$of the fundamental cell of a uniform periodic grating, and Λ is the grating pitch. The duty cycle and the pitch are related through the following equation [10, 60]:

$$\Lambda n_{eff} = n_1\, d_1 + n_2\, d_2 \tag{3.9}$$

Any change in the duty cycle can affect the Bragg wavelength. By combining the previous equation with the λ_B equation, we get a clear relation between the duty cycle and the Bragg wavelength:

$$\lambda_B = \frac{2(n_1\, d_1 + n_2\, d_2)}{O} \tag{3.10}$$

3.1.5 Bandwidth

The bandwidth represents the spectral width of the grating. It has several definitions such as the distance between the first minima on both sides of the main peak [58], or the full width

at half maximum, FWHM. There are two ways to get the bandwidth, either on the linear scale of the reflection spectrum or on the log scale. In the case of the linear scale, it is the width of the spectrum at the half maximum reflection point, whereas for the log scale, it is the width of the spectrum at 3 dB below the maximum reflection point [10]. In this study it is better to have a small bandwidth in order to facilitate the tracking of the signal during biosensing study.

3.2 Surface Plasmon Polariton Bragg Gratings (PPBGs)

Bragg gratings based on plasmon polaritons are constructed by combining a number of LRSPP waveguides that feature different physical characteristics in order to create transitions between the neighboring sections. These transitions cause perturbations for the travelling wave and result in the formation of partial reflections at the interfaces between the adjacent sections. If the design parameters are selected properly, the partial reflections along the grating will combine constructively to form a Bragg reflection [10, 34, 59]. An interesting property of PPBGs is that they are used to guide the optical signal and to transmit it [33].

The waveguides that assemble the grating must differ in their physical characteristics (such as width, thickness, etc.) or their outer profile to create a perturbation. The variations in the physical characteristics lead to different dispersion characteristics for each section, as was demonstrated in Chapter 2. Combining two LRSPPs waveguide sections with different widths will create a perturbation in the effective refractive index of the ss_b^0 mode along the grating, creating plasmon polariton Bragg gratings [10, 34].

The gratings investigated in this study are uniform periodic Bragg gratings. This type of grating is constructed by creating a pattern of waveguides with different widths w along the direction of propagation over a certain length L to create a physical perturbation, or by creating a pattern of waveguides of a certain width with a gap filled with the surrounding dielectric. The latter case is not included in this study. In this study, the uniform periodic PPBGs are composed of two waveguides with a finite width and a constant thickness. Each

waveguide has a certain width w_1 and w_2 . These waveguides are constructed by varying the width periodically along the direction of propagation z, as shown in Figure 21. The dimensions of the waveguides should be selected properly to ensure the occurrence of the reflection at the desired operating wavelength.

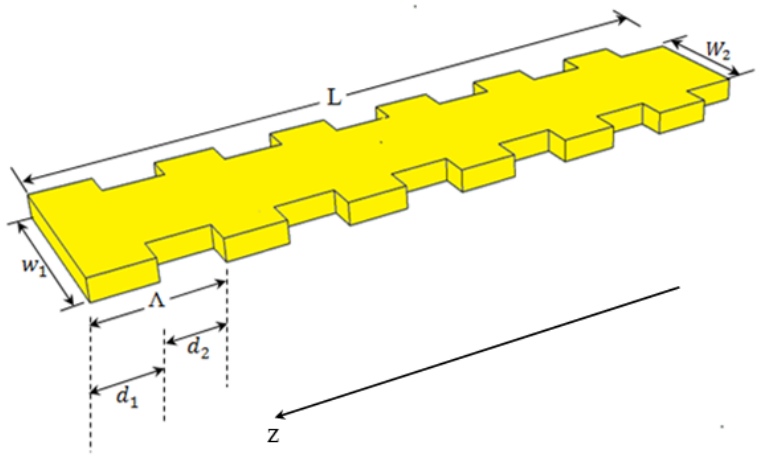

Figure 21: Schematic of PPBGs based on finite width LRSPP waveguides.

In an ideal grating, light is launched longitudinally in the *z* direction into the input using an end-fire technique, and will undergo partial reflection at each step of grating. A portion of the reflected light (partial reflections) will combine constructively to form a reflected wave at the Bragg wavelength. The reflected wave will travel along the grating to the input, while the rest of the incident light will form a transmitted wave at the output of the structure [34, 59], see Figure 22.

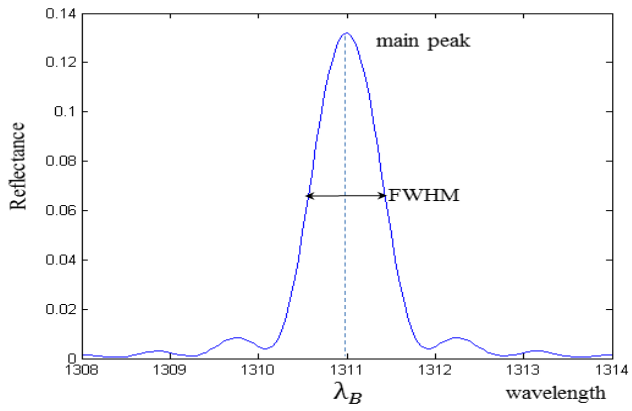

Figure 22: Reflection spectrum of Bragg gratings with Bragg wavelength and FWHM.

The previous figure is generated by a technique to be discussed later. From the figure, it is noted that the main peak is central and surrounded on both sides by a number of subpeaks (sidelobes), this attribute is a characteristic of the uniform period gratings of finite width. These sidelobes are a result of the sharp start and end of the grating, as well as the outer profile of the gratings. Hence, sidelobes are always associated with uniform period index-modulation gratings [56].

In PPBGs, the reflected and transmitted waves are propagating longitudinally along the structure as it is a waveguide grating. The spectral response represented in the reflected and the transmitted waves can be collected via access waveguides [35].

In the previous chapter it was demonstrated that the dispersion characteristics differ with changing waveguides dimensions, *e.g.* width. The lowest value of the effective refractive index for the ss_b^0 mode is obtained with the smallest width, and the highest value is obtained with the largest width. This periodic change in the effective refractive index of the ss_b^0 mode along the structure of the gratings results in induced reflection at and near the Bragg wavelength λ_B .

Since the effective refractive index for the mode of interest here is very close to the refractive index of the bounding media, the change in the effective refractive index when changing the width is small, this leads to weak grating [10, 34].

Since a grating is a periodic concatenation of waveguides, it can be considered as a number of cells *N* where each cell is formed of two waveguides having widths w_1 and w_2, lengths d_1 and d_2, and effective refractive indices $n_{eff,1}$ and $n_{eff,2}$ respectively.

To identify gratings with different designs, a terminology was proposed by Jetté [35], to refer and identify the fundamental cell. A capital c is used to refer to the "fundamental cell" followed by two numbers representing the widths of the waveguides forming the fundamental cell. The first number indicates the width of the waveguide with the higher effective refractive index, and the second the width of the other waveguide.

3.3 Selection of the Grating Parameters

The parameters presented in section 3.1 are also used in this section, with slight changes imposed by using the average effective refractive index n_{ave} instead of using refractive indices directly, such as in the Bragg wavelength equation:

$$\lambda_B = \frac{2\, n_{ave}\, \Lambda}{O} \tag{3.11}$$

where n_{ave} is the average real effective refractive index of the ss_b^0 mode supported by the waveguides comprising the grating and is given by:

$$n_{ave} = \frac{Re\{n_{eff,1}\}d_1 + Re\{n_{eff,2}\}d_2}{\Lambda} \tag{3.12}$$

$n_{eff,1}$ and $n_{eff,2}$ are the complex effective refractive indices of the ss_b^0 modes supported by the waveguide sections comprising the grating and d_1 and d_2 are the lengths of these sections, respectively. If n_{ave} is fixed, then the Bragg wavelength is determined by the grating order and the pitch.

Since this quantity depends on the pitch Λ, then it affects the center wavelength of the grating (the Bragg wavelength). Considering only the real part of the effective refractive

indices when calculating the average effective refractive index is acceptable since the imaginary part of the ss_b^0 mode is small in comparison with the real part [59].

3.3.1 The Grating Length *L*

The grating length is defined by the number of periods, *N*, according to the following equation:

$$L = N\Lambda \tag{3.13}$$

For a PPBG, increasing the length of the grating by increasing the number of cells will result in an increased reflectance. The increasing reflectance continues until it reaches a saturation point, where increasing the length of the grating no longer has an impact on the reflectance, as seen in Figure 23. The maximum reflectance is always less than one, since the gratings are based on lossy metal films. The saturation point in the curve represents the maximum length that should be used for the gratings L_{max} . Past the maximum length, the micro reflections that exist at each refractive index perturbation will be cancelled due to the waveguide attenuation.

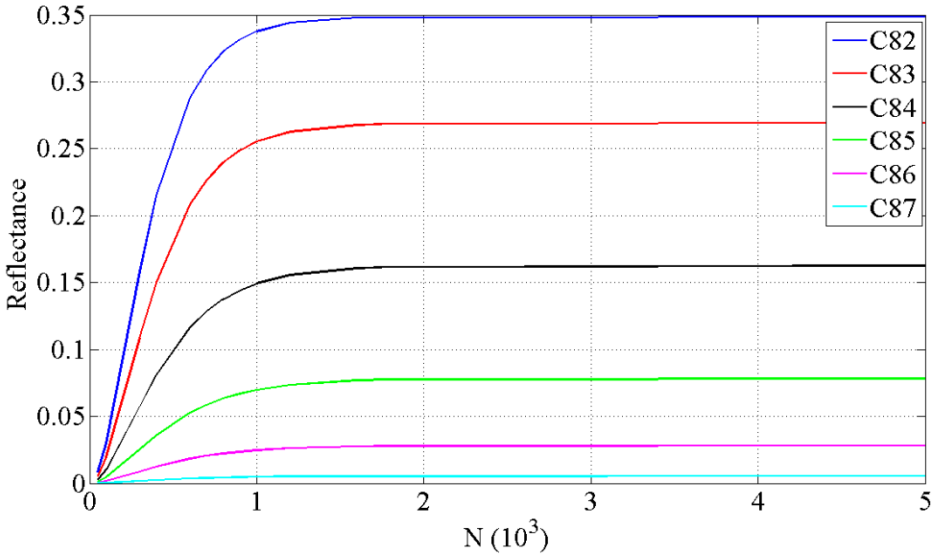

Figure 23: reflectance versus number of cells for different PPBGs designs. In all designs the fundamental cell is consisted of Au waveguide of 35 nm thickness, the first waveguide width is fixed at 8 µm and the second is varied from 2 µm to 7 µm. The pitch is fixed at 1740 nm and the duty cycle is 50%. The gratings modeled at λ = 1550 nm.

Figure 23 shows that for different designs, the increment in *N* leads to increments in the reflectance, until the length of the PPBGs reaches the saturation point which is represented in Figure 23 by a skew. The saturation point differs with different designs. In this study, the lengths of different gratings are taken to attain approximately 90 to 95% of the maximum reflection.

It is noted that the location of the saturation point differs with different designs. It is reached sooner for stronger designs (short gratings), and requires a larger number of cells in the case of weak gratings (*e.g.* for a fixed percentage of total reflectance, the number of cells will increase for weaker designs. The required number of cells to attain 95% of the total reflectance for the designs of C82, C85, and C87 at λ = 1550 nm are 900, 1300, 1450 respectively); this is because the two waveguides comprising the fundamental cell at the weaker gratings suffer from higher loss than stronger gratings do.

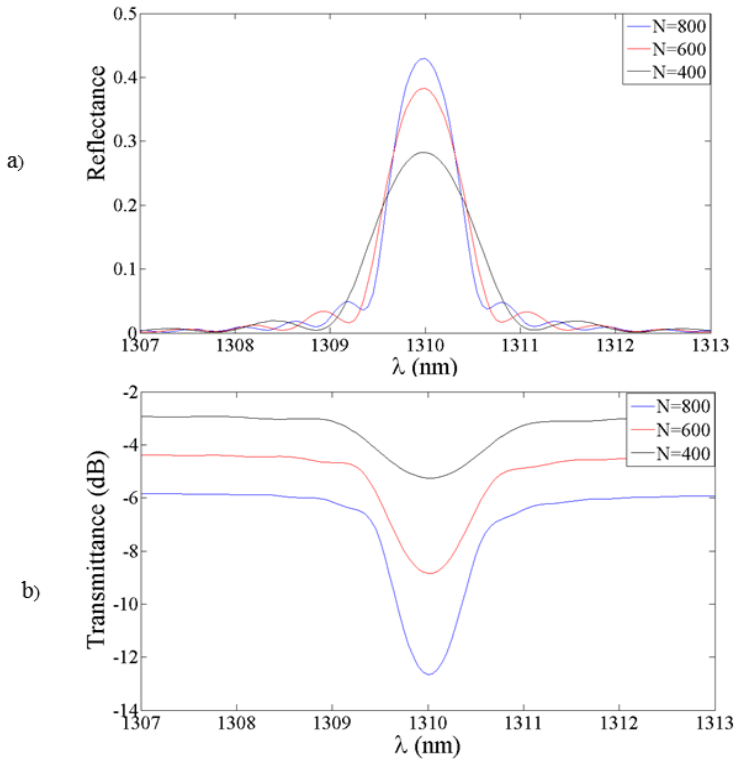

Figure 24: Wavelength spectra for third order uniform periodic PPBGs with fundamental cell design of C52 operated at wavelength of 1310 nm with different number of cells N, the duty cycle is 50% and the pitch is fixed at 1470 nm, (a) shows the reflectance spectra, and (b) shows the transmittance spectra.

Figure 24 shows the influence of increasing the number of cells *N* on the wavelength response. For a fixed parameter in a certain design, it is noted that the reflectance increases when augmenting the grating length, and both the on- and off- resonance transmittance decrease when augmenting the length. The off-resonance decreases when augmenting the length, due to the increasing loss of the PPBGs. The decrease in the on-resonance is due to the strength of the grating. Augmenting the length leads to more reflection of the incident wave, thus less of the incident wave is transmitted. The length of the grating has an influence on FWHM; it gets narrower as the length increases.

3.3.2 The Length of the Waveguide Sections d_1 , d_2

There are three approaches that control the selection of the proper length of the waveguide sections [10]; the first approach is that the length of the fundamental cell depends on the quarter wave dimensions:

$$d_1 = \frac{\lambda_0}{4n_1} \tag{3.14}$$

and

$$d_1 = \frac{\lambda_0}{4n_2} \tag{3.15}$$

where λ_0 is the free-space wavelength. The second approach uses the optimized lengths d_1, d_2 which depend on two parameters called the optimization parameters B_{opt} and d_{opt}. They are selected to ensure the maximum intensity reflectance to occur at the desired Bragg wavelength, λ_B , the optimized lengths are defined as:

$$d_1 = \beta_{opt}\, d_{opt} \tag{3.16}$$

$$d_2 = (1 - \beta_{opt})\, d_{opt} \tag{3.17}$$

The third approach which is applied in this thesis work, exploits the relation between the pitch, the duty cycle and the lengths d_1 and d_2 in equations (3.7) and (3.8). In this thesis, the pitch is taken dividable by 5 in order to respect eventual fabrication by e-beam lithography, where the greatest accuracy with the available e-beam can be achieved at 5 nm.

3.3.3 The Grating Strength

The grating strength is determined by the modulation depth, which is defined by the following equation:

$$\Delta n = |n_1 - n_2| \tag{3.18}$$

The modulation depth of the grating Δn represents the strength of the perturbation of the effective refractive indices along the structure; the larger the modulation depth, the stronger the grating. Strong gratings offer strong reflectance. According to this, the maximum peak reflectance is achieved by combining a wide waveguide section with a gap or a narrow waveguide section. Since the indices depend on the waveguide dimensions, a proper selection of waveguides of the fundamental cell $w_1$and w_2 have a direct effect on the grating performance. To study the effect of this parameter, several designs were made by varying one of the widths and fixing both the Bragg wavelength and the duty cycle. The strongest grating can be achieved by combining waveguide sections with the largest and smallest widths. Figure 25 shows a comparison of different grating designs. They are composed by combining different widths of LRSPPs waveguides.

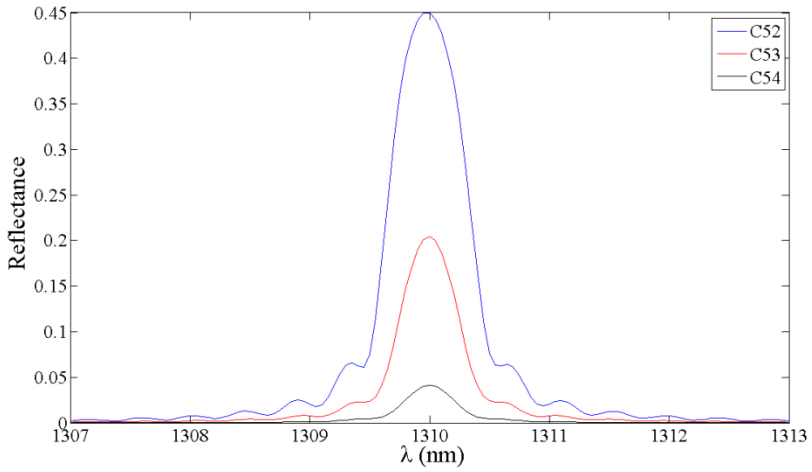

Figure 25: Reflectance spectra for uniform periodic third order PPBGs. Three designs are used C52, C53, and C54 modeled at 1310 free space wavelength. All designs have the same number of cells (1000) cells, and the duty cycle is 50%. The fundamental cell is comprised of a 35 nm thick Au film and embedded in H_2O and index matched polymer.

From the previous figure, it is noted that the PPBGs with a fundamental cell of C52 attain the highest reflection, while those with C54 attain the lowest reflection. Also, it is noted that the sidelobe levels increase with greater grating strength.

3.3.4 The Duty Cycle

The duty cycle is defined by equation (3.8). From the equation, in the case of fixed pitch, the duty cycle determines the length of the waveguide section of the fundamental cell. The selection of the duty cycle should consider the minimum feature size and the resolution of the fabrication process, in order to achieve the maximum reflectance. The effect of the duty cycle on the performance of the PPBGs was presented in [59], where it was shown that the duty cycle affects both the L_{max} and the reflectance peak at the saturation point. Increasing the duty cycle means increasing the length of the waveguide section d_1, and this leads to more loss introduced to the grating, thus reducing the maximum peak reflectance. The loss of the fundamental cell must be minimized in order to obtain the highest reflectance for the uniform periodic PPBGs, and this can be achieved by minimizing the duty cycle. The duty cycle in this study was fixed at 50%.

3.3.5 Bandwidth

The bandwidth of a uniform periodic grating depends on the width of the bandgap $\Delta\omega_g$ of the structure

$$\Delta\omega_g = \omega_B \frac{4}{\pi} \arcsin\left(\frac{\Delta n}{2n_{ave}}\right) \tag{3.19}$$

where ω_B is the Bragg radian frequency.

In the case of small modulations the equation can be simplified to

$$\Delta\omega_g \approx \omega_B \frac{2}{\pi} \frac{\Delta n}{n_{ave}} \tag{3.20}$$

In terms of a free space wavelength, the previous equation can be written as follows

$$\Delta\lambda_g = \lambda_B \frac{4}{O\pi} \arcsin\left(\frac{\Delta n_{eff}}{2n_{ave}}\right) \tag{3.21}$$

$$\Delta\lambda_g \approx \lambda_B \frac{2}{\pi} \frac{\Delta n}{n_{ave}} \tag{3.22}$$

The equations show the relation of the bandgap and the bandwidth with the modulation depth (grating strength) Δn and the average effective refractive index n_{ave}. The bandwidth is proportional to the grating strength, and inversely proportional to the average effective refractive index. Both parameters depend on the indices of the fundamental cell, thus the dimension of the waveguides comprising the fundamental cell. It is nonetheless possible to change one of these parameters without affecting the other [59].

3.4 Modeling PPBGs

3.4.1 Selection of Modeling Method

In order to design a grating, a model of the grating is required. From the previous chapter, it was clear that only numerical solutions are available for the modes supported by waveguides with finite width, and since these waveguides are essential elements in the formation of PPBGs, only numerical solutions can be obtained for this grating.

The fact that the mode field in the waveguides with finite width can be coupled effectively to a single mode fiber leads to the assumption that the method used in modeling fiber Bragg gratings can be applied to model plasmon polariton Bragg gratings [10].

Different methods are used to model FBGs, such as Coupled Mode Theory (CMT) [10, 58, 61, 62, 63, 64]. It provides the calculation of the reflectance and transmittance spectra, and it can be used with complex forms of Fiber Bragg gratings if the grating is treated as a series of small sections, each with constant period and specific refractive index modulation [58]. Another method is Rouard's method, which relies on dividing the gratings into sections of multilayers, where each layer is characterized by an effective complex reflectivity and replaced by a single interface that has the same reflectivity and phase change through the

layer (the same properties). The reflectivity in this method is calculated from the difference in the refractive index between two adjacent waveguides [58, 65]. A comparison study was done between the results of the Rouard's method and the Coupled Mode Theory, and resulted in excellent agreement, even though the Rouard's method is simpler and faster than CMT, since the entire gratings need to be solved in CMT [66]. There is also a method based on Gel'Fand-Levitan–Marchenko inverse scattering, it relies on the integral coupled equations and allows the gratings to be solved with particular characteristics, but it has the disadvantage of obscuring the problem being solved [58]. Another approach used to analyze the Fiber Bragg grating is the Floquet-Bloch method [67]. In this method, the stability diagram is used to study the reflection and transmission properties of gratings.

The wavelength response represented in reflection and transmittance of a longitudinal excitation is of interest for certain applications, especially if the PPBGs are used as a passive integrated device [34, 64].

It was determined that PPBGs can be modeled as a series of small sections mapped to a multilayer dielectric stack (equivalent thin film dielectric stack). Then, the wavelength response of the equivalent dielectric stack represented in the reflectance and the transmittance can be determined by using the transfer matrix method (TMM), based on Maxwell's equations [58, 34, 64].

3.4.1.1 Equivalent Dielectric Stack Model

Using an equivalent thin film dielectric stack is advantageous because it is a general approach and its generality allows it to handle any grating architecture, including the complex ones [10, 34, 57]. In the dielectric stack, each slice represents an individual grating section (waveguide) characterized by a refractive index, *n*, that matches the effective refractive index of the ss_b^0 mode, n_{eff} supported by the waveguide comprising the grating, and a length, *d*, that resembles the waveguide length. In other words, the grating structure is mapped to the dielectric stack, where each slice from the stack resembles a grating section. The dielectrics that bound the grating are represented in the stack as semi-infinite materials bounding the input and the output. Figure 20 shows an equivalent thin film stack model of

PPBGs. A length, d_i, and an effective refractive index, n characterize each slice of the stack. It is bounded by two semi-infinite materials of index $n_0 = n_s$ [10, 34].

A TEM wave is assumed normally incident on the dielectric stack along the direction of propagation +z. Modelling the ss_b^0 mode as a TEM wave is reasonable because as a weakly guided mode, its longitudinal fields are much smaller than the transverse ones.

The thin film stack can be solved, and its wavelength response can be obtained, by using the Transfer Matrix Method (TMM), this numerical approach is based on Maxwell's equations. The transfer matrix method carries the calculations of the reflectance and the transmittance of the gratings and allows the use of complex refractive indices throughout the stack [10, 34].

3.4.1.2 Transfer Matrix Method (TMM)

The TMM is an effective tool used to depict the propagation of electromagnetic fields along periodic structures [34, 58]. The spectral wavelength (reflectance and transmittance spectra) of gratings can be obtained by applying the formulation of TMM, and are related to the electric fields associated with incident. The waves transmitted and reflected by the relations are represented in equations (3.1) and (3.2) [34]. The TMM is applicable to lossy and lossless waveguides and appropriate to handle both bound and leaky modes [68].

In this method the periodic structure is treated as small segments. Each has fundamental matrices and the total transfer matrix for the whole structure is a multiplication of the individual transfer matrices for different segments by certain phase conditions of the grating [10, 59].

This method was treated in details in [10], based on the approach presented in [57]. The formulation in TMM is based on Maxwell's equations. In order to obtain the reflectance and the transmittance of the gratings, a solution for both the $\boldsymbol{H}$ and $\boldsymbol{E}$ fields should be found in each layer, and the complex amplitude of the waves at the input and the output should be represented using the reflectance and transmittance relations (3.3) and (3.4).

The complex field amplitude on either side of the dielectric boundary interface was defined through a matrix equation, and a relation between the complex amplitude of the electric field

at the input and the output was sought. It was found that the amplitudes at the input and the output are related with a sequence of 2×2 matrix multiplications. The result defined reflectance and transmittance respectively as following:

$$R = |r|^2 = \left|\frac{M_{21}}{M_{11}}\right|^2 \tag{3.23}$$

and

$$T = \frac{n_s cos(\theta_s)}{n_0 cos(\theta_0)} \left|\frac{1}{M_{11}}\right|^2 = \frac{n_s cos(\theta_s)}{n_0 cos(\theta_0)} |t|^2 \tag{3.24}$$

where n_0 and n_s are the refractive indices of the semi-infinite bounding materials at the input and the output respectively, θ_0 and θ_s are the incident and transmitted angles, and M_{ii} represents the elements of the M matrix. The M matrix is the product of the sub-matrices for the whole structure.

In the case of index matched bounding media, $n_0 = n_s$ and $\theta_0 = \theta_s$, the transmittance equation can be simplified to :

$$T = |t|^2 \tag{3.25}$$

For this thesis work, the formulation used was validated by reproducing some of the modeling results in [10], as seen in Figure 26 The results are identical.

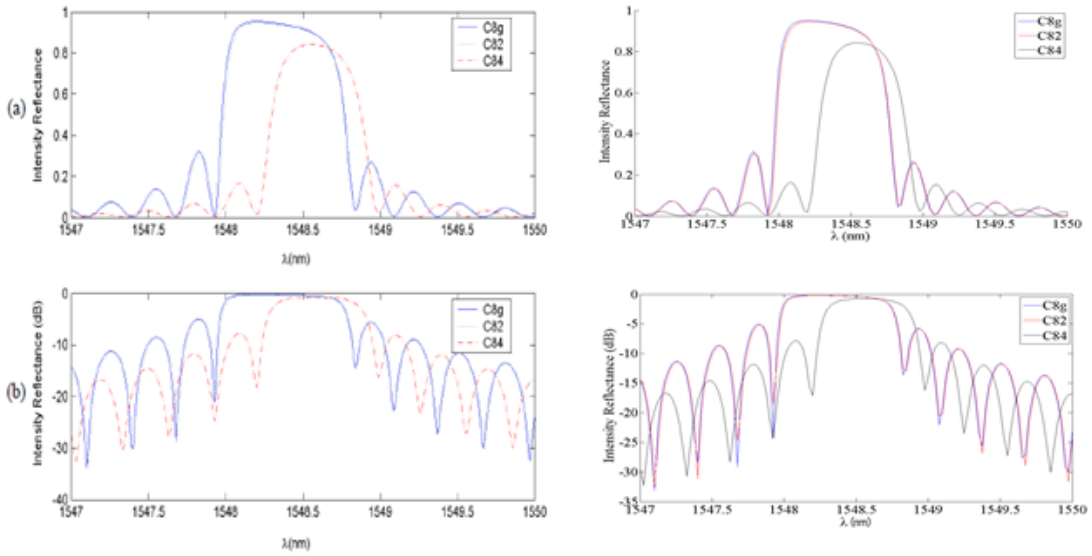

Figure 26: Reproduction of Figure 30 from reference [10]. Reflectance spectra of uniform periodic PPBGs. Three fundamental cells are used C8g, C82, and C84 for a 20 nm thick Au film embedded in SiO_2 at free space e wavelength of 1550 nm. All the gratings modeled have 35% duty cycle, pitch 0.536 μm and the total length of 2.68 nm. (a) Shows the reflectance on a linear scale, (b) shows the reflectance on a dB scale. The first column is from [10], and the second column is the reproduction.

3.4.1.3 Design Methodology

The modeling starts by numerically solving a boundary-value problem based on Maxwell's equations, in order to obtain the dispersion characteristics of waveguides sections that comprised the gratings at a specific wavelength. These calculations are done for the waveguides of different physical characteristics. The normalized phase and attenuation constants are then used to define the equivalent thin-film stack; some specifications of the gratings such as the pitch Λ, the duty cycle *dc,* and the Bragg wavelength λ_B are used to define the spectral performance of the grating through TMM. The Bragg wavelength, the reflectance, and the bandwidth can be changed according to the design parameters, including the waveguides dimensions. See Figure 27.

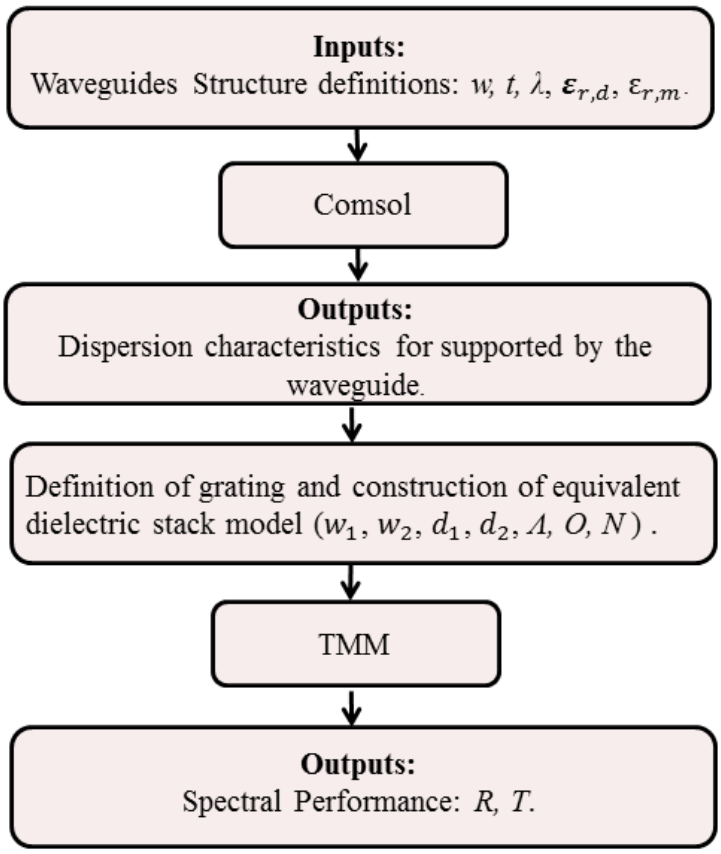

Figure 27: Plasmon-Polariton Bragg Grating Design Methodology.

3.5 Modeling Results

The computational work was handled by using an equivalent dielectric stack model, with the use of first and third order uniform periodic step in width PPBGs. All of the modeling results are based on a finite width metal waveguide made of a 35 nm thick Au film, operated at different wavelengths as shown in Chapter 2. Cytop in the upper cladding is replaced by H_2O, where the index of water is elevated to match the index of Cytop, in order to maintain the symmetry of the structure. According to these results, the effective refractive indices will differ slightly, as seen in Table 4 and Figure 28. While modeling the gratings, both real and imaginary parts of the effective refractive indices should be considered, even

though the imaginary part is smaller than the real part by approximately10^{-4}. This is because the imaginary part participates in the perturbation and the grating loss should be considered. Several fundamental cells have been considered. In each grating family, a combination of two wave guides is used; one of them w_1 is the waveguide that supports the ss_b^0 mode with the highest value of the effective refractive index, and the designs are varied by increasing w_2 in uniform steps. In general, the dimensions of the fundamental cell should be selected carefully to ensure that constructive reflections exist at the desired operating wavelength.

As mentioned previously, the designs are for uniform periodic PPBGs with rectangular profiles. Two different grating orders have been considered, the duty cycle is 50%, and the number of cells is taken to achieve approximately 90 to 95% of the total reflectance. The pitch Λ is fixed for each operating wavelength, which results in varying the Bragg wavelengths for different designs. The pitch is taken to be divisible by 5 for fabrication restrictions. Table 5 summarizes the modeling results and the spectral characteristics of the grating design at a free space wavelength of 850 nm.

Table 4: Dispersion characteristics of finite width metal waveguide comprised of 35 nm thick Au film imbedded in matched index claddings, Cytop as the lower cladding and H_2O as the upper cladding, at different wavelengths.

Wavelength (nm)	**Waveguide width** (μm)	**Effective refractive index**
850	0.5	$1.338463 - i\ 4.257276 \times 10^{-5}$
	0.75	$1.339971 - i\ 1.35223 \times 10^{-4}$
	1	$1.341915 - i\ 2.177359 \times 10^{-4}$
	1.25	$1.34375 - i\ 2.77188 \times 10^{-4}$
	1.5	$1.345313 - i\ 3.181929 \times 10^{-4}$
	1.75	$1.346598 - i\ 3.46626 \times 10^{-4}$
	2	$1.347645 - i\ 3.667119 \times 10^{-4}$
1310	2	$1.335525 - i\ 6.976001 \times 10^{-5}$
	3	$1.336695 - i\ 1.210939 \times 10^{-4}$
	4	$1.337658 - i\ 1.511915 \times 10^{-4}$
	5	$1.338363 - i\ 1.68238 \times 10^{-4}$
1550	2	$1.333525 - i\ 1.119925e \times 10^{-4}$
	3	$1.334004 - i1.246607 \times 10^{-4}$
	4	$1.334582 - i\ 1.471503 \times 10^{-4}$
	5	$1.335097 - i\ 1.6562267 \times 10^{-4}$
	6	$1.335517 - i\ 1.780266 \times 10^{-4}$
	7	$1.335852 - i\ 1.864224 \times 10^{-4}$
	8	$1.33612 - i\ 1.922478 \times 10^{-4}$

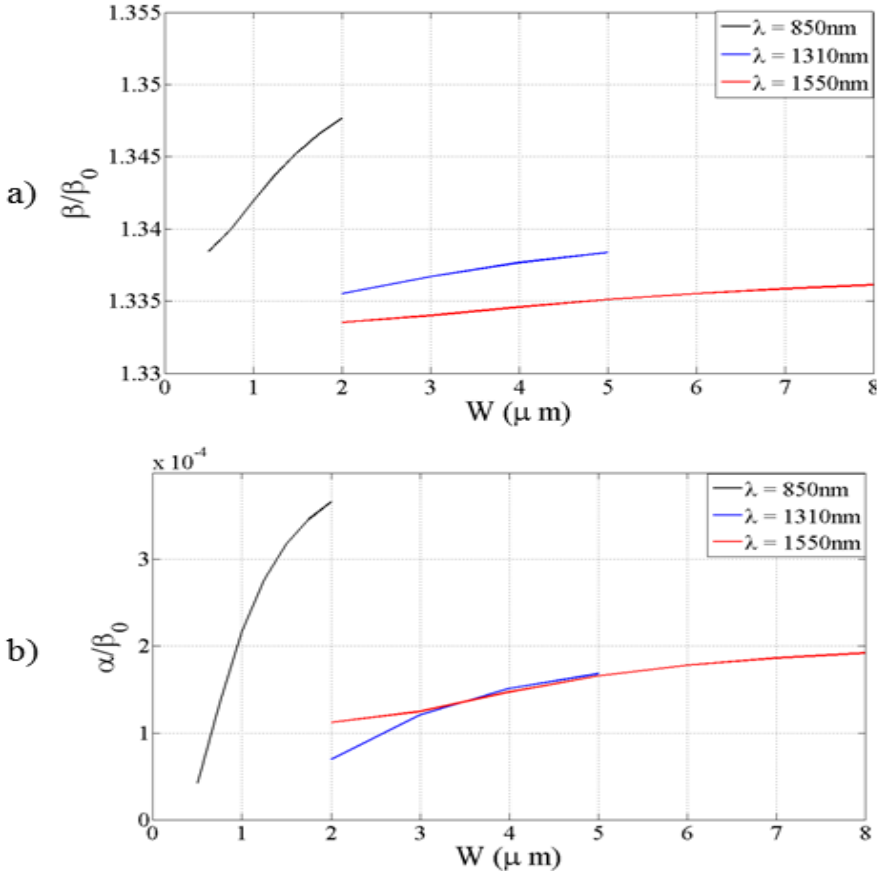

Figure 28: Effective refractive indices of the ss_b^0 mode supported by 35 nm Au film at different wavelengths. (a) is the real part while (b) is the imaginary part.

Table 5: Summary of design parameters and spectral characteristics of third order uniform periodic PPBGs, comprised of a 35nm thick Au film. The pitch is fixed at 950 nm and the duty cycle is 50% at a free space wavelength of 850 nm.

Cell design	**Reflectance**	λ_B (nm)	**N**	**L** (mm)	**FWHM** (nm)	$\lvert\Delta T\rvert$ (dB)
C2, 0.5	0.6	850.6	300	0.3	1.8	9.9
C2,0.75	0.5	851.1	300	0.3	1.4	7.3
C2,1	0.4	851.7	400	0.4	1	6.4
C2,1.25	0.2	852.3	500	0.5	0.8	4.3
C2,1.5	0.1	852.8	600	0.6	0.6	2.1
C2,1.75	0.02	853.2	600	0.6	0.55	0.46

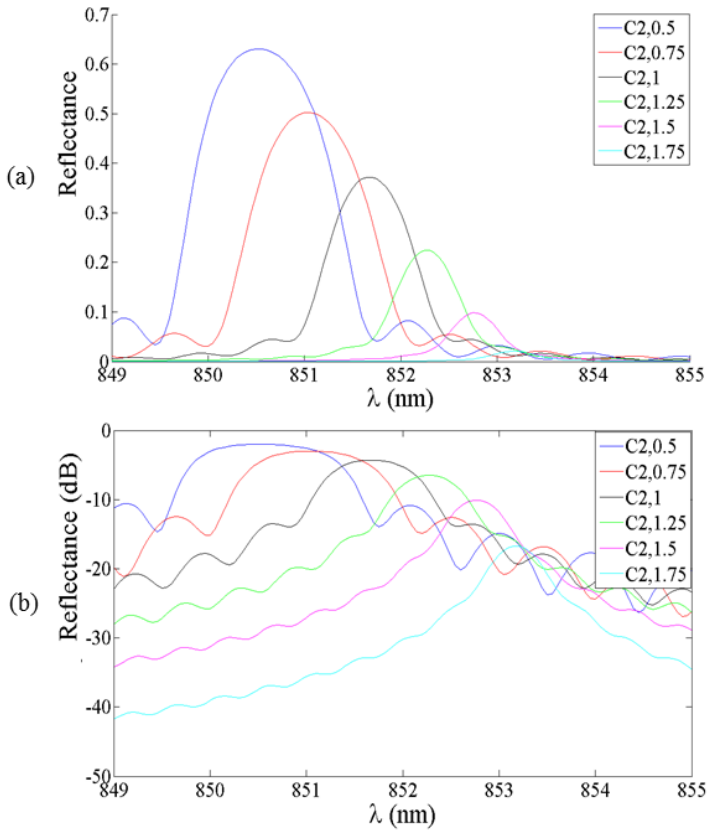

Figure 29: Modeled reflectance spectra for step in width third order uniform periodic PPBGs at a free space wavelength of 850nm and the cells are comprised of 35 nm thick Au films. (a) Shows the reflectance on a linear scale, (b) shows the reflectance on a linear scale, (b) shows the reflectance on a dB scale.

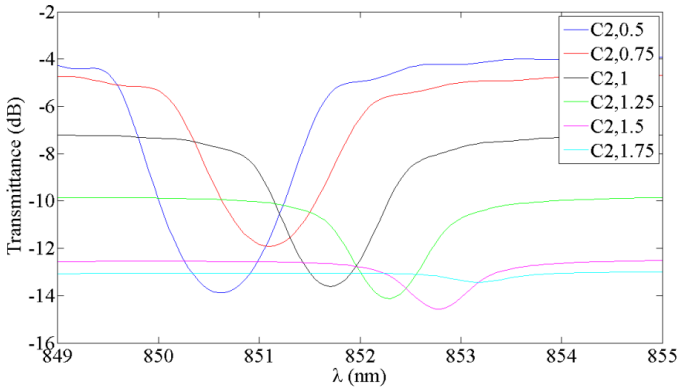

Figure 30: Modeled transmittance spectrum on a logarithmic scale for third order uniform periodic PPBGs at a free space wavelength of 850 nm and the cells are comprised of 35 nm thick Au films.

It is noted from Table 5 and Figures 29 and 30, that as the PPBGs get weaker (increasing w_2), the reflectance decreases, the Bragg wavelength shifts toward the longer wavelength side, less cells are required to achieve the desired reflectance, meaning shorter grating structures, FWHM is narrower, which agrees with equation (3.22), and the depth of the transmittance dip, which is given by the difference between the on- and off-resonance transmittance, decreases. For both FWHM and ΔT, changing the number of cells can change their values, *e.g.* when increasing the grating length, the FWHM decreases and ΔT increases. The narrower the FWHM, the easier it is to track the signal. For the transmittance, the depth of the transmittance dip should be measurable [59]. The choice of the best cell design depends on the application.

With the same waveguide thickness, PPBGs were modeled at different free space wavelengths. Table 6 summarizes the grating parameters and the spectral characteristics for the gratings at a wavelength of 1310 nm and Table 7 summarizes the grating parameters and the spectral characteristics for the gratings at a wavelength of 1550 nm.

Table 6: Summary of design parameters and spectral characteristics for third order uniform periodic PPBGs, comprised of a 35 nm thick Au film. The pitch is fixed at 1470 nm and the duty cycle is 50% at a free space wavelength of 1310 nm.

Cell design	**Reflectance**	$\boldsymbol{\lambda_B}$ (nm)	**N**	**L** (mm)	**FWHM** (nm)	$\lvert\Delta T\rvert$ (dB)
C52	0.43	1310.2	800	1.2	0.8	6.8
C53	0.2	1310.8	1000	1.5	0.6	3.4
C54	0.047	1311.3	1400	2.1	0.4	1

Table 7: Summary of design parameters and spectral characteristics for third order uniform periodic PPBGs, comprised of a 35 nm thick Au film. The pitch is fixed at 1740 nm and the duty cycle is 50% at a free space wavelength of 1550 nm.

Cell design	Reflectance	λ_B (nm)	N	L (mm)	FWHM (nm)	$\lvert\Delta T\rvert$ (dB)
C82	0.32	1548.4	800	1.4	0.9	5.4
C83	0.26	1548.7	1000	1.74	0.72	5.1
C84	0.15	1549.01	1000	1.74	0.64	2.7
C85	0.072	1549.3	1100	2	0.57	1.4
C86	0.026	1549.5	1100	2	0.54	0.5
C87	0.005	1549.7	1200	2.1	0.46	0.13

From Tables 6 and 7, it is noted that the same trends observed in PPBGs at a wavelength of 850 nm are observed at wavelengths of 1310 and 1550 nm. The main differences between the designs at various wavelengths are the strength of the grating and the depth of the transmittance dip. To compare the performance of PPBGs operated at different wavelengths, we consider the maximum reflectance that can be achieved with the strongest design in each grating family: at λ = 850 nm, $R_{max.}$= 0.6646, at λ = 1310 nm, $R_{max.}$= 0.6223, and λ = 1550 nm, $R_{max.}$= 0.3485. The highest reflectance can be achieved with designs at shorter wavelengths. In the case of a fixed reflectance at the three wavelengths, designs of 850 nm require fewer cells than designs at other wavelengths to attain the certain reflectance. However, grating designs at λ = 850 nm require a small pitch Λ, which is considered more challenging.

PPBGs have also been designed as first order gratings. The grating order is related to the Bragg wavelength via equation (3.11), and to the bandwidth of the reflected wave via equation (3.21). From the equation (3.12), for gratings with the same Δn_{eff} and n_{ave}, the bandwidth will drop for higher order gratings where the Bragg wavelength does not change, see Table 8.

Table 8: Summary of design parameters and spectral characteristics for first order uniform periodic PPBGs, comprised of a 35 nm thick Au film. The pitch is fixed at 490 nm and the duty cycle is 50% at a free space wavelength of 1310 nm.

Cell design	**Reflectance**	$\boldsymbol{\lambda_B}$ (nm)	**N**	**L** (mm)	**FWHM** (nm)	$\lvert\Delta T\rvert$ (dB)
C52	0.74	1310.2	1000	0.5	2.1	11
C53	0.56	1310.8	1600	0.78	1.3	9.1
C54	0.24	1311.3	2600	1.3	0.7	4.1

By comparing the PPBGs with different orders and the same fundamental cell designs at the same free space wavelength, it is noted that the first order gratings are stronger and produce greater reflection. The lengths of the structures are shorter, the pitch Λ is much smaller, the sidelobe levels are higher, the out of band transmission is lower since the grating is shorter, and the FWHM is wider. Thus, the grating dimension increases with the grating order. However, changing the grating order did not affect the Bragg wavelength. As mentioned previously, the design parameters are chosen according to the intended application. In this thesis work, the PPBGs are used in biosensing, justifying our focus on the Bragg wavelength and the FWHM, and not the reflection. Since the gratings with a higher order express a smaller FWHM, these designs will be the core of the study.

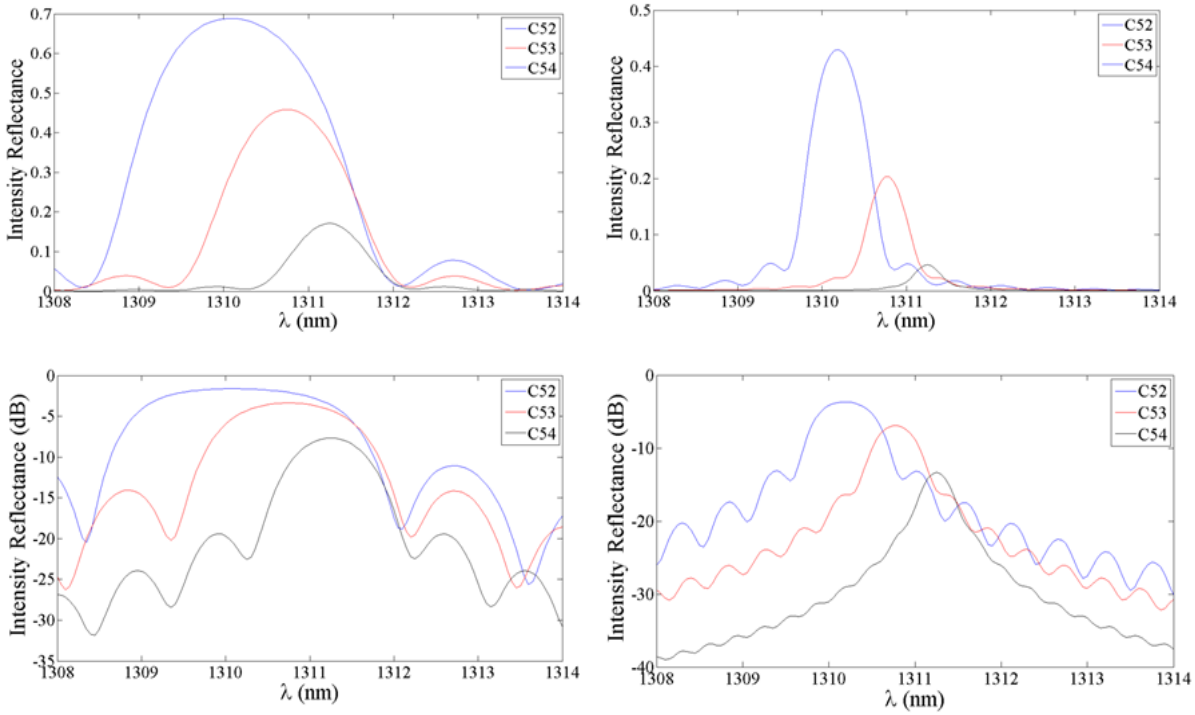

Figure 32: Reflectance spectra for PPBGs operated at a wavelength of 1310 nm and same cell designs are used with different grating orders. (a) shows the reflectance on a linear scale, and (b) shows the reflectance on a dB scale. The first column is for the gratings with the first order, while the second column is for the gratings with the third order.

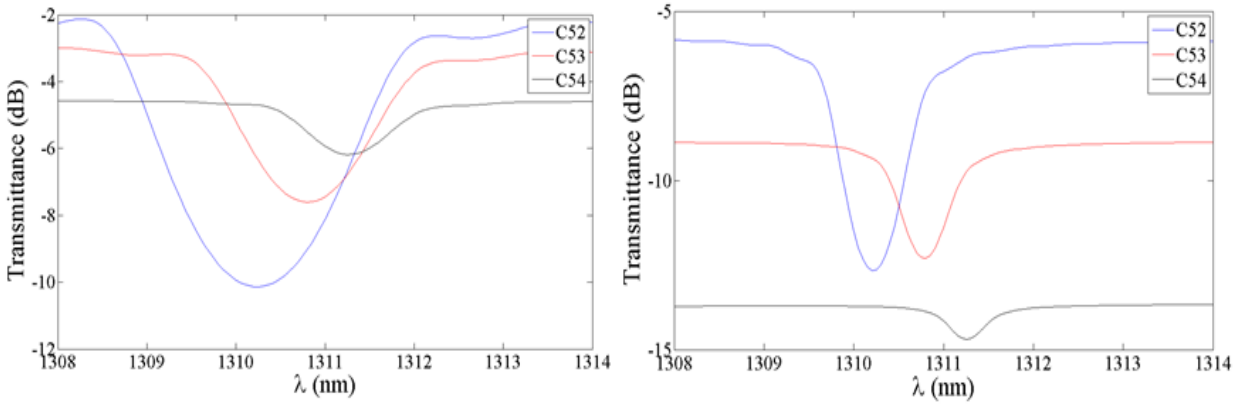

Figure 31: Transmittance spectra for uniform periodic PPBGs operated at 1310nm with the same fundamental cell design. The first graph is for the gratings with the first order and the second for the gratings with the third order

From Figure 31, it is noted that in the reflectance spectra there is a skew in the maximum reflectance peak. It is more obvious as the peak reflectance increases, and it is due to the loss in the grating. Short and long wavelengths, on either side of λ_B, will penetrate the grating for varying distances before being reflected; each wavelength therefore experiences a different amount of loss, introducing the skew in the spectra [59].

3.6 Effect of the Access Waveguides

In order to obtain the spectral response of the PPBGs, the reflected and the transmitted optical signals should be collected at the input and the output. This can be done by using access wave guides. The access waveguides are waveguides that are attached to the grating structures at the input and the output. They are identical in dimensions, their total length equals the difference between the gratings length and the die length, and their widths are identical to the width of the waveguide section that supports the ss_b^0 mode with the highest effective refractive index of the fundamental cell of the gratings (extending from the input and the output of the gratings) [34]. The spectral response (insertion loss) of these waveguides has been disregarded in this study, where the access waveguides will increase the loss of the gratings [10, 34]. In addition, access waveguides are used to excite the grating by coupling with fiber using an end fire coupling technique [35].

3.7 Summary

PPBGs in this study are constructed by creating a pattern with the width of LRSPP waveguides comprised of 35 nm thick Au film in a H_2O/Cytop background, and supporting a single long ranging mode ss_b^0 along the direction of propagation. If light is launched at the input of the grating, incident wave will undergo perturbations at each interface, forming micro-reflections that add constructively to form a reflected wave that travels along the

structure to the input of the grating. The remainder of the light launched appears at the output as the transmitted wave. In this chapter, the performance of uniform periodic step in width PPBGs was investigated theoretically. The study includes the performance of the gratings at several wavelengths and different grating orders. PPBGs exhibit very interesting spectral properties; changing the grating parameters can modify the spectral response.

Chapter 4 PPBGs Biosensing Performance

In this chapter, the sensitivity of PPBGs is examined theoretically. The sensing performance of several designs at different wavelengths is obtained in terms of both bulk and surface sensitivities. The sensitivities were calculated for the LRSPP waveguides that comprise the gratings, as well as for PPBGs as whole devices. The detection limit was also theoretically estimated for both bulk and surface sensitivities.

4.1 Design Considerations

The structure of PPBGs was demonstrated in the previous chapter. The grating is placed in Cytop and its upper surface is exposed to the sensing fluid through an etched channel in the upper cladding. The ends of the gratings are connected to access waveguides, as in Figure 33. The performance of any device can be determined by several factors such as the materials used to fabricate the device, the structure (*e.g.* symmetric), and the dimensions. To optimize the performance of PPBGs, a good selection of the materials and dimensions should be considered.

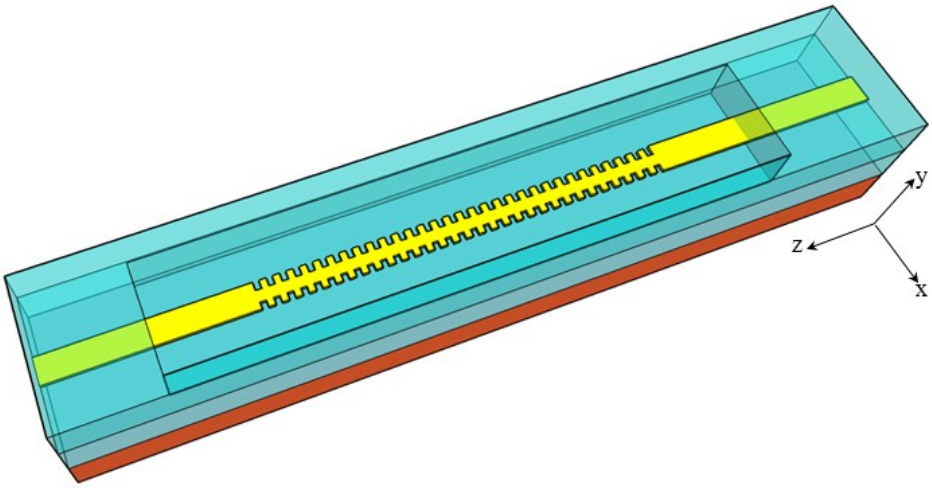

Figure 33: PPBGs used for biosensing, the gratings is based on Cytop and exposed from the upper side to the sensing fluid.

4.1.1 Materials

It is essential to select proper materials in order to optimize the performance of PPBGs. In this study, the materials selected were the following: gold for the metal stripes, Cytop for the lower cladding, and water for the upper cladding.

4.1.1.1 Gold

The properties of Gold (Au) make it a metal of choice in almost all bio-sensing applications. It is a suitable choice for biosensing because of its stability under chemical reactions when comparing it to other candidate metals such as Silver (Ag) [23].

Gold and silver are suitable metals for plasmonics; gold exhibits chemical inertness, whereas for silver, attempts have been made to protect the thin, non-inert silver layer [69]. Silver Ag has reactive nature; it reacts with sulfur in air or fluid and can cause cell toxicity [15]. The performance of biosensors involving silver decreases rapidly to non-practical level [69].

Using an Au stripe as the core of the waveguide is advantageous because of the nature of this metal; it is easy to be obtained as a thin film by vapour deposition, it is easy to be patterned by a combination of lithographic techniques, it is relatively inert, where it does not oxidize below its melting temperature and does not react with most chemical compounds. Thin gold films are commonly used as substrates for many spectroscopy techniques such as surface plasmon resonance (SPR), quartz crystal microbalances (QCM), Raman infrared spectroscopy (RAIRS) and ellipsometry. Gold is also biocompatible with cells, allowing them to adhere to its surface and function properly without evidence of toxicity [15]. Gold is the most studied metal in this field [6]. Furthermore, a thin gold film with low surface roughness can bind to SAM (self-assembled monolayer) easily, and sustains stable bonds for days and even weeks when exposed to complex media [15]. In addition, it does not require an adhesion layer to stick to Cytop; this is beneficial since adhesion promoting layers are strongly absorbing [15].

For all these reasons, gold is the selected metal in almost all practical plasmonic sensing applications. As a result, sensing is usually limited to the red part of the visible spectrum and the near-infrared, due to the permittivity of gold [12]. Gold is strongly absorbent for blue and green, due to interband transition in the Drude model.

4.1.1.2 Water

The choice of water for the upper cladding is because in most biosensing devices the carrier fluid for the analyte is an aqueous solution [5].

4.1.1.3 Cytop

Many biosensing devices must perform with an aqueous solution, and Cytop features a refractive index that is close to that of water, which makes it an ideal material to construct many biosensing devices.

The device of interest is operated by supporting the long ranging ss_b^0 mode. It was mentioned previously that even though the long ranging mode is less sensitive than the single interface, its low attenuation makes it more practical in biosensing applications and higher performing because optical interaction lengths are longer. In order to lower the attenuation for the ss_b^0 mode supported by LRSPP waveguides to its lowest value, the refractive index around the metal should be homogenous. Therefore, to support ss_b^0 mode in bio-sensing applications, a cladding with a refractive index that matches that of the fluids is used to carry the analyte, which is mostly aqueous with an index of approximately n≈ 1.33, meaning that low index claddings are required [6]. Using low index claddings is beneficial so that the fluidic channels become less invasive when filled with sensing solution [6].

The choice of the polymer to be used beneath the metal film should consider the refractive index, since index matching claddings are the key to obtaining a symmetric mode. Water is used for the upper cladding since most sensing fluids are aqueous and its refractive index is important to determine the polymer that forms the lower cladding. The polymer of choice should have a refractive index that is close to that of water. Most polymers possess refractive indices that are higher than the refractive index of water. The most common materials used for this purpose are Cytop and Teflon; they have both been used as claddings in sensing experiments involving slabs that support LRSPP modes [6], but Cytop which is a fluoropolymer with a refractive index of 1.3348 at 1300 nm wavelength, is close to the refractive index of the de-ionized water [15].

Cytop is very suitable for the construction of devices used for biosensing applications. Besides satisfying the essential requirement of index matching, there are other properties

that make this polymer a good choice for many biosensing devices: it is impervious to water, oil and some other chemicals, and it features good transparency. In fabrication, it can be easily applied over a silicon wafer without the need of an adhesion layer by spin coating and dip coating [15].

In biosensing experiments carried out for different devices [15, 6], both claddings are Cytop, where the upper cladding is etched with a microfluidic channel to provide access to the sensing surface (metal stripe), or removed for that same purpose. In this study we based all the calculations on the sensing fluid as the upper cladding, since it is index matched with the polymer used in the lower cladding.

4.1.2 Dimensions

The dimensions of the metal stripe should be selected properly to support only the fundamental symmetric mode. Good dimensions for the gold stripe are 20 ~ 35 nm thick and 5μm wide, since t = 35nm have been tested in several studies and gave good results, it was the thickness of choice. For the claddings it is known that in order for the ss_b^0 mode to have its full expansion, the claddings should be sufficiently thick and from [15] it was found that the thickness of the Cytop should be at least 8μm. This is taken as the thickness of the bottom cladding (Cytop). The upper cladding was taken as optically semi-infinite in thickness since it represents the sensing solution. It was considered that all the modes should be nicely bounded. In order to maintain that, the widths that did not support good bounded modes were excluded such as w =1μm at a wavelength of 1310 and 1550 nm.

4.1.3 Structure

Using a symmetric structure increases the propagation length of the supported mode beyond that of the SPP and preserves the energy of the incident beam [70]; this enhances sensitivity.

In order to achieve optimal sensitivity for the device, the attenuation constant should be reduced. This can be done by insuring that both claddings are index matched as was explained in a previous section. Index matched claddings can provide a perfectly symmetric ss_b^0 mode. Moreover, the material composing the claddings should possess a refractive index that can match the refractive index of the bio-sensing fluid. A mismatch in the refractive index of the upper and lower claddings would result in an asymmetric device, which would

reduce its sensitivity [71]. Nonetheless, in certain situations, the symmetric mode can still be supported by an asymmetric structure. For biosensing applications, there is another way to create environment that support ss_b^0 without using index-matched materials. This can be achieved by using a thin high-index layer that, with the sensing fluid, can create an effective index that closely matches the index of the material used in the other cladding. Even though this structure is not physically symmetric, it is symmetric in terms of the index [72]. This type of structure has previously been used for biosensing [73].

4.2 Sensitivity

The sensitivity of biosensors means the ability to detect, capture and recognize analyte present in the sensing fluid [2]. The sensing procedure relies on the change in the refractive index caused by the presence of analytes in the sensing solution, or the adsorption of the target analyte on the sensing surface. The interaction of the target analyte on the sensing surface or in the sensing solution results in small variations in the biosensors' optical properties, such as the refractive index. The variations are used to express measurable signal variations [70]. For PPBGs, the change in the effective refractive index is translated into a shift in the Bragg wavelength λ_B.

The sensitivity can be defined as the ratio of the measured optical parameter to the change in the waveguide parameter influenced by analytes [74].

In waveguide based sensors, the sensitivity is determined for two cases: surface and bulk sensing [74]. In bulk sensing, the analytes exist in the aqueous solution that surround the device in the upper cladding only. The bulk refractive index of the sensing solution will change due to the presence of the analyte. This variation in the index influences the effective refractive index of the guided mode. In bulk sensing, all materials existing in the sensing solution participate in the change of the refractive index, including the target analyte. To overcome this generality, surface sensing is required. In surface sensitivity, the metal surface is treated and functionalized to have receptors for the target analyte only [74].

To determine the potential of PPBGs in biosensing, the sensitivity has to be investigated for several designs where it is defined by a shift in Bragg wavelength relative to the change in the adlayer thickness for the case of surface sensing, and also by a shift in Bragg wavelength relative to the change in bulk refractive index for the case of bulk sensing.

4.2.1 Waveguides Sensitivities

4.2.1.1 Surface Sensitivity

The sensitivity calculations for this study followed the method presented in [5]. In [5], Berini studied the sensitivities for different 1D structures supporting surface plasmon polaritons. Since 1D and 2D waveguides share the same essential features, the study conducted in [5] for bulk and surface sensitivities of surface plasmon waveguides can be used to investigate the sensitivity of PPBGs.

There are several ways to define surface sensitivity [71, 70]. In this thesis work, the definition is adopted from [5], which is $\delta n_{eff}/\delta a$, where a is the adlayer thickness, as shown in Figure 34. This method for calculating the surface sensitivity was used to calculate the sensitivity in different structures including single interface, metal/insulator/metal, and insulator/metal/insulator.

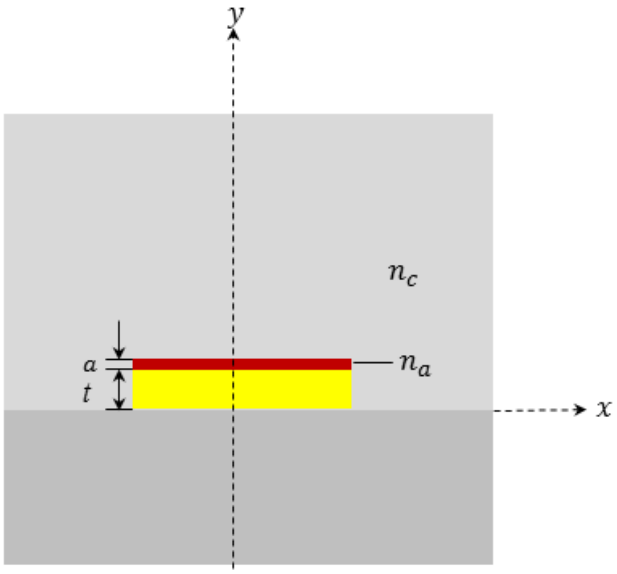

Figure 34: Sketch of surface plasmon waveguide in surface sensing, the metal surface is covered with an adlayer of thickness a and $\boldsymbol{n_a}$ as refractive index.

Surface sensitivity has two parts. Real and imaginary represent the effective index surface sensitivity and the normalized attenuation surface sensitivity, respectively. The surface sensitivity is defined by the following equation:

$$\frac{\delta n_{eff}}{\delta a} = \frac{n_{eff}(a+h_a) - n_{eff}(a-h_a)}{2h_a} \tag{4.1}$$

where h_a is the change in the adlayer thickness. The nominal adlayer thickness is taken 3 nm to represent a monolayer of receptor molecules [5], and $h_a = \pm 0.1$nm.

The surface sensitivity is carried out by introducing an adlayer to the waveguides. The adlayer is located along the top surface of the Au stripes and presented as a homogenous region, parallel to the metal stripe, and longitudinally invariant [5]. The adlayer is characterized by optical parameters equivalent to the biochemical adlayer a and n_a, where n_a is the refractive index ($n_a = 1.5$) and is constant with wavelength [5] The index and thickness of the adlayer located on the sensing surface have a great impact in supporting the mode of interest [69]. The sensitivity for the device is determined by investigating the effect of the adlayer.

The surface sensitivity of the waveguides (sensing surface) is where the biomolecular interaction takes place and even though it is small in dimension, it affects and determines the performance of the biosensor and the quality of the measured data [75]. Consequently, the metal surface has to be functionalized to optimize the sensing procedure and to ensure the selectivity of the molecules of interest [12, 76]. The binding of the molecules to the surface results in a change of the effective refractive index of the ss_b^0 mode; this change can be measured optically to indicate the presence of analyte [15].

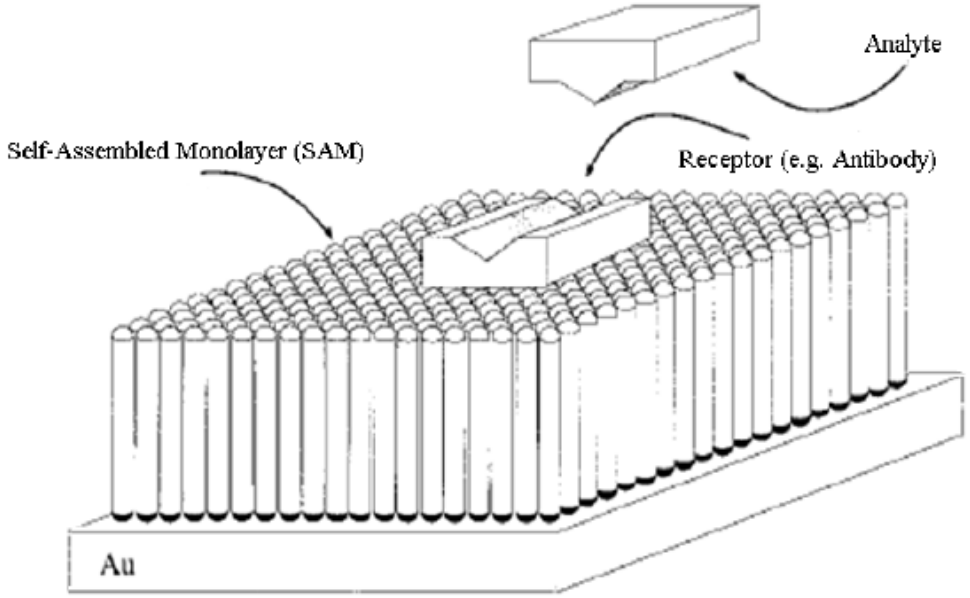

Figure 35: Functionalization of gold surface for surface sensing applications. "Reprinted with permission from [76].Copyright 1993, AIP publishing LLC."

Functionalizing the gold surface to the target analyte allows only the target analyte to bind to the surface of the gold. This can be done by covering the sensing with a self-assembled monolayer (SAM). SAM binds to the metal surface and is functionalized with a certain receptor, which depends on the targeted analyte, for example antibodies for protein detection [15]. The biomolecular interactions produce a variation in the thickness of the adlayer, as well as in the refractive index, which affect the resonance conditions. The degree of change in the adlayer and in the refractive index or thickness is meaningful as it represents specific characteristics of the target analyte [23]. As the mode propagates along the metal surface, it will be affected by the change occurring at the surface due to the accumulation of analytes. This will lead to a change in the effective refractive index of the supported mode; this change indicates the interaction between the analyte (molecules) and the surface, and can be measured depending on the device (*e.g.* change in the resonant angle of the incident light, change in the intensity of the reflected light) [77].

For this thesis work, the surface sensitivity study started by reproducing the surface sensitivity results obtained in [5] for insulator/metal/insulator, where the metal surface was covered with an adlayer of nominal thickness of 3nm. The thickness was then changed with

$h_a = \pm$ 0.1nm. The surface sensitivity was calculated following equation (4.2), and the results were in good agreement.

4.2.1.1.1 Modeling Results

The surface sensitivity of the waveguides presented in this study is conducted using the same waveguides as presented in chapter 3. An adlayer of thickness 3 nm is introduced to the waveguides, with changing thickness $h_a = \pm 0.1$ nm.

First, an adlayer of thickness 3 nm and $n_a = 1.5$ is introduced to the waveguides. The presence of this adlayer affects the ss_b^0 mode as it increases the phase constant of the mode, Figure 36, then the adlayer thickness is changed by $h_a = \pm 0.1$ nm to calculate the surface sensitivity; see Figure 37.

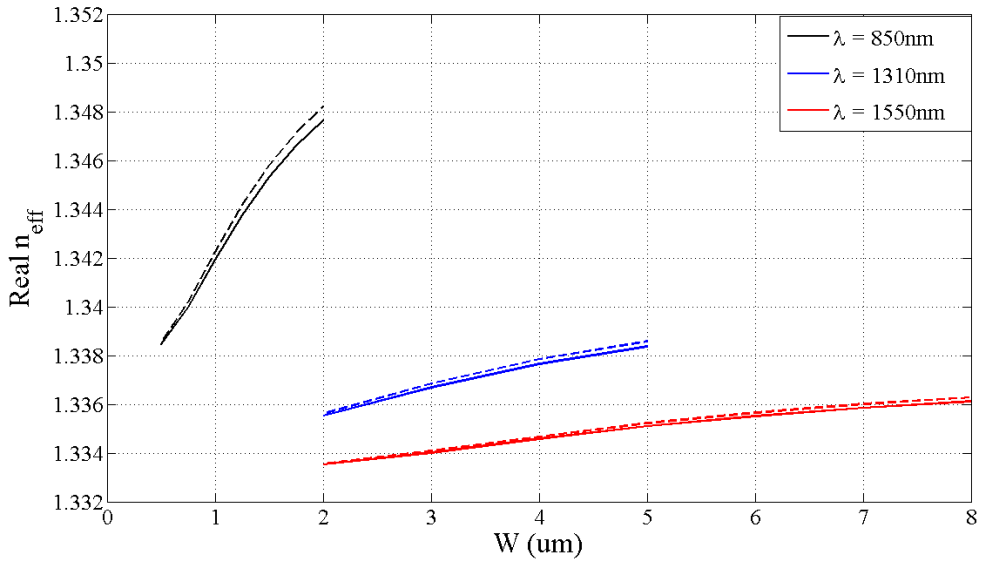

Figure 36: Change in the effective refractive index of the ss_b^0 mode supported by finite widths waveguides affected by the presence of an adlayer of 3 nm thickness and n_a=1.5. The dotted lines represent the normalized propagation constant of the ss_b^0 mode with the adlayer where the solid lines represent the normalized phase constant without the adlayer at different wavelengths.

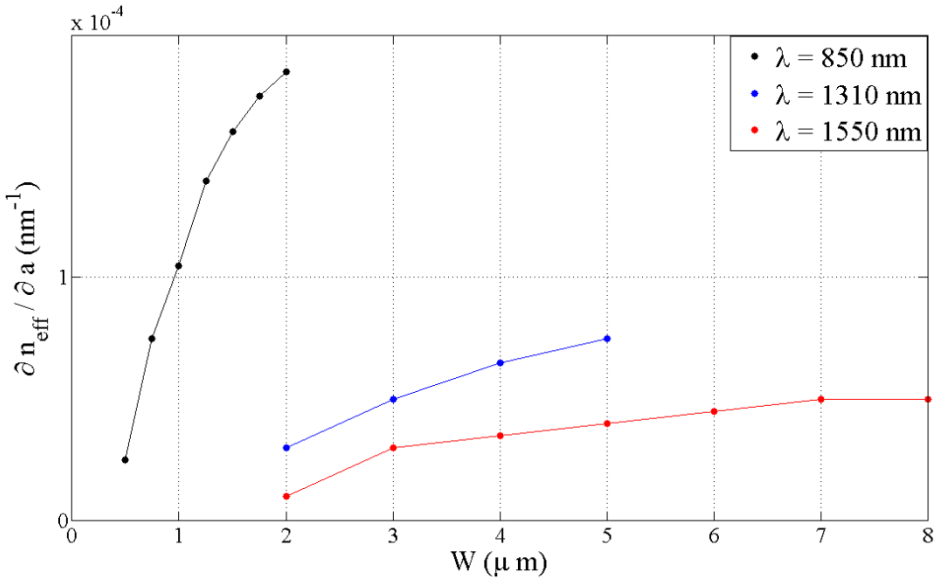

Figure 37: Surface sensitivity as a function of width for finite width metal film supporting ss_b^0 mode.

It is clear from the graph that the surface sensitivity increases when decreasing the wavelength, giving best results at λ = 850 nm. This agrees with [5], where the sensitivity also increases with the width as it is associated with the confinement. The mode becomes more bounded to the metal film with an increasing width and decreasing wavelength, and becomes more sensitive to changes occurring on the sensing surface.

4.2.1.2 Bulk Sensitivity

The bulk sensitivity is calculated without an adlayer on the metal film and defined as $\delta n_{eff}/\delta n_c$ [5]. It is handled by inducing a homogenous change in the refractive index of the sensing fluid. The bulk sensitivity has real and imaginary parts related to the effective index: phase bulk sensitivity and attenuation bulk sensitivity, respectively [5]. The bulk sensitivity is defined by the following equation:

$$\frac{\delta n_{eff}}{\delta n_c} = \frac{n_{eff}(n_c+h_c-jk_c)-n_{eff}(n_c-h_c-jk_c)}{2h_c} \tag{4.2}$$

where h_c represents the change in the bulk index, n_c is the index of the sensing solution, and k_c is neglected. The accuracy increases as $h_c \to 0$. Changing the bulk refractive index introduces a perturbation in the permittivity distribution of the structure; this perturbation

will change the propagation constant of the supported mode. The sensitivity of the structure can be determined from the difference in the phase constant.

The bulk sensitivity for biosensors is determined from the response of the sensor for different sensing fluids; these sensing fluids have different refractive indices [15, 5, 6, 7].

The change in the refractive index according to h_c should meet the requirements of supporting ss_b^0 mode. Different values for h_c were used to induce a suitable change in the refractive index. In experiments, the index of the sensing solution can be increased by adding materials (*e.g.* glycerol) to the stock buffer solution, or decreased by diluting it with water [15].

4.2.1.2.1 Modeling Results

As mentioned previously, various values for h_c have been tested, it was found that a suitable value is (5×10^{-4}). This change in the refractive index of the sensing solution can maintain the symmetry of the mode, with no radiation, and provide a compatible shift for the values found in the surface sensitivity. See Figure 38.

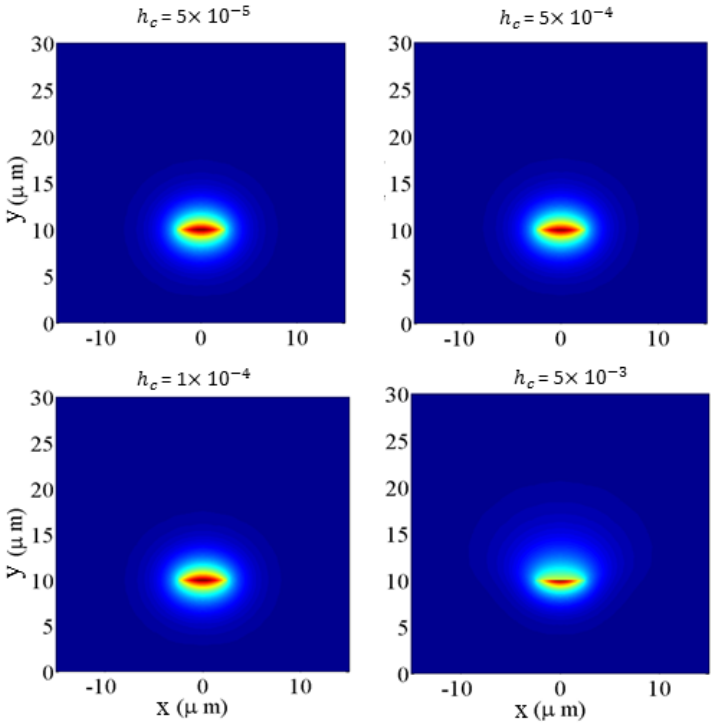

Figure 38: Series of field distribution for the ss_b^0 mode supported by a metal stripe of 35 nm thickness and 5 μwidth at free space wavelength of 1310nm, obtained by using series of solutions with different refractive indices.

Applying equation (4.1), the waveguides' bulk sensitivities are computed, as presented in Table 9.

Table 9: Bulk sensitivity for LRSPPs waveguides ($\frac{\delta n_{eff}}{\delta n_c}$) as a function of width at free space wavelength of 850, 1310, and 1550 nm.

Wavelength (λ) (nm)	**Width (W) (nm)**	$\frac{\delta n_{eff}}{\delta n_c}$
850	0.5	0.493
	0.75	0.511
	1	0.515
	1.25	0.517
	1.5	0.518
	1.75	0.518
	2	0.519
1310	2	0.525
	3	0.509
	4	0.508
	5	0.508
1550	3	0.554
	4	0.51
	5	0.51
	6	0.508
	7	0.508
	8	0.506

From the previous table it is noticed that the bulk sensitivities are about 0.5 for all waveguides. This is expected since about half of the mode area is affected by the change in the bulk index.

4.2.2 Waveguides Sensitivities with the Perturbation Method

The method mentioned above is the finite-difference approximations method; an alternative method is the perturbation method, which is considered more complicated to compute [5]. According to perturbation method, it is possible to obtain the change in the phase constant of a mode by introducing a perturbation in the permittivity distribution of the structure. In this case the perturbation is constant longitudinally [5]. The effective index sensitivity can be determined from the change in the phase constant [5]. Ignoring the losses, both the unperturbed (u) and the perturbed (p) field can be written as follows [5]:

$$\boldsymbol{E}_u(x, y, z) = \boldsymbol{E}_u(x, y)\, e^{-i\beta_u z} \tag{4.3}$$

$$\boldsymbol{H}_u(x, y, z) = \boldsymbol{H}_u(x, y)\, e^{-i\beta_u z} \tag{4.4}$$

and

$$\boldsymbol{E}_p(x, y, z) = \boldsymbol{E}_p(x, y)\, e^{-i\beta_u z} \tag{4.5}$$

$$\boldsymbol{H}_p(x, y, z) = \boldsymbol{H}_p(x, y)\, e^{-i\beta_u z}$$

The perturbed and the unperturbed permittivity distributions are related via the following equation:

$$\varepsilon_p(x, y) = \varepsilon_u(x, y) + \Delta\varepsilon\,(x, y) \tag{4.6}$$

The change in the phase constant as a result of the perturbation can be provided by the following equation:

$$\beta_p - \beta_u = \omega \frac{\iint_{A_\infty} \Delta\varepsilon\, \boldsymbol{E}_p . \boldsymbol{E}_u^*\, dA}{\iint_{A_\infty} (\boldsymbol{E}_u^* \times \boldsymbol{H}_p + \boldsymbol{E}_p \times \boldsymbol{H}_u^*)\, \hat{z}\, dA} \tag{4.7}$$

Where A_∞ is the area of the infinite transverse cross section and $\hat{z}$ is the unit vector in the z direction. The perturbed and the unperturbed fields can be considered identical if the perturbation $\Delta\varepsilon$ is small. In this case, when defining the perturbation $\Delta\varepsilon$ in terms of refractive index perturbation:

$$\Delta\varepsilon\,(x, y) = \varepsilon_0\,(n_p^2(x, y) - n_u^2\,(x, y)) \tag{4.8}$$

The change in the effective index is obtained and given by the following equation:

$$n_{eff,p} - n_{eff,u} = \sqrt{\frac{\varepsilon_0}{\mu_0}}\frac{1}{4P_{AVE}}\iint_{A_\infty}(\,n_p^2 - n_u^2)|E_u|^2\,dA \tag{4.9}$$

Where P_{AVE} is the time-averaged real power carried by the mode, and is defined as:

$$P_{AVE}=\frac{1}{2}\iint_{A_\infty} Re\,\{\boldsymbol{E}_u \times \boldsymbol{H}_u^*\}\,\hat{z}\,dA \tag{4.10}$$

When the perturbation is caused by the presence of an adlayer of index n_a and cross sectionA_∞:

$$n_p^2\,(x, y) - n_u^2\,(x, y) = \begin{cases} n_a^2 - n_c^2 & for\ x, y\ in\ A_a \\ 0 & elsewhere \end{cases} \tag{4.11}$$

and equation (4.9) can be written as:

$$\Delta n_{eff} = n_{eff,p} - n_{eff,u} = \sqrt{\frac{\varepsilon_0}{\mu_0}}\frac{(n_p^2 - n_u^2)}{4P_{AVE}}\iint_{A_a}|\boldsymbol{E}_u|^2\,dA \tag{4.12}$$

From the previous, if $n_a^2 > n_c^2$, then $\Delta n_{eff} > 0$, this is the case for biosensors. Maximizing the sensitivity is associated with maximizing the overlap of the mode fields with the adlayer area A_a, and this can be achieved by increasing Δn_{eff} which indicates increasing the overlap. Only fields within A_a are affecting the integral, regarding this, if possible, the mode area should be comparable to A_a, and the mode field peaks inside A_a [5].

For bulk sensitivity, the perturbation is caused by a change in the refractive index of the sensing solution of A_c area, the perturbation ish_c, where $h_c \ll n_c$:

$$n_p^2\,(x, y) - n_u^2\,(x, y) = \begin{cases} (n_c + h_c)^2 - n_c^2 & for\ x, y\ in\ A_c \\ 0 & elsewhere \end{cases} \tag{4.13}$$

Then a simplification of equation (4.9) can be applied:

$$n_{eff,p} - n_{eff,u} = \sqrt{\frac{\varepsilon_0}{\mu_0}}\frac{n_c\,h_c}{2P_{AVE}}\iint_{A_c}|\boldsymbol{E}_u|^2\,dA \tag{4.14}$$

4.3 PPBGs Sensitivities

4.3.1 PPBGs Surface Sensitivity

The surface sensitivity computations are carried out by introducing an adlayer to the waveguides constructing PPBGs, as in Figure 34. The sensitivity is determined for the device by investigating the effect of the adlayer.

The adlayer is located along the top surface of the Au stripes that create PPBGs, which is the sensing surface. As mentioned previously, the presence of this adlayer affects the ss_b^0 mode. Consequently, the grating properties will change including λ_B. The difference in the Bragg wavelength for a device with and without an adlayer (shift) captures the sensitivity of the device; see Figure 39.

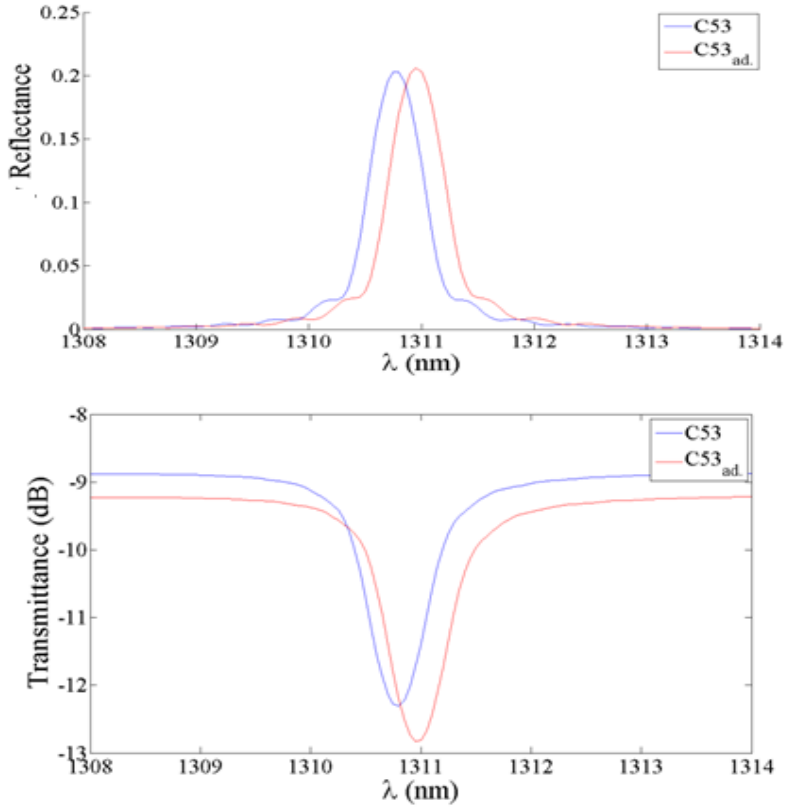

Figure 39: Comparison of the wavelength spectra for C53 design with the adlayer, operated at wavelength of 1310 nm. The red line indicates the wavelength response of the design with the presence of the adlayer.

From the previous graph, it is clear that the wavelength response changes with the presence of the adlayer. The changes are minor for reflectance and transmittance, but greater variation is caused in the position of the Bragg wavelength.

The surface sensitivity of PPBGs is computed in two different ways. First, the sensitivity is found for the whole device. The wavelength response is obtained for the grating with and without an adlayer and the shift is then found. An adlayer with a thickness of 3nm is introduced to PPBGs, then calculations were carried out in the same manner presented in chapter 3 to obtain the new Bragg wavelength λ_B. A change in the gratings characteristics is observed (*e.g.* reflectance) but our interest is in λ_B. The shift that occurred in the Bragg wavelength represents the surface sensitivity, where a larger shift means a higher sensitivity. The second way in which the sensitivity calculated is from the sensitivities calculated for the LRSPPs waveguides that construct the grating. The sensitivity calculations are carried out by introducing an adlayer with a changing thickness by h_a, the accuracy enhanced as h_a tends toward (0). Both computation methods are in agreement with each other.

For the waveguides that construct the grating, the sensitivity is computed by applying equation (4.1), as shown in a previous section of this chapter. The waveguides sensitivities are then used to determine the device sensitivity. The adlayer thickness is changed for each waveguide comprising the fundamental cell with $\pm$ 0.1 nm, and the characteristics of the ss_b^0 mode is computed as a function of the adlayer thickness. Equation (4.1) is then applied to find the surface sensitivity of each segment of the fundamental cell of the gratings. To obtain the surface sensitivity of the device, we use equation (3.11) and take the derivative with respect to a:

$$\frac{\partial \lambda_B}{\partial a} = \frac{2\Lambda}{O} \frac{\partial n_{ave}}{\partial a} \tag{4.15}$$

where

$$\frac{\partial n_{ave}}{\partial a} = \left(\frac{\partial n_{eff,w_1}}{\partial a} + \frac{\partial n_{eff,w_2}}{\partial a} \right) / 2 \tag{4.16}$$

since

$$\frac{\partial \lambda_B}{\partial a} \approx \frac{\Delta \lambda_B}{\Delta a} \tag{4.17}$$

the shift is $\Delta \lambda_B = \frac{\partial \lambda_B}{\partial a} . \Delta a$ (4.18)

where $\Delta \lambda_B$ is the obtained shift in the Bragg wavelength for an adlayer of thickness Δa = 3 nm.

4.3.1.1 Modeling Results

The shift is calculated for each grating family over the wavelengths of interest (850, 1310, and 1550 nm). The following table is a copy of Table 4 in the previous chapter, with the addition of the shift that can be achieved by each design.

Table 10: Summary of design parameter, spectral characteristics and shift for third order uniform periodic PPBGs comprised of a 35 nm thick Au film. The pitch is fixed at 1470 nm and the duty cycle is 50% at free space wavelength of 850 nm.

Cell design	**Reflectance**	λ_B (nm)	**N**	**L** (mm)	**FWHM** (nm)	|ΔT| (dB)	$\Delta\lambda_B$ (nm)
C2, 0.5	0.6	850.6	300	0.3	1.8	9.9	0.2
C2,0.75	0.5	851.1	300	0.3	1.4	7.3	0.25
C2,1	0.4	851.7	400	0.4	1	6.4	0.28
C2,1.25	0.2	852.3	500	0.5	0.8	4.3	0.31
C2,1.5	0.1	852.8	600	0.6	0.6	2.1	0.33
C2,1.75	0.02	853.2	600	0.6	0.55	0.46	0.34

The previous table shows that the shift is inversely proportional to the grating strength; this is expected since the sensitivity increases when increasing the confinement. Weaker designs are formed with waveguides that features higher loss and more confinement. See Figure 40.

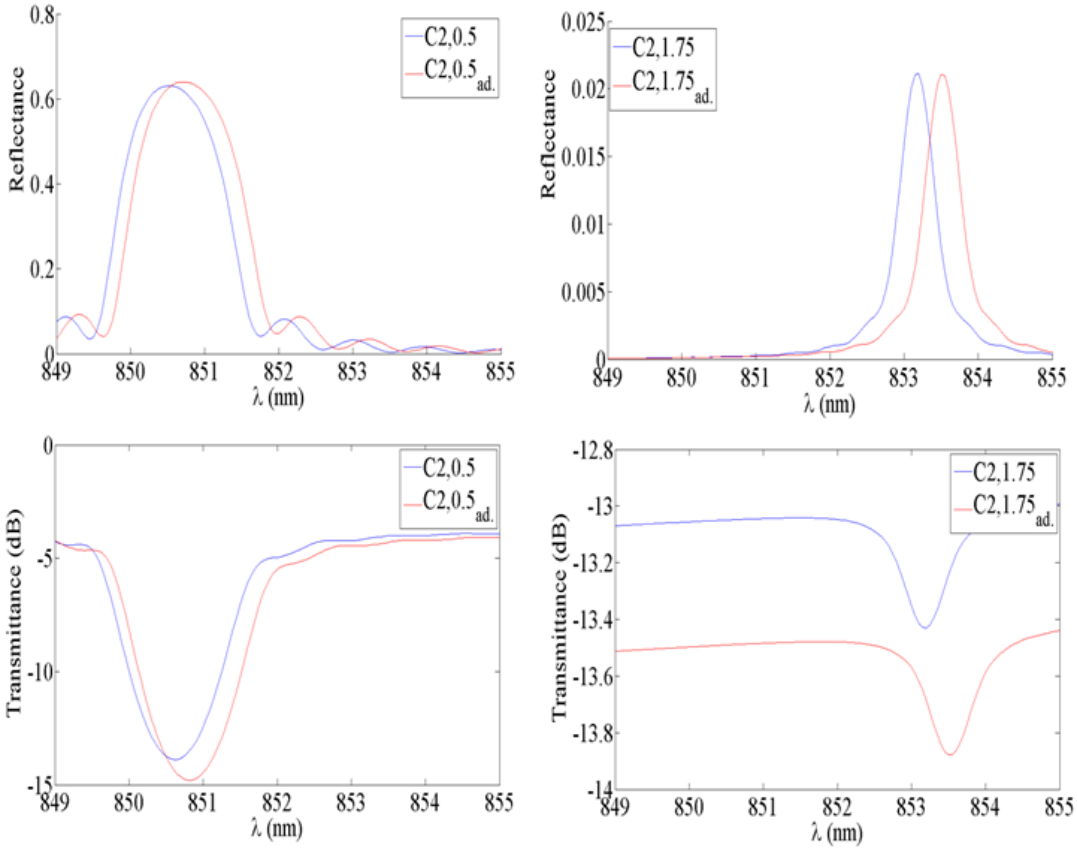

Figure 40: Wavelength spectra for C2,0.5 and C2,1.75 operated at 850 nm free space wavelength, the blue and the red curves indicate the spectra for the PPBGs without and with an adlayer respectively.

The same trend is observed with PPBGs operated at free space wavelengths of 1310 and 1550 nm, as in Table 11 and Table 12.

Table 11: Summary of design parameters, spectral characteristics and shift for third order uniform periodic PPBGs comprised of a 35nm thick Au film. The pitch is fixed at 1470 nm and the duty cycle is 50% at free space wavelength of 1310 nm.

Cell design	**Reflectance**	λ_B (nm)	**N**	**L** (mm)	**FWHM** (nm)	$\|\Delta T\|$ (dB)	$\Delta\lambda_B$ (nm)
C52	0.43	1310.2	800	1.2	0.8	6.8	0.15
C53	0.2	1310.8	1000	1.5	0.6	3.4	0.18
C54	0.047	1311.3	1400	2.1	0.4	1	0.2

Table 12: Summary of design parameters, and spectral characteristics and shift for third order uniform periodic PPBGs comprised of a 35nm thick Au film. The pitch is fixed at 1740 nm and the duty cycle is 50% at free space wavelength of 1550 nm.

Cell design	**Reflectance**	λ_B (nm)	**N**	**L** (mm)	**FWHM** (nm)	$\|\Delta T\|$ (dB)	$\Delta\lambda_B$ (nm)
C82	0.32	1548.4	800	1.4	0.9	5.4	0.102
C83	0.26	1548.7	1000	1.74	0.72	5.1	0.14
C84	0.15	1549.01	1000	1.74	0.64	2.7	0.15
C85	0.072	1549.3	1100	2	0.57	1.4	0.16
C86	0.026	1549.5	1100	2	0.54	0.5	0.17
C87	0.005	1549.7	1200	2.1	0.46	0.13	0.177

The same trends observed on the performance of PPBGs operated in λ= 850 nm are observed for PPBGs operated in free space wavelengths of 1310 and 1550 nm. To compare the performance of several devices, the sensitivity is generally determined by the magnitude of the change in the measured optical parameter, if the same change is introduced to them. It is clear that the shift is larger (higher performance in biosensing) at a wavelength of 850 nm, and this agrees with the study conducted in [5], where it was found that the wavelengths preferred for surface sensing are near the short wavelength of the Drude region. See Figure 41.

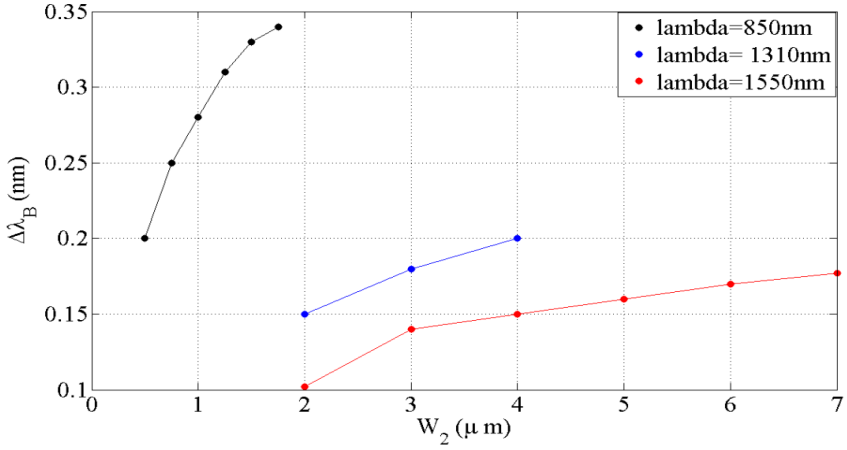

Figure 41: Shift ($\Delta\lambda_B$) achieved with surface sensitivity for different PPBGs designs at different wavelengths, the designs are represented as a function of the small width in the fundamental cell.

As mentioned previously, the confinement of the mode to the metal film is the key to the sensitivity and the foundation of using SPP in biosensing. At the free space wavelength of 850 nm, the mode is highly confined compare to wavelengths of 1310 and 1550 nm. The high confinement at λ= 850 nm enhances the biosensing performance.

Second, the sensitivity is computed by using waveguide sensitivities. Calculating the surface sensitivity in this method gives results that agree very well (96% ~ 99.7 %.) with the results obtained with the previous method. Table 13 shows the exact shift obtained for every design, using each method.

Table 13: Comparison between the biosensing performances ($\Delta\lambda_B$) obtained by calculating the surface sensitivity for the waveguides comprising the gratings, and by calculating the surface sensitivity for the whole device operated at different wavelengths.

Wavelength (nm)	**Cell design**	$\boldsymbol{\Delta\lambda_B}$ (nm) (adding adlayer)	$\boldsymbol{\Delta\lambda_B}$ (nm) (change adlayer thickness by 0.1nm)
850	C2,0.5	0.2	0.1995
	C2,0.75	0.25	0.247
	C2,1	0.28	0.2755
	C2,1.25	0.31	0.3087
	C2,1.5	0.33	0.3278
	C2,1.75	0.34	0.342
1310	C52	0.15	0.1543
	C53	0.18	0.1837
	C54	0.2	0.2085
1550	C82	0.102	0.1044
	C83	0.14	0.1392
	C84	0.15	0.1496
	C85	0.16	0.1566
	C86	0.17	0.1653
	C87	0.177	0.174

For PPBGs, a good performance in biosensing is achieved when the gratings can provide a measurable reflectance, a measurable depth of the transmittance dip ($\Delta T > 1$), relatively narrow bandwidth, and a large shift. Accordingly, several designs are selected to investigate their biosensing performance covering the tuning range of a typical laser. This can be conducted by making a design every 10 nm around the wavelength of interest. The selected designs are C53, C54, C84, and C85. Even though C86 and C87 provide a larger shift than C84 and C85, the depth of their transmittance dip is rather shallow.

The surface sensitivity is calculated for the whole device by adding an adlayer of thickness *a* which represents a molecular monolayer. Changing the wavelength will induce change in the dielectric constants of the materials comprising the gratings. These changes in the refractive indices are considered for all materials by calculating the refractive indices every 10 nm. The PPBGs parameters were modified to ensure the location of the Bragg wavelength λ_B to be placed within the range of the wavelength of interest. Table A1 in the Appendix summarizes the grating parameters and the characteristics of the C53 design operating at a wavelength of 1310nm.

It was found that the performance and the characteristics differ for each design; even the pitch Λ had to be changed at every design to ensure that the Bragg wavelength was to land in the desired range of wavelengths. The trend in biosensing performance agrees with the previous results, where the biosensing performance is enhanced by decreasing the operating wavelength. In general, the reflectance is inversely proportional with the operating wavelength; the pitch has to be increased by approximately 10 nm at each step, which results in increasing the waveguides lengths d_1 and d_2. This is the reason for decreasing the reflectance and the depth of the transmitted dip with longer wavelengths. A fluctuation in the reflectance is noticed because of the properties of water; water has a strong absorption profile that influences the reflectance. The same trend was observed with C54 with improvement in the biosensing performance, $\Delta\lambda_B$ = 0.22 ~ 0.18 nm. Also, the same procedure was followed with C84 and C85. For the gratings with C84 as the fundamental cell, the FWHM is around 0.7 nm, with $\Delta\lambda_B$ from 0.16 ~ 0.13 nm for N=1000, whereas for the PPBGs with C85 as the fundamental cell, the FWHM is around 0.6 nm, and the shift is 0.18~ 0.15 nm for N=1100.

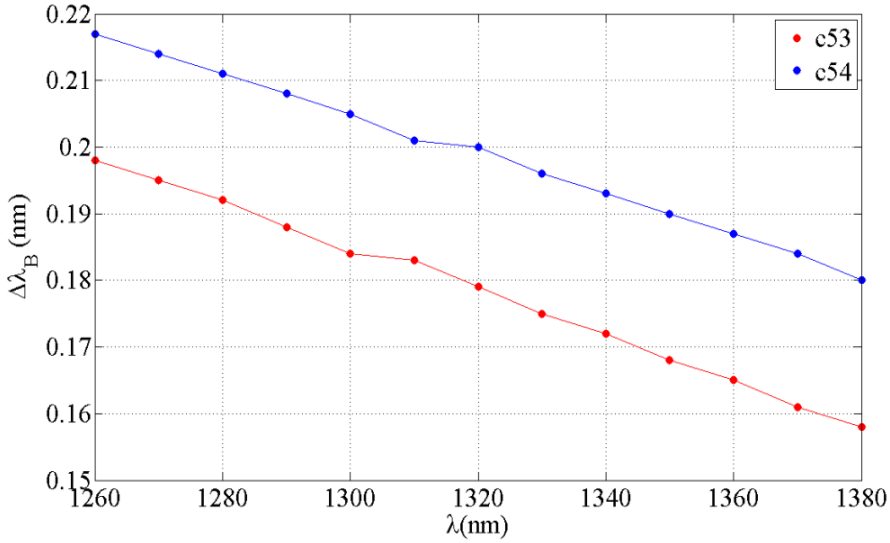

Figure 42: Change in the biosensing performance for two designs C53 and C54 over a range of wavelengths 1260 ~1360 nm.

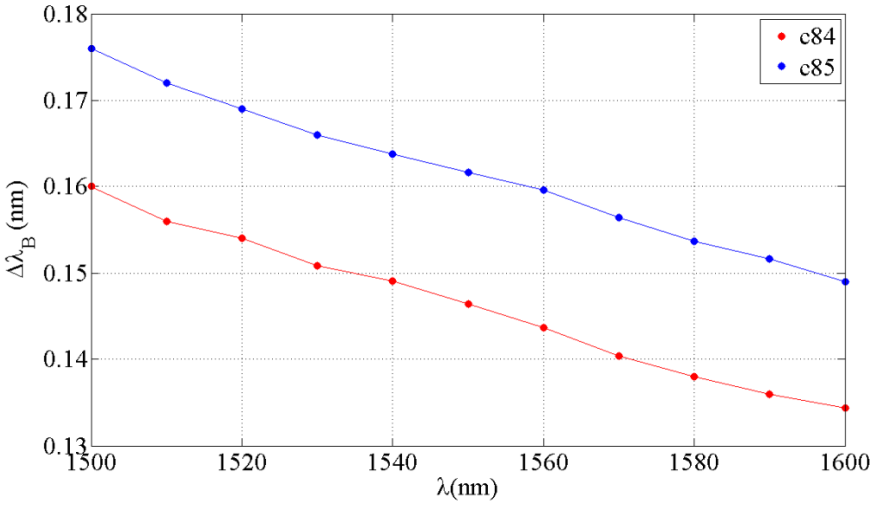

Figure 43: Change in the biosensing performance for two designs C84 and C85 over a range of wavelengths 1500 ~1600 nm.

4.3.2 Bulk Sensitivity

The bulk sensitivity of biosensors is determined from the response of the sensor for different sensing fluids; these sensing fluids have different refractive indices [15, 5, 6, 7]. It was determined to change the index of the sensing solution with 5×10^{-4} as shown previously. The bulk sensitivity is determined by two different approaches; for the grating as a whole

device, and from the waveguide sensitivities. In the former, the index of the sensing solution that covers the grating is changed. This change will affect the effective refractive indices of the ss_b^0modes that are supported by the waveguides constructing the grating. As a result, the grating parameters, including the Bragg wavelength will change. According to this, a shift in the Bragg wavelength will occur, which represents the bulk biosensing performance. The magnitude of the shift depends on, and is associated quantitatively with the magnitude of the refractive index of the surrounding media to the waveguides [77].

The bulk sensitivity can be calculated for the PPBGs from the waveguides that comprise the grating. Using equation (3.11) with taken the derivative with respect to n_c:

$$\frac{\partial \lambda_B}{\partial n_c} = \frac{2\Lambda}{O} \frac{\partial n_{ave}}{\partial n_c} \tag{4.19}$$

where

$$\frac{\partial n_{ave}}{\partial n_c} = \left(\frac{\partial n_{eff,w_1}}{\partial n_c} + \frac{\partial n_{eff,w_2}}{\partial n_c}\right)/2 \tag{4.20}$$

and $\frac{\partial n_{eff,w_1}}{\partial n_c}$ and $\frac{\partial n_{eff,w_2}}{\partial n_c}$ are the bulk sensitivities of the waveguides and are obtained using equation (4.2). Since

$$\frac{\partial \lambda_B}{\partial n_c} \approx \frac{\Delta \lambda_B}{\Delta n_c} \tag{4.21}$$

so the shift is $\Delta\lambda_B = \frac{\partial \lambda_B}{\partial a} . \Delta n_c$ (4.22)

where $\Delta\lambda_B$ is the shift in Bragg wavelength when changing the bulk index of the sensing solution by Δn_c, where $\Delta n_c = 5 \times 10^{-4}$.

4.3.2.1 Modeling Results

As mentioned previously, various values for h_c have been tested, it was found that a suitable value is (5×10^{-5}). This change in the refractive index of the sensing solution can maintain the symmetry of the mode with no radiation, and provide a compatible shift for the values found in the surface sensitivity.

Table 14: Summary of bulk biosensing performance for PPBGs at different wavelengths by inducing a change in the bulk index of the sensing fluid with (5×10^{-4}).

Wavelength (nm)	**Cell design**	$\Delta\lambda_B$ (nm)
850	C2,0.5	0.168
	C2,0.75	0.1647
	C2,1	0.1634
	C2,1.25	0.164
	C2,1.5	0.16403
	C2,1.75	0.16403
1310	C52	0.26
	C53	0.249
	C54	0.2489
1550	C83	0.3161
	C84	0.2923
	C85	0.2929
	C86	0.2917
	C87	0.292

It is noticed in Table 14 that some designs were eliminated because the modes obtained were not bound enough. Also, from the table it is noticed that the biosensing performance increases with an increase in the wavelength. At λ= 850nm, the shift ranges from 0.168 ~ 0.164 nm, whereas at λ= 1550nm, the shift ranges from 0.32~ 0.29 nm. Within the same wavelength, the performance increase slightly with the grating strength. This is the opposite of the results found in surface sensitivity. See Figure 44.

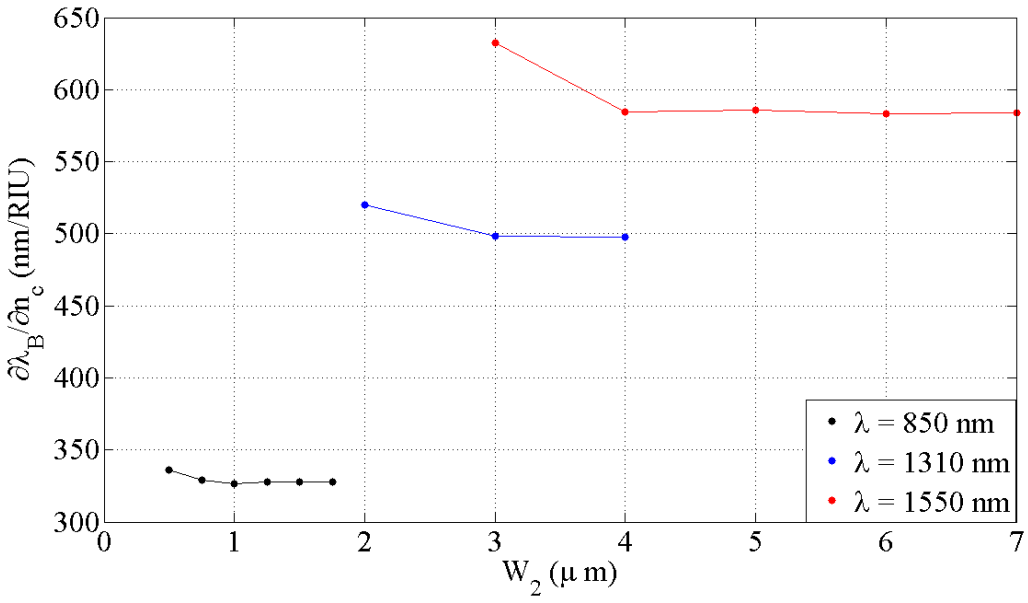

Figure 44: Bulk sensitivities for different designs of PPBGs as a function of w_2.

Comparing both bulk and surface sensitivity performances, different trends are found. First, in surface sensitivity, the performance is inversely proportional to the wavelength, where it is the opposite in bulk sensitivity. At the same wavelength, the biosensing performance in surface sensitivity is enhanced with weaker gratings ($w_1 \sim w_2$) because in such design the sensing surface is larger. The bulk sensitivity exhibits an opposite trend. Overall, the biosensing performance in both cases indicates good potential of PPBGs in biosensing.

4.4 Detection Limit

4.4.1 Detection Limit with Wavelength Interrogation

4.4.1.1 LOD of Surface Sensitivity of PPBGs

The quality of any biosensor is determined by its detection limit or limit of detection (LOD) which is the smallest quantity of substance that can be detected and measured. The detection limit of a biosensor determines its applications. Improvement of the detection limit is always of interest for biosensors. The detection limit for any biosensor depends on its sensitivity and the noise floor of the interrogation system [2].

The detection limit for PPBG surface sensing depends on the surface sensitivity ($\partial\lambda/\partial a$), using equation (4.17)

$$\frac{\Delta\lambda_{min}}{\Delta a_{min}} = \frac{\partial\lambda_B}{\partial a} \tag{4.23}$$

$$\Delta a_{min} = \frac{1}{\partial\lambda_B/\partial a}\,\Delta\lambda_{min} \tag{4.24}$$

where Δa_{min} is the smallest change in the adlayer thickness and $\Delta\lambda_{min}$ is the smallest change in resonant wavelength. A range of LOD is predicted by using two values of $\Delta\lambda_{min}$ that express conservative and aggressive detection limits. From [78], $\Delta\lambda_{min} \approx 20$ pm but for a high-quality spectral interrogation system can be as small as 1 pm. The sensitivity ($\partial\lambda/\partial a$) can be calculated from either equation (4.15) or equation (4.17). The surface sensitivity can be expressed in terms of surface mass coverage Γ ($g m^{-2}$) which is related to the adlayer with the following formula [5].

$$\Gamma = \frac{a(n_a - n_c)}{\partial n/\partial c} \tag{4.25}$$

where $\partial n/\partial c$ ($m^3 g^{-1}$) is the index variation with analyte concentration and is taken as 187 $mm^3 g^{-1}$. From equation (4.25), it is obvious that variations in the surface mass coverage are associated with variations in the adlayer thickness. The detection limit $\Delta\Gamma_{min}$ can be obtained by combining equations (4.24) and (4.25)

$$\Delta\Gamma_{min} = \frac{(n_a - n_c)}{\partial n/\partial c}\,\frac{1}{\partial\lambda/\partial a}\,\Delta\lambda_{min} \tag{4.26}$$

From the equation it is noted that LOD ($\Delta\Gamma_{min}$) is inversely proportional to the PPBGs sensitivity$\partial\lambda/\partial a$; see Table 15.

Table 15: Summary of sensitivity and LOD for surface sensitivity of PPBGs.

λ (nm)	**Cell design**	$\frac{\Delta\lambda_B}{\partial a}$	Δa_{min} (nm) $\Delta\lambda_{min}$=1pm	$\Delta\Gamma_{min}$ pg/mm² $\Delta\lambda_{min}$=1pm	Δa_{min} (nm) $\Delta\lambda_{min}$=20pm	$\Delta\Gamma_{min}$ pg/mm² $\Delta\lambda_{min}$=20pm
850	C2,0.5	0.067	0.015	12.99	0.30	259.8
	C2,0.75	0.083	0.012	10.4	0.24	208
	C2,1	0.093	0.011	9.3	0.22	185.7
	C2,1.25	0.103	0.0097	8.4	0.19	167.7
	C2,1.5	0.11	0.0092	7.9	0.183	157.5
	C2,1.75	0.113	0.0088	6.9	0.18	152.9
1310	C52	0.05	0.019	17.7	0.39	353.4
	C53	0.06	0.016	14.8	0.33	294.2
	C54	0.67	0.015	13.3	0.3	265.3
1550	C82	0.34	0.029	26.2	0.57	523.7
	C83	0.47	0.022	19.1	0.43	382.2
	C84	0.05	0.02	17.8	0.40	356.2
	C85	0.53	0.019	16.7	0.383	334.1
	C86	0.57	0.018	15.8	0.38	314.7
	C87	0.59	0.017	15.05	0.34	301.8

It is noted from the table above that the lowest detection limits can be achieved at λ=850 nm. It is also noted that weaker gratings provide better detection limits.

4.4.1.2 LOD of Bulk Sensitivity of PPBGs

The detection limit is obtained for bulk sensitivity in order to find the smallest change in the bulk index that can be measured $\Delta n_{c,min}$. Similar to the detection limit of surface sensitivity, the detection limit of PPBGs depends on the bulk sensitivity ($\partial\lambda/\partial n_c$). $\Delta n_{c,min}$ can be obtained from equation (4.2)

$$\frac{\Delta\lambda_{min}}{\Delta n_{c,min}} = \frac{\partial\lambda_B}{\partial n_c} \tag{4.27}$$

Hence, the detection limit for bulk sensing is

$$\Delta n_{c,min} = \frac{1}{\partial\lambda_B/\partial n_c}\,\Delta\lambda_{min} \tag{4.28}$$

It is noted that the detection limit decreases as the sensitivity ($\partial\lambda/\partial n_c$) increases.

The PPBGs bulk sensitivity ($\partial\lambda/\partial n_c$) can be calculated using equation (4.19) or (4.21). The detection limit is calculated for two extreme values for the minimum change in the resonant wavelength $\Delta\lambda_{min}$ =1, 20 pm.

Table 16 : Summary of sensitivity and LOD for bulk sensitivity of PPBGs.

λ (nm)	Cell design	$\frac{\Delta\lambda_B}{\partial n_c}$ nm/RIU	$\Delta n_{c,min}$ (RIU) $\Delta\lambda_{min}$=1pm	$\Delta n_{c,min}$ (RIU) $\Delta\lambda_{min}$=20pm
850	C2,0.5	336	29.8×10^{-7}	59×10^{-6}
	C2,0.75	329.3	30.4×10^{-7}	60.7×10^{-6}
	C2,1	326.8	30.6×10^{-7}	61.2×10^{-6}
	C2,1.25	328	30.5×10^{-7}	61×10^{-6}
	C2,1.5	328.1	30.5×10^{-7}	61×10^{-6}
	C2,1.75	328.1	30.5×10^{-7}	61×10^{-6}
1310	C52	520	19×10^{-7}	38.5×10^{-6}
	C53	498	20×10^{-7}	40.2×10^{-6}
	C54	497.8	20×10^{-7}	40.2×10^{-6}
1550	C83	632.2	16×10^{-7}	31.6×10^{-6}
	C84	584.6	17×10^{-7}	34.2×10^{-6}
	C85	585.8	17×10^{-7}	34.1×10^{-6}
	C86	583.4	17×10^{-7}	34.3×10^{-6}
	C87	584	17×10^{-7}	34.3×10^{-6}

It is noted that at the same wavelength, different designs have almost identical detection limits; this is due to similarities in the bulk sensitivities of the waveguides that construct the gratings, as explained earlier in this chapter.

In order to compare the biosensing performance for different designs, Figures of merit (FoMs) are used [79]. They are computed from modal parameters. FoMs are computed

considering the sharpness of the signal (FWHM), and the sensitivity. FoMs for the surface sensitivity are defined by the following equation

$$\text{FoMs} = \frac{\partial \lambda_B / \partial a}{FWHM} \quad (nm^{-1}) \tag{4.29}$$

While for the bulk sensitivity the are defined by the following equation

$$\text{FoMs} = \frac{\partial \lambda_B / \partial n_c}{FWHM} \quad (RIU^{-1}) \tag{4.30}$$

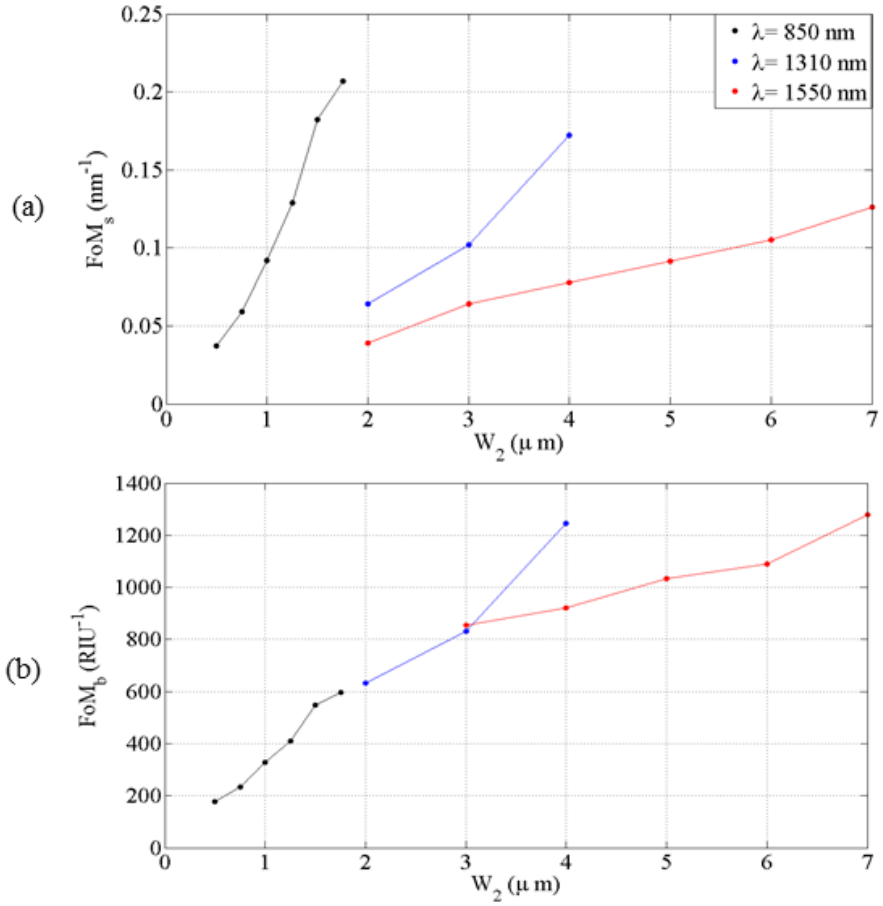

Figure 45: FoM for biosensing performance of PPBGs. (a) FoM for surface sensitivity of PPBGs. (b) FoM for bulk sensitivity of PPBGs.

From the previous Figure it is clear that for surface sensitivity, the biosensing performance increases with shorter wavelengths. For different designs at the same wavelength, the performance enhances with weaker designs ($w_1 \sim w_2$). For bulk sensitivity, the opposite

trend is observed when comparing the performance over a range of wavelengths. PPBGs provide higher biosensing performance at longer wavelengths.

4.4.2 Detection Limit with Power Interrogation

In an attempt to improve detection limits, another interrogation is used based on the output power instead of the wavelength interrogation. The sensitivity in this interrogation is expressed in terms of the (absolute) output power [5], where the Bragg wavelength for the grating is fixed, by adding an adlayer and changing the bulk index. The variations in the output power are used to obtain the detection limit.

4.4.2.1 Detection Limit for Surface Sensitivity of PPBGs

The surface sensitivity in terms of output power is $\partial P_{out}/\partial a$ (nW/nm). Contrary to wavelength interrogation λ_B is fixed and the parameter of interest is the output power as a function of time. The change in the output power ∂P_{out} is obtained by fixing λ_B and monitoring the output power and transmission as a function of time, as the adlayer grows from $a = 0$ to $a = 3$ nm. It is expected that PPBGs with deep transmission and narrow FWHM give better results in terms of sensitivity and detection limits, which is not the case in wavelength interrogation. Changing the adlayer thickness by Δa produces a change in the wavelength spectra and output power by Δp_{out}. Analogous to the equations presented in the previous section, the variations in P_{out} is related to Δa via the following equation

$$\Delta P_{out,min} = \frac{\partial P_{out}}{\partial a} \Delta a_{min} \tag{4.31}$$

hence

$$\Delta a_{min} = \frac{1}{\partial P_{out}/\partial a} \Delta P_{out,min} \tag{4.32}$$

$\Delta P_{out,min}$ is the smallest measurable change in the output power and it is assumed to have the value of 5 nW, and $\partial P_{out}/\partial a$ is the surface sensitivity in terms of the output power. In terms of surface mass coverage, combining Equations (4.25) and (4.32) the detection limit is defined by the following equation

$$\Delta \Gamma_{min} = \frac{(n_a - n_c)}{\partial n/\partial c} \frac{1}{\partial \lambda/\partial a} \Delta P_{out,min} \tag{4.33}$$

The change in the signal in power interrogation depends on the slope of the resonance curve near the resonance, hence it is very sensitive and in order to limit this effect all designs are taken to attain 95% of the total reflection. For this reason, several designs have been eliminated.

Table 17: Summary of LOD for surface sensitivity of PPBGs using power interrogation.

λ (nm)	**Cell design**	$\Delta\Gamma_{min}$ pg/mm^2
850	C2,0.5	3.4
	C2,0.75	22.1
	C2,1	3.1
	C2,1.25	1.8
	C2,1.5	1.6
1310	C52	37.7
	C53	3.2
	C54	54.8
1550	C82	5.8
	C83	21.1
	C84	42.2
	C85	22.6

4.4.2.2 Detection Limit for Bulk Sensitivity of PPBGs

The detection limit for bulk sensitivity is calculated by monitoring the output power and the transmission, while changing the bulk index and fixing λ_B. As in previous derivations, the bulk sensitivity is defined by the following equation

$$\Delta n_{c,min} = \frac{1}{\partial P_{out}/\partial n_c} \Delta P_{out,min} \tag{4.34}$$

Table 18: Summary of LOD for bulk sensitivity of PPBGs using power interrogation.

$\boldsymbol{\lambda}$ (nm)	Cell design	$\boldsymbol{\Delta n_{c,min}}$ (RIU)
850	C2,0.5	6.1×10^{-7}
	C2,0.75	6.9×10^{-7}
	C2,1	7.5×10^{-7}
	C2,1.25	7.1×10^{-7}
	C2,1.5	11.7×10^{-7}
1310	C52	1×10^{-7}
	C53	1.5×10^{-7}
	C54	6.8×10^{-7}
1550	C83	1.6×10^{-7}
	C84	3.2×10^{-7}
	C85	5.1×10^{-7}

An improvement in the biosensing performance of PPBGs is noticed when using power interrogation, but the current designs are subject to optimization.

Chapter 5 Conclusion, Contributions and Future Work

5.1 Conclusions, Contributions and Future work

In this thesis we have theoretically investigated the design and performance of surface plasmon-polariton Bragg gratings as biosensors. We started the study by investigating the basic constructing elements in plasmon-polariton Bragg gratings which are the long range surface plasmon waveguides. The characteristics of the waveguides were demonstrated, then, the gratings were modeled using a Transfer Matrix Method, and the simulations were carried out in a Matlab environment. The simulator was verified by reproducing results from previous work. The modeling work was associated with an overview of design parameters and properties. The overview outlined design rules and considerations for controlling the spectral characteristics of the gratings. The study treated one architecture of plasmon-polariton Bragg gratings which is the uniform periodic PPBGs, but expands to include several designs at different free space wavelengths, in order to optimize the performance of PPBGs as biosensors.

Both surface and bulk sensitivities were investigated using wavelength interrogation. Both sensitivities were found in two approaches, from the PPBGs as a device and from the waveguides that construct the gratings. Results were achieved with high agreement. In surface sensitivity, a 3nm thick adlayer is used to find the sensitivity for the gratings; the thickness of this adlayer is changed by $\pm$ 0.1nm to find the sensitivity for the waveguides. In bulk sensitivity, the importance of keeping the symmetry of the mode was considered while testing the mode with different solutions.

In order to optimize the biosensing performance of PPBGs, detection limits were found for both surface and bulk sensitivities with two different interrogations, wavelength and power. Improvement in the performance was observed when different designs were used for different interrogations, to optimize the biosensing performance.

5.2 Thesis Contributions

This thesis work has made contributions to the field of biosensing.

- Biosensing performance of PPBGs was evaluated theoretically for both bulk and surface sensitivities using two different interrogations.
- Designs of PPBGs at different wavelengths for biosensing have been presented, and are currently being tested.
- The work of this thesis is being prepared in manuscript for publication.

5.3 Future Work

This work highlights the biosensing performance of PPBGs. The results are promising, and the work conducted is subject to experimental verifications to confirm the numerical results obtained. The designed PPBGs have been fabricated and are presently being tested to verify the conclusions of this thesis work by other members of the group.

References

[1] J. Homola,"Surface Plasmon Resonance Sensors for Detection of Chemical and Biological Species," *Chemical Reviews,* vol. 108, pp. 462- 493, 2008.

[2] J. Homola,"Present and Future of Surface Plasmon Resonance Biosensors, " *Analytical and Bioanalytical Chemistry,* vol. 377, pp. 528-539, 2003.

[3] J. Homola *et al.*,"Surface Plasmon Resonance Sensors: Review," *Sensors and Actuators B: Chemical,* vol. 54, pp. 3- 15, 1999.

[4] X. Fan, *et al.*, "Sensitive Optical Biosensors for Unlabeled Targets: a Review," *Analytica Chimica Acta,* vol. 620, pp. 8- 26, 2008.

[5] P. Berini, "Bulk and Surface Sensitivities of Surface Plasmon Waveguides, " *New Journal of Physics,* vol. 10, p. 105010, 2008.

[6] O. Krupin *et al.*, "Biosensing Using Straight Long-Range Surface Plasmon Waveguides, " *Optics Express,* vol. 21, pp. 698-709 , 2013.

[7] M. Valva *et al.*, "Long-Range Surface Plasmons for Sensitive Detection of Bacterial Analytes," *Sensors and Actuators B: Chemical,* vol. 139, pp. 59-63, 2009.

[8] R. Slavik, J. Homola, "Ultrahigh Resolution Long Range Surface Plasmon-Based Sensor," *Sensors and Actuators B: Chemical,* vol. 123, pp. 10-12, 2007.

[9] S. Jettè-Charbonneau *et al.*, "Demonstration of Bragg Gratings Based on Long Ranging Surface Plasmon Polariton Waveguides," *Optics Express,* vol. 13, pp. 4674- 4682, 2005.

[10] S. Jettè, "A Study of Bragg Gratings based on Plasmon-Polariton Wave Guides," M.Sc. thesis, University of Ottawa, Ottawa, Canada, 2003.

[11] B. Liedberg *et al.*, "Surface Plasmon Resonance for Gas Detection and Biosensing," *Sensors and Actuators ,* vol. 4, pp. 299- 304, 1983.

[12] S. A. Maier, *Plasmonics: Fundamentals and Applications*, Springer, 2007.

[13] R. Wood, *On a Remarkable Case of Uneven Distribution of Light in a Diffraction Grating Spectrum*, Taylor & Francis, 1902.

[14] A. Otto, "Excitation of surface plasma waves in silver by the method of frustrated total reflection," *Zeitschrift Physik,* vol. 216, no. 4, pp. 398- 410, 1968.

[15] A. Khan, "Characterization of Bio-Sensing Waveguides in CYTOP Operating with Long Range Surface Plasmon Polaritons, " M.Sc. thesis, University of Ottawa, Ottawa, Canada, 2013.

[16] E. Wijaya *et al.*, "Surface Plasmon Resonance-based Biosensors: From the Development of Different SPR Structures to Novel Surface Functionalization Strategies," *Current Opinion in Solid State and Material Science,* vol. 15, no. 5, pp. 208- 224, 2011.

[17] A. Khan *et al.*, "Mach-Zehnder Refractometric Sensor Using Long-Range Surface Plasmon Waveguides," *Applied Physics Letters,* vol. 103, pp. 111108-1 - 111108-4, 2013.

[18] A. V. Kabashin *et al.*, "Plasmonic Nanorod Metamaterials for Biosensing," *Nature Materials Letters,* vol. 8, pp. 867- 871, 2009.

[19] B. Spackova, J. Homola, "Theoretical Analysis of a Fiber Optic Surface Plasmon Resonance Utilizing Bragg Gratings," *Optics Express,* vol. 17, pp. 23254- 23264, 2009.

[20] P. Berini, "Plasmon-Polariton Waves Guided by Thin Lossy Metal Films of Finite Width: Bound Modes of Symmetric Structures," *Physical Reviews B,* vol. 61, pp. 10484- 10503, 2000.

[21] R. Daviau *et al.*, "Fabrication of Surface Plasmon Waveguides and Integrated Components on Cytop," *Microelectronic Engineering,* vol. 87, pp. 1914-1921, 2010.

[22] P. Berini, "Long-Range Surface Plamon Polaritons," *Advances in Optics and Photonics,* vol. 1, pp. 484- 588, 2009.

[23] F.C. Chien, S. J. Chen, "A Sensitivity Comparison of Optical Biosensors Based on Four Different Surface Plasmon Resonance Modes," *Biosensors and Bioelectrons,* vol. 20, pp. 633-642, 2004.

[24] P. Berini *et al.*, "Long Range Surface Plasmon on Ultrathin Membrane," *Nano Letters,* vol. 7, pp. 1376- 1380, 2007.

[25] V.N. Konopsky, E. V. Alieva,"Long-Range Plasmons in Lossy Metal Films on Photonic Crystal Surfaces," *Optics Letters,* vol. 34, pp. 479- 481, 2009.

[26] *Asahi Glass Company, "Amorphous Polymer Cytop".*

[27] O. Krupin *et al.*, "Selective Capture of Human Red Blood cells Based on Blood Group Using Long-Range Surface Palsmon Waveguides," *Biosensors and Bioelectronics,* vol. 53, pp. 117- 122, 2014.

[28] O.Krupin, P. Berini, "Biosensing Using Plasmonic Waveguides Embedded in CYTOP," in *Photonics North 2012* , Montreal, Canada, 2012.

[29] A. Khan *et al.*, "Sensing of Bacteria Immobilised Under Static Conditions Using Long-Range Surface Plasmon Waveguides in Cytop," in *Photonics North 2011*, Ottawa, Canada, 2011.

[30] R. Charbonneau *et al.*, "Demonstration of Surface Sensing Using Long-Range Surface Plasmon Waveguides on Silica," *Sensors and Actuators B: Chemical,* vol. 134, pp. 455-461, 2008.

[31] S. I. Bozhevolnyi *et al.*, "Observation of Propagation of Surface Plasmon Polaritons Along Line Defects in a Periodically Corrugated Metal Surface," *Optics Letters,* vol. 26, pp. 734-736, 2001.

[32] S. I. Bozhevolnyi *et al.*, "Photonic Bandgap Structures for Long-Range Surface Plasmon Polaritons," *Optics Communications,* vol. 250, pp. 328- 333, 2005.

[33] A. Boltasseva *et al.*, "Compact Bragg Gratings for Long-Range Surface Plasmon Polaritons," *Journal of Lightwave Technology,* vol. 24, pp. 912- 918, 2006.

[34] S. Jettè-Charbonneau *et al.*, "Bragg Gratings Based on Long-Range Surface Plasmon-Polariton Waveguides: Comparison of Theory and Experiment," *IEEE Journal of Quantum Electronics,* vol. 41, pp. 1480- 1491, 2005.

[35] S. Jettè-Charbonneau *et al.*, "Demonstration of Bragg gratings based on longranging surface plasmon polariton waveguides," *Optics Express,* vol. 13, pp.4674-4682, 2005.

[36] Y. H. Joo *et al.*, "Long-Range Surface Plasmon-Polariton Waveguide Sensors with a Bragg Grating in the Asymmetric Double-Electrode Structure," *Optics Express,* vol. 17, pp. 10606- 10611, 2009.

[37] Y. H. Joo *et al.*, "Demonstration of Long-Range Surface Plasmon Polariton Waveguides Sensors with Asymmetric Double-Electrode Structures," *Applied Physics Letters ,* vol. 97, 2010.

[38] Kristjan loesson *et al.*, "Long-Range Surface Plasmon Polariton Waveguides and Devices," in *Plasmonics and Plasmonic Metamaterials*, Singapore, World Scientific, 2012.

[39] Y. Wang *et al.*, "Foundation of Plasmonics," *Advances in Physics*, vol. 60, pp. 799-898, 2011.

[40] A. J. Tudos, R. B. M. Schasfoort, "Introduction to Surface Plasmon Resonance," in *Handbook of Surface Plasmon Resonance*, Cambridge, RSC publishing, 2008.

[41] P. Berini, "Plasmon Polariton Modes Guided by a Metal Film of Finite Width," *Optics Letters,* vol. 24, pp. 1011-1013, 1999.

[42] S. A. Ramakrishna, T. M. Grzegorczyk, Physics and Applications of Negative Refractive Index Metamaterials, Bellingham: CRC press, 2008.

[43] F. A. Burton, S. A. Cassidy, "A Complete Description of the Dispersion Relation for thin metal film plasmon-polaritons," *Journal of Lightwave Technology,* vol. 8, pp. 1843-1849, 1990.

[44] D. R. Smith *et al.*, "Metamaterials and Negative Refractive Index," *Science Magazine,* vol. 305, pp. 788-792, 2004.

[45] A. D. Boardman, Electromagnetic Surface Modes, New York: Wiley, 1982.

[46] P. Berini *et al.*, "Characterization of Long-Range Surface-Plasmon-Polariton Waveguides," *Journal of Applied Physics,* vol. 98, pp. 043109-1-043109-12, 2005.

[47] P. Berini, "Plasmon Polariton Waves Guided by Thin Lossy Metal Films of Finite Width: Bound Modes of Asymmetric Structures," *Physical Review B,* vol. 63, 2001.

[48] R. Charbonneau *et al.*, "Passive Integrated Optics Elements Based on Long Range Surface Plasmon Polaritons," *Journal of Lightwave Technology,* vol. 24, p. 477-494, 2006.

[49] J. R. Krenn, J. C. Weeber, "Surface Plasmon Polaritons in Metal Stripes and Wires," *The Royal Society,* vol. 362, pp. 739-756, 2004.

[50] R. Charbonneau *et al.*, "Experimental Observation of Plasmon-Polariton Waves Supported by a Thin Metal Film of Finite Width," *Optics Letters,* vol. 25, pp. 844-846, 2000.

[51] Hui Fan *et al.*, "Passive Long-Range Surface Plasmon-Polariton Devices in Cytop," *Applied Optics,* vol. 51, pp. 1459-1467, 2012.

[52] P. Berini, R. Buckley, "On the Convergence and Accuracy of Numerical Mode Computations of Surface Plasmon Waveguides," *Journal of Conmputational and Theoritical Nanoscience,* vol. 6, pp. 2040-2053, 2009.

[53] E. D. Palik, Handbook of Optical Constants of Solids, Orlando: FL academic, 1985.

[54] D. J. Segelstein, "The Complex Refractive Index of Water," M.Sc. thesis, University of Missouri, Kansas City, 1981.

[55] R. Buckley, P. Berini, "Figures of Merit for 2D Surface Plasmon waveguides and Application to Metal Stripes," *Optics Express,* vol. 15, pp.12174-12182, 2007.

[56] K. Thyagarajan, A. Ghatak, Fiber Optics Essentials, New Jersey: John Wiley and sons, 2007.

[57] P. Yeh, Optical waves in Layered Media, John Wiley and sons, 1988.

[58] R. Kashyap, Fiber Bragg Gratings, Academic press, 1999.

[59] S. Jettè-Charbonneau, P. Berini, "Theoretical Performance of Bragg gratings based on Long-Range surface Plasmon-Polariton Waveguides," *Journal of Optical society of America A,* vol. 23, pp.1757-1767, 2006.

[60] N. Matuschek, "Exact Coupled-Mode Theories for Multilayer interference coatings with Arbitrary Strong Index Modulation," *IEEE Journal of Quantum Electronics ,* vol. 33, pp.295-302, 1977.

[61] M. McCall, "On the Application of Coupled Mode Theory for Modeling Fiber Bragg Gratings," *Journal of Lightwave Technology,* vol. 18, pp.236-242, 2000.

[62] A. Hardy, W. Streifer, "Coupled Mode Theory of Parallel Waveguides," *Journal of Lightwave Technology,* vol. 3, pp.1135-1146, 1985.

[63] A. Yariv, "Coupled-Mode Theory for Guided-Wave Optics," *IEEE Journal of Quantum Electronics,* vol. 9, pp.919-933, 1973.

[64] W. Streifer *et al.*, "Reformulation of the Coupled-Mode Theory of Multiwaveguide Systems," *Journal of Lightwave Technology,* vol. 5, pp.1-4, 1987.

[65] L. A. Weller-Brophy, D. J. Hall, "Analysis of Waveguide Gratings: Application of Rouard's Method," *Journal of Optical Society of America,* vol. 2, pp.863-871, 1985.

[66] L. A. Weller-Brophy, D. J. Hall, "Analysis of Waveguide Gratings: a Comparison of the Results of Rouard's Method and Coupled-Mode Theory," *Journal of Optical Society of America,* vol. 4, pp.60-65, 1987.

[67] B. Lissak, M. Tur, "Fiber Bragg Grating Analysis Using the Floquet-Bloch Approach," *SPIE,* vol. 3110, pp.428-438, 1997.

[68] C. Chengkun *et al.*, "Effeicient and Accurate Numerical Analysis of Mutilayer Planar Optical Waveguides," in *Terahertz and Gigahertz Photonics*, Denver, SPIE*,* vol. 3795, 1999.

[69] R. Schasfoort, A. McWhirter, "SPR Instrumentation," in *Handbook of surface Plasmon Resonance*, Cambridge, RSC publishing, 2008.

[70] F. Dell'Olio, V. Passaro, "Optical Sensing by Optimized Silicon Slot Waveguides," *Optics Express,* vol. 15, pp. 4977-4993, 2007.

[71] W. Lukozs, "Principles and Sensitivities of Integrated and Surface Plasmon Sensors for direct affinity sensing and Immunosensing," *Biosensors and Bioelectronics,* vol. 6, pp. 215-225, 1991.

[72] R. Charbonneau *et al.*,"Demonstration of Surface Sensing Using Long-Range Surface Plasmon Waveguides on Silica," *Sensors and Actuators: Chemical B,* vol. 134, pp. 455–461, 2008.

[73] N. M. Lyndin *et al.*, "Long-Range Surface Plasmons in Asymmetric Layered Metal-Dielectric Structures," *Sensors and Actautors: Chemical B,* vol. 54, pp. 37-42, 1999.

[74] C. Y. Chao, L. J. Guo, "Design and Optimization of Microring Resonators in Biochemical Sensing Applications," *Journal of Lightwave Technology,* vol. 24, no. 3, pp. 1395-1402, 2006.

[75] E. T. Gedig, "Surface Chemistry in SPR Technelogy," in *Handbook of Surface Plasmon Resonance*, Cambridge, RSC publishing, 2008.

[76] J. Spinke *et al.*, "Molecular Recognition on Functionalized Self-Assembled Monolayers," *The Journal of Chemical Physics,* vol. 99, pp. 7011-7019, 1993.

[77] I. Abdulhalim *et al.*, "Surface Plasmon Resonance for Biosensing: A mini-Review," *Electomagnetics,* vol. 28, no. 3, pp. 214-242, 2008.

[78] T. Cleas *et al.*, "Vernier-Cascade label-free Biosensor with Integrated Arrayed Waveguide Grating for Wavelength Interrogation with Low-coast Broadband Source," *Optics Letter,* vol. 36, pp. 3320- 3322, 2011.

[79] B. Paivanranta, "High Aspect Ratio Plasmonic Nanostructures for sensing Applications," *ACS Nano,* vol. 5, pp. 6374-6382, 2011.

Appendix A Design Parameters

Table A 1: Summary of design parametrs and spectral characteristics of C53 at range of wavelenght (1260: 1380) nm. The shift ($\Delta\lambda_B$) is obtained for surface sensitivity by intorucing an adlayer of 3nm thickness on top of the gratings. The culculations are curried with TMM.

λ (nm)	R	λ_B (nm)	Λ (nm)	d_1, d_2 (nm)	N	L (mm)	FWHM (nm)	$\lvert\Delta T\rvert$ (nm)	$\Delta\lambda_B$ (nm)
1260	0.2047	1267.1	1420	710	1000	1.42	0.552	3.9	0.2
1270	0.2062	1275.9	1430	715	1000	1.43	0.552	3.8	0.194
1280	0.2071	1284.6	1440	720	1000	1.44	0.552	3.73	0.192
1290	0.2079	1293.4	1450	725	1000	1.45	0.552	3.7	0.188
1300	0.2077	1302.1	1460	730	1000	1.46	0.553	3.6	0.185
1310	0.2066	1311	1470	735	1000	1.5	0.554	3.6	0.182
1320	0.2059	1328.6	1490	745	1000	1.5	0.558	3.6	0.18
1330	0.2038	1337.3	1500	750	1000	1.5	0.559	3.5	0.176
1340	0.1999	1346.1	1510	755	1000	1.51	0.56	3.4	0.174
1350	0.1910	1354.9	1520	760	1000	1.52	0.563	3.3	0.17
1360	0.1891	1363.7	1530	765	1000	1.53	0.564	3.2	0.167
1370	0.1812	1372.4	1540	770	1000	1.54	0.57	3.1	0.164
1380	0.1672	1381.2	1550	775	1000	1.55	0.573	3.0	0.16

Table A 2: Summary of design parametrs and spectral characteristics of C54 at range of wavelenght (1260: 1380) nm. The shift ($\Delta\lambda_B$) is obtained for surface sensitivity by intorucing an adlayer of 3nm thickness on top of the gratings. The culculations are curried with TMM.

λ (nm)	R	λ_B (nm)	Λ (nm)	d_1,d_2 (nm)	N	L (mm)	FWHM (nm)	$\lvert\Delta T\rvert$ (nm)	$\Delta\lambda_B$ (nm)
1260	0.0421	1267.7	1420	710	1100	1.6	0.4406	0.76	0.217
1270	0.0424	1276.4	1430	715	1100	1.6	0.4414	0.76	0.214
1280	0.0431	1285.1	1440	720	1100	1.6	0.442	0.76	0.211
1290	0.0434	1294	1450	725	1100	1.6	0.443	0.75	0.208
1300	0.0435	1302.6	1460	730	1100	1.61	0.445	0.74	0.205
1310	0.0437	1311.4	1470	735	1100	1.62	0.447	0.74	0.201
1320	0.0437	1329.1	1490	745	1100	1.64	0.449	0.73	0.2
1330	0.0434	1337.8	1500	750	1100	1.7	0.45	0.73	0.196
1340	0.04	1346.6	1510	755	1100	1.7	0.455	0.71	0.193
1350	0.04	1355.3	1520	760	1100	1.7	0.46	0.69	0.19
1360	0.0403	1364.2	1530	765	1100	1.7	0.462	0.72	0.187
1370	0.0386	1372.9	1540	770	1100	1.7	0.467	0.71	0.184
1380	0.035	1381.7	1550	775	1100	1.71	0.48	0.68	0.18

Table A 3: Summary of design parametrs and spectral characteristics of C84 at range of wavelenght (1500: 1600) nm. The shift ($\Delta\lambda_B$) is obtained for surface sensitivity by intorucing an adlayer of 3nm thickness on top of the gratings. The culculations are curried with TMM.

λ (nm)	R	λ_B (nm)	Λ (nm)	d_1,d_2 (nm)	N	L (mm)	FWHM (nm)	|ΔT| (nm)	$\Delta\lambda_B$ (nm)
1500	0.109	1505	1690	845	1000	1.7	0.691	2.61	0.16
1510	0.120	1513.7	1700	850	1000	1.7	0.675	2.67	0.156
1520	0.129	1522.5	1710	855	1000	1.71	0.663	2.71	0.154
1530	0.135	1531.2	1720	860	1000	1.72	0.65	2.73	0.151
1540	0.142	1548.9	1730	865	1000	1.73	0.646	2.74	0.148
1550	0.149	1557.6	1750	875	1000	1.75	0.644	2.75	0.146
1560	0.155	1566.5	1760	880	1000	1.76	0.639	2.74	0.144
1570	0.160	1575.2	1770	885	1000	1.77	0.638	2.73	0.140
1580	0.164	1584	1780	890	1000	1.78	0.634	2.71	0.138
1590	0.169	1592.7	1790	895	1000	1.79	0.631	2.69	0.136
1600	0.172	1601.6	1800	900	1000	1.8	0.628	2.67	0.134

Table A 4: Summary of design parametrs and spectral characteristics of C85 at range of wavelenght (1500: 1600) nm. The shift ($\Delta\lambda_B$) is obtained for surface sensitivity by intorucing an adlayer of 3nm thickness on top of the gratings. The culculations are curried with TMM.

λ (nm)	R	λ_B (nm)	Λ (nm)	d_1,d_2 (nm)	N	L (mm)	FWHM (nm)	|ΔT| (nm)	$\Delta\lambda_B$ (nm)
1500	0.05	1505.9	1690	845	1100	1.86	0.63	1.31	0.175
1510	0.056	1514.6	1700	850	1100	1.87	0.6	1.35	0.172
1520	0.06	1523.5	1710	855	1100	1.89	0.59	1.37	0.169
1530	0.064	1532.2	1720	860	1100	1.9	0.58	1.39	0.166
1540	0.068	1541	1730	865	1100	1.9	0.569	1.41	0.164
1550	0.072	1558.6	1750	875	1100	1.93	0.565	1.42	0.162
1560	0.075	1567.4	1760	880	1100	1.94	0.563	1.42	0.16
1570	0.079	1576.1	1770	885	1100	1.95	0.559	1.43	0.156
1580	0.081	1585	1780	890	1100	1.96	0.556	1.43	0.154
1590	0.085	1593.7	1790	895	1100	1.97	0.553	1.43	0.152
1600	0.087	1602.2	1800	900	1100	1.98	0.543	1.43	0.149